Anomalous diffusion of Dirac fermions

Christoph Waldemar Groth
GEBOREN TE GDYNIA, POLEN IN 1980

Promotiecommissie

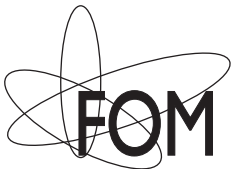|	
Promotor:	prof. dr. C. W. J. Beenakker
Co-Promotor:	dr. J. Tworzydło (Universiteit van Warschau)
Overige leden:	prof. dr. G. T. Barkema
	prof. dr. ir. J. W. M. Hilgenkamp
	prof. dr. J. M. van Ruitenbeek
	dr. X. Waintal (CEA Grenoble)

The cover shows a snapshot from a simulation of anomalous diffusion on a Sierpiński lattice (Chapter 2). The blue and red dots correspond, respectively, to occupied and empty sites. Particles enter the system via the bottom left corner and leave it via the bottom right corner. One can see how obstacles (black triangles) hinder the transport on all length scales.

Contents

1 Introduction

1.1 Normal and anomalous diffusion

Diffusion is the spreading of randomly moving particles from regions with higher concentration to regions with lower concentration. The first class of diffusive processes to have been recognized historically is now known under the name *normal diffusion*. Its signature is the linear growth with time of the mean squared displacement of a particle from its starting point,

$$\langle x^2 \rangle = Dt. \tag{1.1}$$

On long time scales all normal diffusive processes show the same behavior and microscopic details of particle dynamics play no role other than determining the value of the *diffusion coefficient D*.

The importance and generality of the concept of normal diffusion was recognized in the nineteenth century. One of the first milestones was the discovery of Brownian motion, the diffusion of particles suspended in a fluid, by Scottish botanist Robert Brown in 1827 [27]. It was subsequently realized that phenomena seemingly as different as the spreading of infected mosquitos [107] and the conduction of heat in solids can be described in terms of normal diffusion.

The driving force for diffusion need not be differences in concentration, but can also be a difference in potential energy. Electrical conduction in metals is usually also a normal diffusive process, driven by differences in electrical potential (since differences in electron concentration would violate charge neutrality) [39].

Though it is a remarkably general concept, normal diffusion fails to describe all diffusive phenomena. Since the 1970s, increasingly

processes were found in nature [125] where the mean squared displacement of a particle scales as a power of time different from unity,

$$\langle x^2 \rangle = Dt^\gamma, \quad \gamma \neq 1. \tag{1.2}$$

Examples include the foraging patterns of some animals [16], human travel behavior [26], and the spreading of light in a cloudy atmosphere [40]. This kind of diffusion has been termed *anomalous*, and can occur in two varieties: *subdiffusion*, where the particles spread with time arbitrarily slower than normal diffusion ($\gamma < 1$), and *superdiffusion*, where they spread arbitrarily faster ($\gamma > 1$, with an upper limit $\gamma = 2$ for ballistic motion without any scattering).

Random walks are stochastic processes in which particles move in a sequence of randomly directed steps. The lengths s of the steps and the duration τ of a step are drawn from a probability distribution $P(s, \tau)$. (For simplicity, we assume an isotropic random walk, so P is independent of the direction of the step.) For a random walk to be normal, the variance $\text{Var}\, s = \langle s^2 \rangle - \langle s \rangle^2$ of the step size has to be finite as well as the average duration $\langle \tau \rangle$. Then, according to the central limit theorem, the mean square displacement after time t will approach a normal distribution with variance $(t/\langle \tau \rangle)\, \text{Var}\, s$. This is the reason for the previously mentioned similarity of all diffusive processes.

If the requirements for a normal random walk are violated, the random walk will be anomalous and the scaling of the mean squared displacement will in general have a power law (1.2) with $\gamma \neq 1$. This can occur in several ways (See Ref. [145] for a detailed presentation).

Superdiffusion happens if the step size distribution $P(s)$ has a heavy tail $\propto 1/s^{1+\alpha}$ for large s, with $0 < \alpha < 2$. If the duration $\tau = vs$ is simply proportional to the step size (with constant velocity v) this leads to superdiffusive behavior with

$$\gamma = \max(3 - \alpha,\ 2). \tag{1.3}$$

Such an anomalous random walk is called a Lévy walk, after the French mathematician Paul Pierre Lévy. Alternatively, one
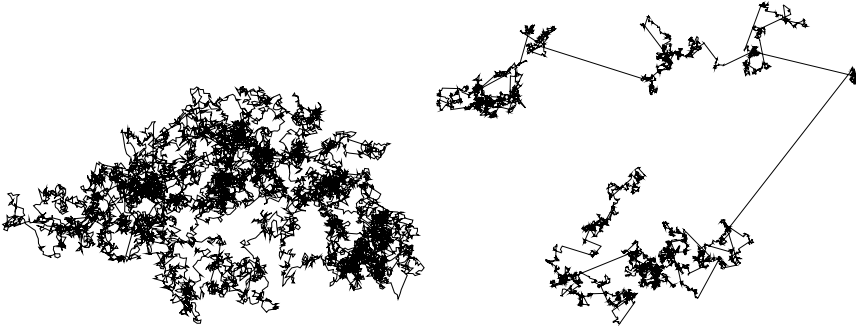
Figure 1.1: Two random walks of 10^4 steps each, characterized by a power-law-tailed step size distribution $P(s) = \alpha/s^{\alpha+1}$ for $s > 1$, $P(s) = 0$ otherwise. The left walk is normal with $\alpha = 3$ (Brownian walk), while the right one has $\alpha = 3/2$ which makes it superdiffusive (Lévy walk). One clearly sees how individual steps play no dominant role in normal diffusion, while superdiffusion is dominated by individual long steps on all length scales.

might give each step the same duration τ_0, independent of the step length. This socalled a Lévy flight has a divergent mean square displacement at any time $t > \tau_0$, and is therefore not physically realistic.

Fig. 1.1 shows two realizations of power-law-tailed random walks of which one is normal and one superdiffusive.

Another way to break normal diffusion is to have a step size distribution with a finite variance, but to associate with the steps durations drawn from a distribution with infinite mean. (See [11] for an introduction.) This leads to subdiffusive behavior characterized by $\gamma < 1$. Effectively, this happens if the random walk is performed on a fractal: a scale-invariant object of non-integer *fractal dimension* d_f embedded in Euclidean space of dimension $d > d_f$. The pieces of Euclidean space which are not part of the fractal present obstacles to the walker that are present at all length scales and slow down the diffusion. The value of $\gamma < 1$ is specific
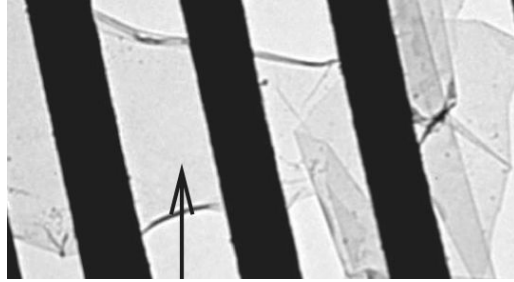
Figure 1.2: Bright-field transmission electron microscope image of a freely suspended graphene sheet. A homogeneous and featureless region of a monolayer graphene is indicated by the arrow; image from Ref. [93].

for each fractal and independent of the fractal dimension.

1.2 Dirac fermions and graphene

In 2004, Andre Geim and Konstantin Novoselov succeeded in isolating for the first time one atom thick flakes of graphite. Their achievement was awarded earlier this year with the Nobel prize in Physics.

This new material, named graphene, is made up of a single layer of carbon atoms arranged in a honeycomb lattice and was previously thought to be unstable and therefore only to exist as part of three-dimensional structures. With the wisdom of hindsight the existence of one atom thick crystals can be reconciled with theory [93]: slight corrugations of the monoatomic carbon film reinforce it against destructive thermal vibrations. Fig. 1.2 shows a photograph of a freely suspended piece of graphene.

The basic electronic properties of graphene which, mostly out of theoretical curiosity, had been studied since the 1940s [143, 91] could be verified by the experiments of Geim, Novoselov and others. The most striking feature is the double-cone shaped dispersion relation of electrons in graphene shown in the right panel of Fig.

4
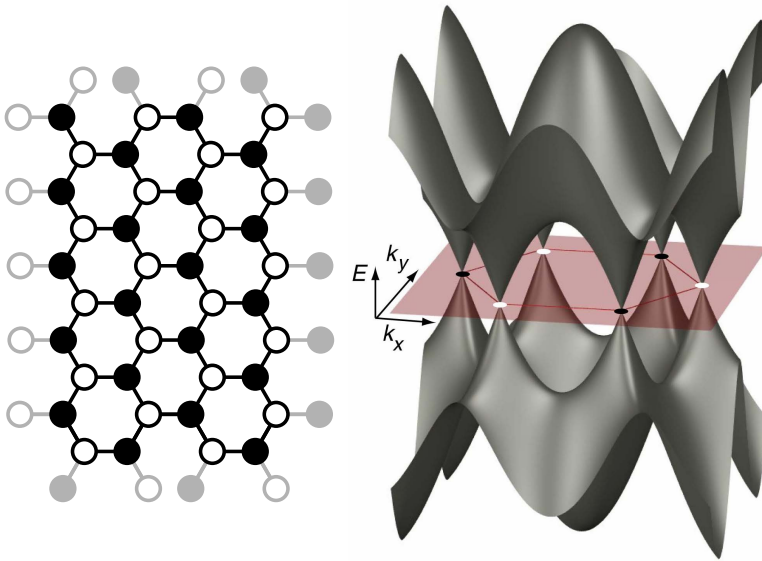
Figure 1.3: Left panel: Honeycomb lattice of carbon atoms in graphene. The unit cell contains two atoms, labeled A and B (open and closed circles). Right panel: Brillouin zone of graphene with a linear double cone spectrum at its corners; independent cones are indicated by open and closed circles. Illustration by C. Jozsa and B. J. van Wees.

1.3. As the velocity of the charge carriers is given by the derivative of the dispersion relation, we see that the speed of electrons in graphene is a constant independent of energy (for energies small enough such that the linear relation holds).

This is a most unusual property for particles in condensed matter physics. (Usually, the velocity increases with the square root of the energy.) It reminds of the energy-independent speed of photons, and indeed the low-energy long-wave length physics of electrons in graphene obeys the Dirac equation of relativistic quantum mechanics, or, more specifically, its two-dimensional massless version

$$-i\hbar v \begin{pmatrix} 0 & \partial_x - i\partial_y \\ \partial_x + i\partial_y & 0 \end{pmatrix} \begin{pmatrix} \Psi_A \\ \Psi_B \end{pmatrix} = E \begin{pmatrix} \Psi_A \\ \Psi_B \end{pmatrix}. \tag{1.4}$$

The A and B components of the wave function correspond to excitations on the two sublattices of the honecomb lattice (see left panel of Fig. 1.3) and form a spin-like degree of freedom called pseudospin. The velocity v is the effective speed of light which in graphene is about 10^6 m/s or $1/300$ of the true speed of light.

Definition of the vector of Pauli matrices $\boldsymbol{\sigma} = (\sigma_x, \sigma_y, \sigma_z)$ allows to express Eq. (1.4) in the compact form

$$v\boldsymbol{p} \cdot \boldsymbol{\sigma}\, \psi = E\psi, \tag{1.5}$$

with the momentum operator $\boldsymbol{p} = -i\hbar(\partial_x, \partial_y)$ and the spinor $\psi = (\Psi_A, \Psi_B)$. Electrons governed by Dirac equation are called Dirac fermions.

The Dirac equation has only a single *Dirac cone*, while the dispersion relation of graphene shown in the right panel of Fig. 1.3 has two independent cones called valleys. (Adjacent cones are independent, while next-nearest-neighbors are equivalent upon translation by a reciprocal lattice vector.) The existence of two independent cones is accounted for by the valley degree of freedom and the full[1] low energy physics has to be described by a four component spinor $\boldsymbol{\Psi} = (\Psi_A, \Psi_B, -\Psi'_B, \Psi'_A)$ satisfying the four-dimensional Dirac equation

$$\begin{pmatrix} v\boldsymbol{p} \cdot \boldsymbol{\sigma} & 0 \\ 0 & v\boldsymbol{p} \cdot \boldsymbol{\sigma} \end{pmatrix} \boldsymbol{\Psi} = E\boldsymbol{\Psi}. \tag{1.6}$$

In the low-energy limit described by the Dirac equation the two valleys are decoupled, but in real graphene inter-valley scattering can occur by potential features which are sharp on the atomic scale.

The Dirac equation gives rise to unusual transport properties. Because the speed of Dirac particles is independent of their energy,

---

[1] The true spin degree of freedom of electrons is still missing, but it only weakly coupled to the dynamics and can be ignored.
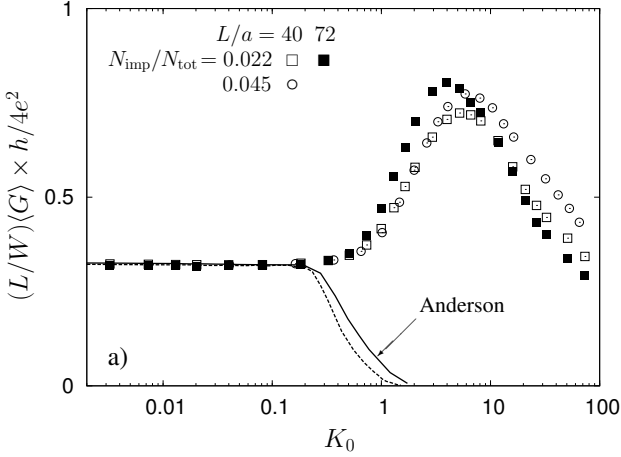
Figure 1.4: Computer simulation showing the dependence of the average conductance $\langle G \rangle$ of a graphene sheet (length L, width W) on the dimensionless disorder strength K_0. The data points are for different sample sizes and number of impurities N_{imp} per total number of lattice points N_{tot}. The conductance increases initially with increasing disorder strength, while in a conventional metal Anderson localization would suppress the conductance (solid and dashed curves). For strong disorder strengths intervalley scattering sets in, resulting in a suppression of the conductance. Figure from Ref. [116].

they cannot be stopped by a potential barrier [34, 64]. This has surprising consequences: adding disorder which is smooth on the scale of atoms to a graphene sample can enhance the conductivity [116] (Fig. 1.4). This behavior is in contrast to that of conventional metals, where disorder reduces the conductivity.

The deviations from normal diffusion in these systems have a quantum mechanical origin in the interference of electron waves. In conventional metals the interference is destructive on average, leading to a complete suppression of diffusion on long length

scales. This is the celebrated localization effect discovered by Philip Anderson in 1957 [9]. For Dirac fermions the interference is constructive on average, which is at the origin of the enhanced conductivity seen in Fig. 1.4.

1.3 Shot noise of subdiffusion

Conductance, the ratio between applied voltage and the resulting time-averaged current, is the basic quantity measured in electronic transport experiments. How does the conductance of a diffusive d-dimensional system scale with its linear size L? For normal diffusion, the answer is given by Ohm's law,

$$G = \sigma L^{d-2}. \tag{1.7}$$

The proportionality constant σ is the conductivity.

Transport by anomalous diffusion is fundamentally different: the conductance depends on L with a different power than in Eq. 1.7. As a consequence, the conductivity becomes scale dependent.

In the case of subdiffusion on fractals the conductance scales as (reviewed in Refs. [135, 111])

$$G \propto L^{d_f - 2/\gamma}, \tag{1.8}$$

with γ the exponent that governs the mean-square displacement in Eq. (1.2). Note that diffusion on a fractal is not just *normal* diffusion in a medium with non-integer dimension d_f. In that case, one would expect G to scale as $L^{d_f - 2}$. Because γ is smaller than 1 for subdiffusion, conduction is suppressed stronger than would be expected solely on the basis of the fractal dimension.

Given the special scaling of conductance with length for subdiffusion, one might ask how other transport properties scale. While the time-averaged current determines the conductance, the time-dependent fluctuations determine the shot noise power S. In terms of the charge Q transmitted in a time τ, one has

$$S = \lim_{\tau \to \infty} 2 \left\langle \delta Q^2 \right\rangle / \tau. \tag{1.9}$$

The shot noise power is proportional to the applied voltage and hence to the mean current

$$I = \lim_{\tau \to \infty} \langle Q \rangle / \tau. \qquad (1.10)$$

The ratio $F = S/2eI$ is called the Fano factor. The Fano factor is unity in the case where completely uncorrelated particles are transmitted. Then, Q is Poisson-distributed which leads to $F = 1$. A value $F > 1$ indicates bunching of charge carriers (particles tend to arrive in groups more often than in the uncorrelated case), whereas $F < 1$ is a signature of anti-bunching (particles arrive less often in groups). Anti-bunching of electrons is a consequence of the Pauli exclusion principle, which prevents two electrons to occupy the same quantum mechanical state. For normal diffusion the Pauli principle produces a Fano factor $F = 1/3$ [18, 96].

What is the Fano factor for subdiffusion on fractals? Shot noise on fractals has been studied previously under circumstances that the Pauli principle is not operative, because the average occupation of a quantum state is much smaller than unity. (This is called a nondegenerate electron gas.) One example is the regime of high-voltage transport modeled by hopping conduction. Then I and S scale differently with L, so that the Fano factor is scale dependent. (See Fig. 1.5.) The Pauli principle is expected to govern the shot noise for diffusive conduction in the regime of low voltages and low temperatures, when the average occupation of a quantum state is of order unity (a degenerate electron gas).

This regime has become experimentally relevant in view of the discovery of electron and hole puddles in undoped graphene [89]. The puddles, shown in Fig. 1.6, form intertwined maze-shaped clusters doped positively (p) or negatively (n). The n-type region contains a degenerate electron gas and the p-type region contains a degenerate hole gas. The current flows with less resistance within an n-type or p-type region than across a p-n interface. Cheianov et al. modeled [89] this system by a random resistor network as illustrated in Fig. 1.7. The interconnected resistors in this model form *percolation clusters* which are fractals with $d_f = 91/48$.
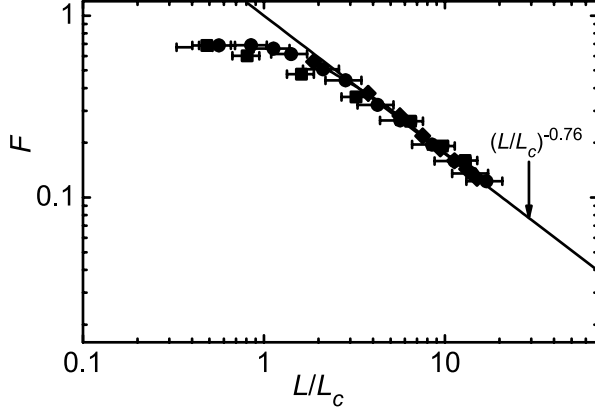
Figure 1.5: Fano factor as function of sample size from a Monte Carlo simulation of two-dimensional hopping through a disordered conductor. The Fano factor is scale dependent because the average current and the noise power scale with a different power of the sample size. Figure from Ref. [68].

Several experiments have studied the Fano factor of graphene recently. Measurements from two of these experiments, performed by Danneau et al. in Helsinki [37] and by DiCarlo et al. in Harvard [41] are shown in Figs. 1.8 and 1.9, respectively. In the Helsinki experiment the Fano factor depends strongly on doping, with a peak value of 1/3, while the Harvard measurements show a doping-independent Fano factor of 1/3. The theory for shot noise on a fractal developed in this thesis offers a way to reconcile these two conflicting experiments.

1.4 Discretization of the Dirac equation

The standard model for graphene is the tight-binding approximation, in which the hopping of electrons between overlapping orbitals of the atoms constituting the carbon sheet is directly con-
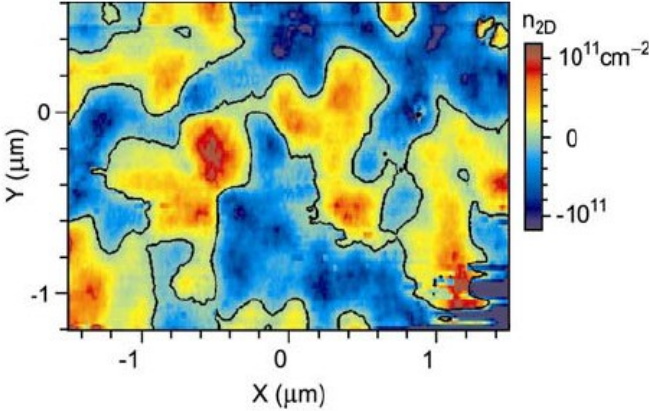
Figure 1.6: Experimentally determined color map of the spatial carrier density variations in a graphene flake. Blue regions correspond to hole doping (p-type) and red regions to electron doping (n-type). The black contour marks the p-n interface. Figure from Ref. [89].

sidered. This model is widely used to study the properties of graphene numerically. It can recover all electronic properties of the material, but is viable for small flakes only, as the computation times grow quickly with the number of atoms. To allow computer modeling of larger flakes of graphene and to probe the physics of a single Dirac cone, it would be useful to simulate the Dirac equation (1.4) directly, and not only as the low-energy limit of the tight-binding model. For this, the Dirac equation needs to be discretized, i.e. put on a lattice. This can be done in real space or in momentum space. The momentum space approach was developed in Refs. [13] and [99], while the real-space approach is developed in this thesis.

The discretization of the Dirac equation is notoriously difficult, because of the socalled *fermion doubling problem* [98]. The most straightforward way to discretize the Dirac equation in real space is to define the wave function $\psi(x, y)$ on a rectangular grid with lattice
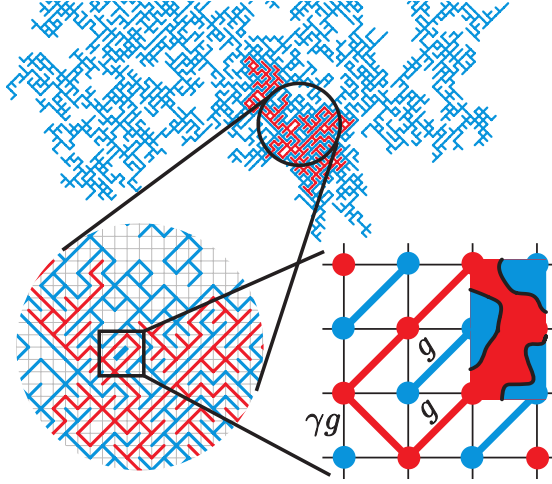
Figure 1.7: Random resistor network representation of a graphene sheet with average zero doping. The conductance is g within an n-type or p-type region (red or blue lines), and has a smaller value across a p-n interface. (The symbol γ used in this figure is unrelated to the random-walk exponent.) Figure from Ref. [35].

constant a and to replace the derivatives with finite differences,

$$\partial_x \psi \rightarrow \frac{\psi(x+a,y) - \psi(x-a,y)}{2a}, \tag{1.11}$$

$$\partial_y \psi \rightarrow \frac{\psi(x,y+a) - \psi(x,y-a)}{2a}. \tag{1.12}$$

This discretization fails to describe the physics of a single Dirac cone.

To see this, let us look at the dispersion relation of the discretized equation. For simplicity, we consider only plane waves moving in the x direction, so that $k_y = 0$. Such plane waves have the general form

$$\psi = \psi_0 \, e^{\pm i k_x x}. \tag{1.13}$$

Inserting this into the Dirac equation (1.4) with the substitutions
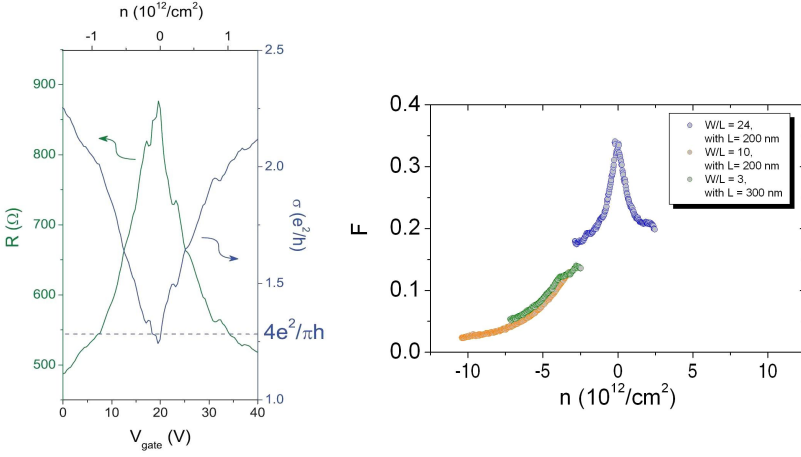
Figure 1.8: Results from a transport experiment performed by R. Danneau et al. on a graphene sheet. The measurements are consistent with theoretical predictions for ballistic transport at the Dirac point [141]. Left panel: Resistance and conductivity as a function of gate voltage and charge carrier density. The conductivity at the Dirac point reaches the expected value $4e^2/\pi h$. Right panel: Fano factor as function of charge carrier density. At the Dirac point, the value $1/3$ is reached with F falling off for both positive and negative doping. Figures from Ref. [37].

(1.11) and (1.12) gives the dispersion relation

$$E = \pm \frac{\hbar v}{a} \sin ka, \tag{1.14}$$

plotted as the solid curve of Fig. 1.10.

We see that unphysical low-energy states, forming a second Dirac cone, have appeared around $k_x a = \pm\pi, k_y = 0$. There are two additional cones, one around $k_x a = 0, k_y a = \pm\pi$, and one around $k_x a = \pm\pi, k_y a = \pm\pi$, giving four in total in the first Brillouin zone. These additional states are due to the fact that the
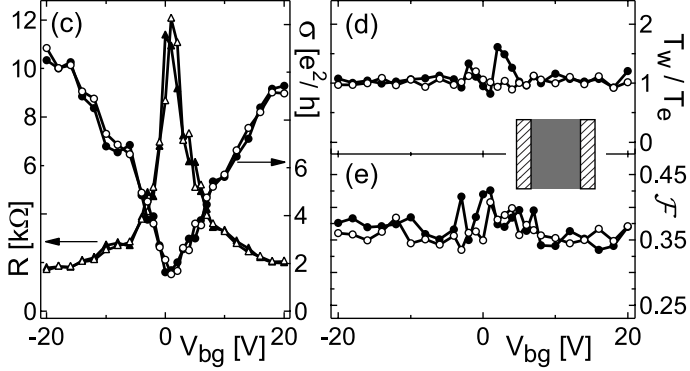
Figure 1.9: Results from a transport experiment performed by Di-Carlo et al. on a graphene sheet. Left panel: Resistance and conductivity as function of gate voltage. Right panel, lower part: Fano factor as function of gate voltage. The Fano factor has the value 1/3 independent of doping. Figure from Ref. [41].

Dirac equation (1.4) is a first order differential equation. To be able to evaluate the first derivatives at the same discretization points as the wave function, we had to take differences over two lattice sites in the difference operators (1.11) and (1.12). As a consequence, waves with a spatial period $2\pi/|k_x|$ below $4a$ are undersampled. This problem is specific for massless Dirac fermions. It does not arise for the Schrödinger equation, which massive fermions obey, as it is second order in space.

The fermion doubling problem also plagues the discretization of the Dirac equation in relativistic quantum mechanics. There exist ways to circumvent it by shifting the energy of the doubled states away from 0. One such method, the method of Wilson fermions [147], gives a mass to the Dirac fermions and thereby breaks a fundamental symmetry (socalled symplectic symmetry) needed to explain transport properties in graphene. An alternative method, known as the method of Kogut-Susskind fermions or as the staggered fermion method [71, 134, 22], preserves the symplec-
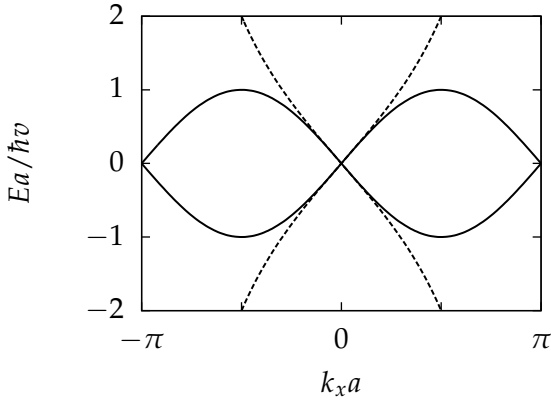
Figure 1.10: Solid curve: dispersion relation of the naively discretized Dirac equation showing *fermion doubling*: a second Dirac cone appears at $k_x = \pm\pi$. Dashed curve: dispersion relation of the Dirac equation discretized according to the method of staggered fermions. The energy of the unphysical states at $k_x = \pm\pi$ has been shifted away to $\pm\infty$.

tic symmetry and is therefore the method which we will apply to graphene.

The dashed curve of Fig. 1.10 shows the dispersion relation of the Dirac equation discretized according to the staggered fermion method. The spurious Dirac cone has disappeared.

1.5 Topological insulators

In 1980 Klaus von Klitzing discovered that the conductance of thin semiconductor layers at low temperatures and large perpendicular magnetic fields is quantized in integer multiples of the conductance quantum e^2/h [69]. The mechanism for this *quantum Hall effect* is illustrated in the left panel of Fig. 1.11 and can be described as follows: Under the influence of the magnetic field the
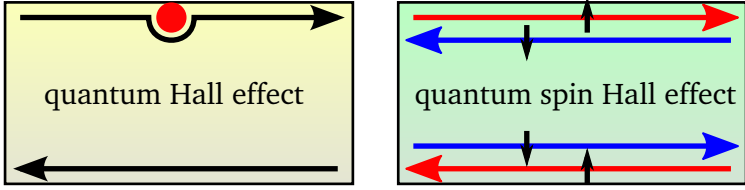
Figure 1.11: Left panel: the quantum Hall effect has a single conducting channel along the edge. Because movement in the channel is only possible in a single direction, electrons cannot be scattered back by impurities (an impurity is symbolized by the red dot). Right panel: the quantum spin Hall effect has two spin-polarized channels per edge of opposite spin (the spin orientation is indicated by the short black arrows), propagating in opposite directions. Backscattering is now forbidden by Kramers theorem.

electrons move in quantized circular orbits (Landau levels), making the bulk of the sample insulating. Electrons at the edges of the samples cannot perform full circles and are forced to "skip along the edge". This leads to the appearance of conducting edge states which propagate in a single direction only. Backscattering requires scattering to the opposite edge, which is strongly suppressed if the sample is sufficiently wide. Due to the absence of backscattering, the transmission probability is unity for each edge channel at the Fermi level. Each fully transmitted edge channel contributes e^2/h to the conductance, leading to the observed quantization.

An analogous quantization of the conductance in zero magnetic field occurs in a new class of materials known as topological insulators [50, 108]. This socalled *quantum spin Hall effect* requires spin-orbit coupling to produce an unusual band structure (shown schematically in Fig. 1.12) that leads to the appearance of an insulating bulk and conducting edge channels. There are now two counterpropagating edge channels at each edge, so backscattering

would not require scattering to the opposite edge. The reason that backscattering is still forbidden is a rather subtle consequence of time reversal symmetry.

Since a magnetic field is absent, the system is time reversal invariant – its Hamiltonian H is unchanged by the anti-unitary time-reversal operator Θ:

$$\Theta H \Theta^{-1} = H. \tag{1.15}$$

Because the electrons have spin $1/2$, the operator Θ^2 is equal to -1. In this case, Kramers theorem states that all electron states are at least twofold degenerate: Let us consider a state ψ at energy E,

$$H\psi = E\psi. \tag{1.16}$$

Because of Eq. (1.15), the state $\Theta\psi$ has the same energy E as ψ. The state $\Theta\psi$ cannot be equivalent to ψ, as assuming that $\Theta\psi$ differs from ψ just by a phase factor $e^{i\delta}$ leads to

$$\Theta^2\psi = \Theta e^{i\delta}\psi = e^{-i\delta}\Theta\psi = e^{-i\delta}e^{i\delta}\psi = \psi, \tag{1.17}$$

which contradicts the previously stated $\Theta^2 = -1$. (The second equality in Eq. (1.17) is due to Θ being antiunitary.)

Kramers theorem tells us that there should be at least two states at each energy. This forbids scattering between the counterpropagating edge channels, because that would remove the crossing at zero momentum in Fig. 1.12 and thus remove the degeneracy.

The spectrum near the crossing looks similar to that near the Dirac point in graphene (cf. Fig. 1.10), and indeed, the electrons moving in the edge channels are governed by a one-dimensional version of the Dirac equation (1.4). Topological insulators are therefore an alternative source of Dirac fermions and many of the techniques developed in the study of graphene can be applied to this new class of materials.
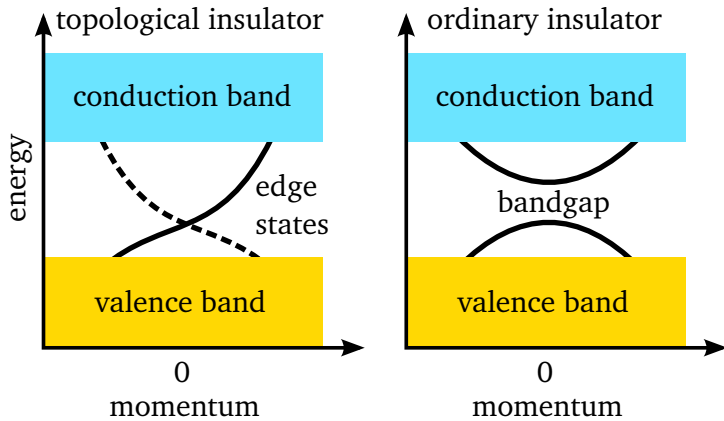
Figure 1.12: Schematic comparison of the band structure of a topological insulator (left panel) and an ordinary insulator (right panel). Both have an insulating bulk, but the topological insulator has conducting edge states inside the band gap. The crossing of the edge states cannot be avoided because that would violate Kramers theorem (requiring twofold degenerate energy levels).

1.6 Outline of this thesis

The research presented in the following chapters concerns the anomalous diffusion of particles in general and Dirac fermions in particular. One area of focus are the implications of anomalous diffusion for electronic shot noise. Novel methods for simulation of Dirac fermions (which might exhibit anomalous diffusion) were developed. Finally, some aspects of transport of Dirac fermions in topological insulators were studied numerically and analytically.

Chapter 2: Electronic shot noise in fractal conductors

Motivated by the experiments mentioned in Sec. 1.3, in Chapter 2 we study the shot noise of subdiffusion on fractals. The two kinds of fractals we consider are the Sierpiński gasket (a regular fractal)

and random planar resistor networks which arise from a model of graphene. We determine the scaling with size L of the shot noise power S due to elastic scattering in a fractal conductor. We find a power-law scaling $S \propto L^{d_f - 2/\gamma}$, with an exponent depending on the fractal dimension d_f and the anomalous diffusion exponent[2] γ. This is the same scaling as the time-averaged current I, which implies that the Fano factor $F = S/2eI$ is scale independent. We obtain a value $F = 1/3$ for anomalous diffusion that is the same as for normal diffusion, even if there is no smallest length scale below which the normal diffusion equation holds. The fact that F remains fixed at $1/3$ as one crosses the percolation threshold in a random-resistor network may explain measurements of a doping-independent Fano factor in a graphene flake [41].

Chapter 3: Nonalgebraic length dependence of transmission through a chain of barriers with a Lévy spacing distribution

In Chapter 3 we analyze transport through a linear chain of barriers with independent spacings s drawn from a heavy-tailed Lévy distribution. We are motivated by the recent realization of a "Lévy glass" [15] (a three-dimensional optical material with a Lévy distribution of scattering lengths) of which our system is a one-dimensional analogue. The step length distribution of particles in our system also has a heavy tail, $P(s) \propto s^{-1-\alpha}$ for $s \to \infty$, but strong correlations exist between subsequent steps because the same space between two barriers will often be traversed back after a particle gets scattered by a barrier. We show that a random walk along such a sparse chain is not a Lévy walk because of these correlations. Thus, by working in the lowest possible dimension, we can provide a worst-case estimate for the effect of the correlations in higher dimensions.

  We calculate all moments of conductance (or transmission), in the regime of incoherent sequential tunneling through the barriers.

---

[2]In Chapter 2 the symbol α is used for a differently defined anomalous diffusion exponent: $\alpha = 1/\gamma - 2$.

The average transmission from one barrier to a point at a distance L scales as $L^{-\alpha}\ln L$ for $0 < \alpha < 1$. The corresponding electronic shot noise has a Fano factor that approaches $1/3$ very slowly, with $1/\ln L$ corrections.

Chapter 4: Finite difference method for transport properties of massless Dirac fermions

As shown in Sec. 1.4, a straightforward discretization of the massless Dirac equation fails because of the fermion doubling problem. In Chapter 4 we adapt a finite difference method of solution, developed in the context of lattice gauge theory, to the calculation of electrical conduction in a graphene sheet or on the surface of a topological insulator. The discretized Dirac equation retains a single Dirac point (no fermion doubling), avoids intervalley scattering as well as trigonal warping (a triangular distortion of the conical band structure that breaks the momentum inversion symmetry), and thus preserves the single-valley time reversal symmetry (= symplectic symmetry) at all length scales and energies. This comes at the expense of a nonlocal finite difference approximation of the differential operator. We demonstrate the symplectic symmetry by calculating the scaling of the conductivity with sample size, obtaining the logarithmic increase due to antilocalization. We also calculate the sample-to-sample conductance fluctuations as well as the shot noise power, and compare with analytical predictions.

Our numerical results are in good agreement with a recent theory of transport in smoothly disordered graphene by Schuessler et al. [122]. Fig. 1.13 compares their analytical results (solid curve) with our numerical data (rectangles). The same numerical results were used to prepare Fig. 4.12.
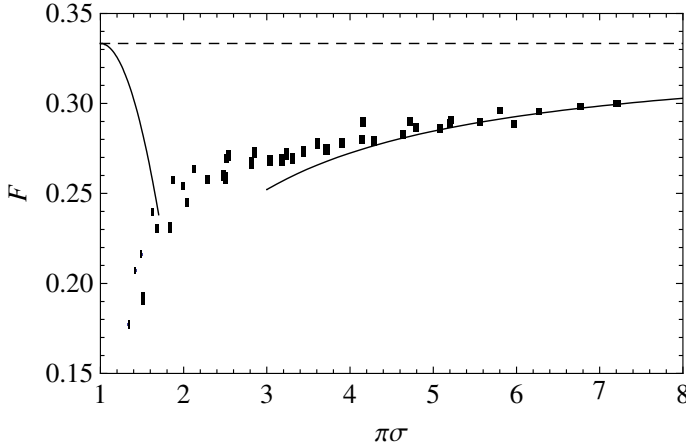
Figure 1.13: Fano factor as a function of conductivity for smoothly disordered graphene. The solid curves show ballistic and diffusive results of Ref. [122]. The dashed line corresponds to the asymptotic value $F = 1/3$. The solid rectangles are our numerical results, obtained with the method of Chapter 4. The size of rectangles corresponds to the statistical error estimate. Figure from Ref. [122].

Chapter 5: Switching of electrical current by spin precession in the first Landau level of an inverted-gap semiconductor

In Chapter 5 we show how the quantum Hall effect in a two-dimensional topological insulator can be used to inject, precess, and detect the electron spin along a one-dimensional pathway. The restriction of the electron motion to a single spatial dimension ensures that all electrons experience the same amount of precession in a parallel magnetic field, so that the full electrical current can be switched on and off. As an example, we calculate the magnetoconductance of a *p-n* interface in a HgTe quantum well and show how it can be used to measure the spin precession due to bulk inversion asymmetry. A realization of this experiment would

provide a unique demonstration of full-current switching by spin precession.

Chapter 6: Theory of the topological Anderson insulator

In Chapter 6 we present an effective medium theory that explains the disorder-induced transition into a phase of quantized conductance, discovered in computer simulations of HgTe quantum wells [81]. Depending on the width of their innermost layer, such quantum wells are two-dimensional topological insulators or ordinary insulators. Our theory explains how the combination of a random potential and quadratic corrections $\propto p^2 \sigma_z$ to the Dirac Hamiltonian can drive an ordinary band insulator into a topological insulator (having conducting edge states). We calculate the location of the phase boundary at weak disorder and show that it corresponds to the crossing of a band edge rather than a mobility edge. Our mechanism for the formation of a topological Anderson insulator is generic, and would apply as well to three-dimensional semiconductors with strong spin-orbit coupling. It has indeed been adapted to that case recently [49].

2 Electronic shot noise in fractal conductors

2.1 Introduction

Diffusion in a medium with a fractal dimension is characterized by an anomalous scaling with time t of the root-mean-squared displacement Δ. The usual scaling for integer dimensionality d is $\Delta \propto t^{1/2}$, independent of d. If the dimensionality d_f is noninteger, however, an anomalous scaling

$$\Delta \propto t^{1/(2+\alpha)} \tag{2.1}$$

with $\alpha > 0$ may appear. This anomaly was discovered in the early 1980's [144, 7, 21, 46, 109] and has since been studied extensively (see Refs. [53, 57] for reviews). Intuitively, the slowing down of the diffusion can be understood as arising from the presence of obstacles at all length scales – characteristic of a selfsimilar fractal geometry.

A celebrated application of the theory of fractal diffusion is to the scaling of electrical conduction in random-resistor networks (reviewed in Refs. [135, 111]). According to Ohm's law, the conductance G should scale with the linear size L of a d-dimensional network as $G \propto L^{d-2}$. In a fractal dimension the scaling is modified to $G \propto L^{d_f-2-\alpha}$, depending both on the fractal dimensionality d_f and on the anomalous diffusion exponent α. At the percolation threshold, the known [53] values for $d = 2$ are $d_f = 91/48$ and $\alpha = 0.87$, leading to a scaling $G \propto L^{-0.97}$. This almost inverse-linear scaling of the conductance of a planar random-resistor network

contrasts with the L-independent conductance $G \propto L^0$ predicted by Ohm's law in two dimensions.

All of this body of knowledge applies to classical resistors, with applications to disordered semiconductors and granular metals [128, 29]. The quantum Hall effect provides one quantum mechanical realization of a random-resistor network [140], in a rather special way because time-reversal symmetry is broken by the magnetic field. Recently [35], Cheianov, Fal'ko, Altshuler, and Aleiner announced an altogether different quantum realization in zero magnetic field. Following experimental [89] and theoretical [56] evidence for electron and hole puddles in undoped graphene[1], Cheianov et al. modeled this system by a degenerate electron gas[2] in a random-resistor network. They analyzed both the high-temperature classical resistance, as well as the low-temperature quantum corrections, using the anomalous scaling laws in a fractal geometry.

These recent experimental and theoretical developments open up new possibilities to study quantum mechanical aspects of fractal diffusion, both with respect to the Pauli exclusion principle and with respect to quantum interference (which are operative in distinct temperature regimes). To access the effect of the Pauli principle one needs to go beyond the time-averaged current $\bar{I}$ (studied by Cheianov et al. [35]), and consider the time-dependent fluctuations $\delta I(t)$ of the current in response to a time-independent applied voltage V. These fluctuations exist because of the granularity of the electron charge, hence their name "shot noise" (for reviews, see

---

[1]Graphene is a single layer of carbon atoms, forming a two-dimensional honeycomb lattice. Electrical conduction is provided by overlapping π-orbitals, with on average one electron per π-orbital in undoped graphene. Electron puddles have a little more than one electron per π-orbital (n-type doping), while hole puddles have a little less than one electron per π-orbital (p-type doping).

[2]An electron gas is called "degenerate" if the average occupation number of a quantum state is either close to unity or close to zero. It is called "nondegenerate" if the average occupation number is much smaller than unity for all states.

Refs. [24, 19]). Shot noise is quantified by the noise power

$$P = 2 \int_{-\infty}^{\infty} dt \, \langle \delta I(0) \delta I(t) \rangle \qquad (2.2)$$

and by the Fano factor $F = P/2e\bar{I}$. The Pauli principle enforces $F < 1$, meaning that the noise power is smaller than the Poisson value $2e\bar{I}$ – which is the expected value for independent particles (Poisson statistics).

The investigation of shot noise in a fractal conductor is particularly interesting in view of two different experimental results [41, 37] that have been reported. Both experiments measure the shot noise power in a graphene flake and find $F < 1$. A calculation [141] of the effect of the Pauli principle on the shot noise of undoped graphene predicted $F = 1/3$ in the absence of disorder, with a rapid suppression upon either p-type or n-type doping. This prediction is consistent with the experiment of Danneau et al. [37], but the experiment of DiCarlo et al. [41] gives instead an approximately *doping-independent F* near 1/3. Computer simulations [118, 80] suggest that disorder in the samples of DiCarlo et al. might cause the difference.

Motivated by this specific example, we study here the fundamental problem of shot noise due to anomalous diffusion in a fractal conductor. While *equilibrium* thermal noise in a fractal has been studied previously [110, 51, 43], it remains unknown how anomalous diffusion might affect the *nonequilibrium* shot noise. Existing studies [77, 31, 68] of shot noise in a percolating network were in the regime where *inelastic* scattering dominates, leading to hopping conduction, while for diffusive conduction we need predominantly *elastic* scattering.

2.2 Results and discussion

We demonstrate that anomalous diffusion affects P and $\bar{I}$ in such a way that the Fano factor (their ratio) becomes scale independent as well as independent of d_f and α. Anomalous diffusion, therefore,

produces the same Fano factor $F = 1/3$ as is known [18, 96] for normal diffusion. This is a remarkable property of diffusive conduction, given that hopping conduction in a percolating network does not produce a scale-independent Fano factor [77, 31, 68]. Our general findings are consistent with the doping independence of the Fano factor in disordered graphene observed by DiCarlo et al. [41].

To arrive at these conclusions we work in the experimentally relevant regime where the temperature T is sufficiently high that the phase coherence length is $\ll L$, and sufficiently low that the inelastic length is $\gg L$. Quantum interference effects can then be neglected, as well as inelastic scattering events. The Pauli principle remains operative if the thermal energy kT remains well below the Fermi energy, so that the electron gas remains degenerate.

We first briefly consider the case that the anomalous diffusion on long length scales is preceded by normal diffusion on short length scales. This would apply, for example, to a percolating cluster of electron and hole puddles with a mean free path l which is short compared to the typical size a of a puddle. We can then rely on the fact that $F = 1/3$ for a conductor of any shape, provided that the normal diffusion equation holds locally [97, 136], to conclude that the transition to anomalous diffusion on long length scales must preserve the one-third Fano factor.

This simple argument cannot be applied to the more typical class of fractal conductors in which the normal diffusion equation does not hold on short length scales. As representative for this class, we consider fractal lattices of sites connected by tunnel barriers. The local tunneling dynamics then crosses over into global anomalous diffusion, without an intermediate regime of normal diffusion.

2.2.1 Sierpiński lattice

A classic example is the Sierpiński lattice [130] shown in Fig. 2.1 (inset). Each site is connected to four neighbors by bonds that represent the tunnel barriers, with equal tunnel rate Γ through each

barrier. The fractal dimension is $d_f = \log_2 3$ and the anomalous diffusion exponent is [53] $\alpha = \log_2(5/4)$. The Pauli exclusion principle can be incorporated as in Ref. [84], by demanding that each site is either empty or occupied by a single electron. Tunneling is therefore only allowed between an occupied site and an adjacent empty site. A current is passed through the lattice by connecting the lower left corner to a source (injecting electrons so that the site remains occupied) and the lower right corner to a drain (extracting electrons so that the site remains empty). The resulting stochastic sequence of current pulses is the "tunnel exclusion process" of Ref. [112].

The statistics of the current pulses can be obtained exactly (albeit not in closed form) by solving a master equation [12]. We have calculated the first two cumulants by extending to a two-dimensional lattice the one-dimensional calculation of Ref. [112]. To manage the added complexity of an extra dimension we found it convenient to use the Hamiltonian formulation of Ref. [119]. The hierarchy of linear equations that we need to solve in order to obtain $\bar{I}$ and P is derived in the appendix.

The results in Fig. 2.1 demonstrate, firstly, that the shot noise power P scales as a function of the size L of the lattice with the same exponent $d_f - 2 - \alpha = \log_2(3/5)$ as the conductance; and, secondly, that the Fano factor F approaches $1/3$ for large L. More precisely, see Fig. 2.2, we find that $F - 1/3 \propto L^{-1.5}$ scales to zero as a power law, with $F - 1/3 < 10^{-4}$ for our largest L.

2.2.2 Percolating network

Turning now to the application to graphene mentioned in the introduction, we have repeated the calculation of shot noise and Fano factor for the random-resistor network of electron and hole puddles introduced by Cheianov et al. [35]. The results, shown in Fig. 2.3, demonstrate that the shot noise power P scales with the same exponent $L^{-0.97}$ as the conductance G (solid lines in the lower panel), and that the Fano factor F approaches $1/3$ for

large networks (upper panel). This is a random, rather than a deterministic fractal, so there remains some statistical scatter in the data, but the deviation of F from $1/3$ for the largest lattices is still $< 10^{-3}$ (see the circular data points in Fig. 2.2).

2.3 Conclusion

In conclusion, we have found that the universality of the one-third Fano factor, previously established for normal diffusion [18, 96, 97, 136], extends to anomalous diffusion as well. This universality might have been expected with respect to the fractal dimension d_f (since the Fano factor is dimension independent), but we had not expected universality with respect to the anomalous diffusion exponent α. The experimental implication of the universality is that the Fano factor remains fixed at $1/3$ as one crosses the percolation threshold in a random-resistor network – thereby crossing over from anomalous diffusion to normal diffusion. This is consistent with the doping-independent Fano factor measured in a graphene flake by DiCarlo et al. [41].

Appendix 2.A   Calculation of the Fano factor for the tunnel exclusion process on a two-dimensional network

Here we present the method we used to calculate the Fano factor for the tunnel exclusion process in the Sierpiński lattice and in the random-resistor network. We follow the master equation approach of Refs. [112, 12]. The two-dimensionality of our networks requires a more elaborate bookkeeping, which we manage by means of the Hamiltonian formalism of Ref. [119].

2.A.1 Counting statistics

We consider a network of N sites, each of which is either empty or singly occupied. Two sites are called adjacent if they are directly connected by at least one bond. A subset $\mathcal{S}$ of the N sites is connected to the source and a subset $\mathcal{D}$ is connected to the drain. Each of the 2^N possible states of the network is reached with a certain probability at time t. We store these probabilities in the 2^N-dimensional vector $|P(t)\rangle$. Its time evolution in the tunnel exclusion process is given by the master equation

$$\frac{d}{dt}|P(t)\rangle = M|P(t)\rangle, \tag{2.3}$$

where the matrix M contains the tunnel rates. The normalization condition can be written as $\langle\Sigma|P\rangle = 1$, in terms of a vector $\langle\Sigma|$ that has all 2^N components equal to 1. This vector is a left eigenstate of M with zero eigenvalue

$$\langle\Sigma|M = 0, \tag{2.4}$$

because every column of M must sum to zero in order to conserve probability. The right eigenstate with zero eigenvalue is the stationary distribution $|P_\infty\rangle$. All other eigenvalues of M have a real part < 0.

We store in the vector $|P(t, Q)\rangle$ the conditional probabilities that a state is reached at time t after precisely Q charges have entered the network from the source. Because the source remains occupied, a charge which has entered the network cannot return back to the source but must eventually leave through the drain. One can therefore use Q to represent the number of transfered charges. The time evolution of $|P(t, Q)\rangle$ reads

$$\frac{d}{dt}|P(t,Q)\rangle = M_0|P(t,Q)\rangle + M_1|P(t,Q-1)\rangle, \tag{2.5}$$

where $M = M_0 + M_1$ has been decomposed into a matrix M_0 containing all transitions by which Q does not change and a matrix M_1 containing all transitions that increase Q by 1.

The probability $\langle\Sigma|P(t,Q)\rangle$ that Q charges have been transferred through the network at time t represents the counting statistics. It describes the entire statistics of current fluctuations. The cumulants

$$C_n = \left.\frac{\partial^n S(t,\chi)}{\partial\chi^n}\right|_{\chi=0} \tag{2.6}$$

are obtained from the cumulant generating function

$$S(t,\chi) = \ln\left[\sum_Q \langle\Sigma|P(t,Q)\rangle\, e^{\chi Q}\right]. \tag{2.7}$$

The average current and Fano factor are given by

$$\bar{I} = \lim_{t\to\infty} C_1/t, \quad F = \lim_{t\to\infty} C_2/C_1. \tag{2.8}$$

The cumulant generating function (2.7) can be expressed in terms of a Laplace transformed probability vector $|P(t,\chi)\rangle = \sum_Q |P(t,Q)\rangle\, e^{\chi Q}$ as

$$S(t,\chi) = \ln\langle\Sigma|P(t,\chi)\rangle. \tag{2.9}$$

Transformation of Eq. (2.5) gives

$$\frac{d}{dt}|P(t,\chi)\rangle = M(\chi)|P(t,\chi)\rangle, \tag{2.10}$$

where we have introduced the counting matrix

$$M(\chi) = M_0 + e^\chi M_1. \tag{2.11}$$

The cumulant generating function follows from

$$S(t,\chi) = \ln\langle\Sigma|e^{tM(\chi)}|P(0,\chi)\rangle. \tag{2.12}$$

The long-time limit of interest for the Fano factor can be implemented as follows [12]. Let $\mu(\chi)$ be the eigenvalue of $M(\chi)$ with the largest real part, and let $|P_\infty(\chi)\rangle$ be the corresponding (normalized) right eigenstate,

$$M(\chi)|P_\infty(\chi)\rangle = \mu(\chi)|P_\infty(\chi)\rangle, \tag{2.13}$$
$$\langle\Sigma|P_\infty(\chi)\rangle = 1. \tag{2.14}$$

Since the largest eigenvalue of $M(0)$ is zero, we have

$$M(0) |P_\infty(0)\rangle = 0 \Leftrightarrow \mu(0) = 0. \tag{2.15}$$

(Note that $|P_\infty(0)\rangle$ is the stationary distribution $|P_\infty\rangle$ introduced earlier.) In the limit $t \to \infty$ only the largest eigenvalue contributes to the cumulant generating function,

$$\lim_{t\to\infty} \frac{1}{t} S(t,\chi) = \lim_{t\to\infty} \frac{1}{t} \ln\left[e^{t\mu(\chi)} \langle\Sigma|P_\infty(\chi)\rangle \right] = \mu(\chi). \tag{2.16}$$

2.A.2 Construction of the counting matrix

The construction of the counting matrix $M(\chi)$ is simplified by expressing it in terms of raising and lowering operators, so that it resembles a Hamiltonian of quantum mechanical spins [119]. First, consider a single site with the basis states $|0\rangle = \binom{1}{0}$ (vacant) and $|1\rangle = \binom{0}{1}$ (occupied). We define, respectively, raising and lowering operators

$$s^+ = \begin{pmatrix} 0 & 0 \\ 1 & 0 \end{pmatrix}, \quad s^- = \begin{pmatrix} 0 & 1 \\ 0 & 0 \end{pmatrix}. \tag{2.17}$$

We also define the electron number operator $n = s^+ s^-$ and the hole number operator $v = \mathbb{1} - n$ (with $\mathbb{1}$ the 2×2 unit matrix). Each site i has such operators, denoted by s_i^+, s_i^-, n_i, and v_i. The matrix $M(\chi)$ can be written in terms of these operators as

$$
\begin{aligned}
M(\chi) = &\sum_{\langle i,j\rangle} \left(s_j^+ s_i^- - v_j n_i \right) \\
&+ \sum_{i\in\mathcal{S}} (e^\chi s_i^+ - v_i) + \sum_{i\in\mathcal{D}} (s_i^- - n_i),
\end{aligned} \tag{2.18}
$$

where all tunnel rates have been set equal to unity. The first sum runs over all ordered pairs $\langle i,j\rangle$ of adjacent sites. These are Hermitian contributions to the counting matrix. The second sum runs over sites in $\mathcal{S}$ connected to the source, and the third sum runs over sites in $\mathcal{D}$ connected to the drain. These are non-Hermitian contributions.

It is easy to convince oneself that $M(0)$ is indeed M of Eq. (2.3), since every possible tunneling event corresponds to two terms in Eq. (2.18): one positive non-diagonal term responsible for probability gain for the new state and one negative diagonal term responsible for probability loss for the old state. In accordance with Eq. (2.11), the full $M(\chi)$ differs from M by a factor e^χ at the terms associated with charges entering the network.

2.A.3 Extraction of the cumulants

In view of Eq. (2.16), the entire counting statistics in the long-time limit is determined by the largest eigenvalue $\mu(\chi)$ of the operator (2.18). However, direct calculation of that eigenvalue is feasible only for very small networks. Our approach, following Ref. [112], is to derive the first two cumulants by solving a hierarchy of linear equations.

We define

$$T_i = \langle \Sigma | \, n_i \, | P_\infty(\chi) \rangle = 1 - \langle \Sigma | \, v_i \, | P_\infty(\chi) \rangle \,, \qquad (2.19)$$
$$U_{ij} = U_{ji} = \langle \Sigma | \, n_i n_j \, | P_\infty(\chi) \rangle \quad \text{for } i \neq j, \qquad (2.20)$$
$$U_{ii} = 2T_i - 1. \qquad (2.21)$$

The value $T_i|_{\chi=0}$ is the average stationary occupancy of site i. Similarly, $U_{ij}|_{\chi=0}$ for $i \neq j$ is the two-point correlator.

We will now express $\mu(\chi)$ in terms of T_i. We start from the definition (2.13). If we act with $\langle \Sigma |$ on the left-hand-side of Eq. (2.13) we obtain

$$
\langle \Sigma | \, M(0) + (e^\chi - 1) \sum_{i \in \mathcal{S}} s_i^+ \, | P_\infty(\chi) \rangle
$$
$$
= (e^\chi - 1) \sum_{i \in \mathcal{S}} \langle \Sigma | \, s_i^+ \, | P_\infty(\chi) \rangle
$$
$$
= (e^\chi - 1) \sum_{i \in \mathcal{S}} \langle \Sigma | \, v_i \, | P_\infty(\chi) \rangle
$$
$$
= (e^\chi - 1) \sum_{i \in \mathcal{S}} (1 - T_i). \qquad (2.22)
$$

In the second equality we have used Eq. (2.4) [which holds since $M \equiv M(0)$]. Acting with $\langle \Sigma|$ on the the right-hand-side of Eq. (2.13) we obtain just $\mu(\chi)$, in view of Eq. (2.14). Hence we arrive at

$$\mu(\chi) = (e^{\chi} - 1) \sum_{i \in \mathcal{S}} (1 - T_i). \tag{2.23}$$

From Eq. (2.23) we obtain the average current and Fano factor in terms of T_i and the first derivative $T_i' = dT_i/d\chi$ at $\chi = 0$,

$$\bar{I} = \lim_{t \to \infty} C_1/t = \mu'(0) = \sum_{i \in \mathcal{S}} (1 - T_i|_{\chi=0}), \tag{2.24}$$

$$F = \lim_{t \to \infty} \frac{C_2}{C_1} = \frac{\mu''(0)}{\mu'(0)} = 1 - \frac{2 \sum_{i \in \mathcal{S}} T_i'|_{\chi=0}}{\sum_{i \in \mathcal{S}} (1 - T_i|_{\chi=0})}. \tag{2.25}$$

Average current

To obtain T_i we set up a system of linear equations starting from

$$\mu(\chi) T_i = \langle \Sigma | n_i M(\chi) | P_{\infty}(\chi) \rangle. \tag{2.26}$$

Commuting n_i to the right, using the commutation relations $[n_i, s_i^+] = s_i^+$ and $[n_i, s_i^-] = -s_i^-$, we find

$$\mu(\chi) T_i = \sum_{j(i)} T_j - k_i T_i + k_{i,\mathcal{S}} + (e^{\chi} - 1) \sum_{l \in \mathcal{S}} (T_i - U_{li}). \tag{2.27}$$

The notation $\sum_{j(i)}$ means that the sum runs over all sites j adjacent to i. The number k_i is the total number of bonds connected to site i; $k_{i,\mathcal{S}}$ of these bonds connect site i to the source.

In order to compute $T_i|_{\chi=0}$ we set $\chi = 0$ in Eq. (2.27), use Eq. (2.15) to set the left-hand-side to zero, and solve the resulting symmetric sparse linear system of equations,

$$-k_{i,\mathcal{S}} = \sum_{j(i)} T_j - k_i T_i. \tag{2.28}$$

This is the first level of the hierarchy. Substitution of the solution into Eq. (2.24) gives the average current $\bar{I}$.

Fano factor

To calculate the Fano factor via Eq. (2.25) we also need $T_i'|_{\chi=0}$. We take Eq. (2.27), substitute Eq. (2.23) for $\mu(\chi)$, differentiate and set $\chi = 0$ to arrive at

$$\sum_{l \in \mathcal{S}} (U_{li} - T_l T_i) - k_{i,\mathcal{S}} = \sum_{j(i)} T_j' - k_i T_i'. \qquad (2.29)$$

To find $U_{ij}|_{\chi=0}$ we note that

$$\mu(\chi) U_{ij} = \langle \Sigma | \, n_i n_j M(\chi) \, | P_\infty(\chi) \rangle \,, \quad i \neq j, \qquad (2.30)$$

and commute n_i to the right. Setting $\chi = 0$ provides the second level of the hierarchy of linear equations,

$$0 = \sum_{l(j),l \neq i} U_{il} + \sum_{l(i),l \neq j} U_{jl} - (k_i + k_j - 2d_{ij}) U_{ij}$$

$$+ k_{j,\mathcal{S}} T_i + k_{i,\mathcal{S}} T_j, \quad i \neq j. \qquad (2.31)$$

The number d_{ij} is the number of bonds connecting sites i and j if they are adjacent, while $d_{ij} = 0$ if they are not adjacent.
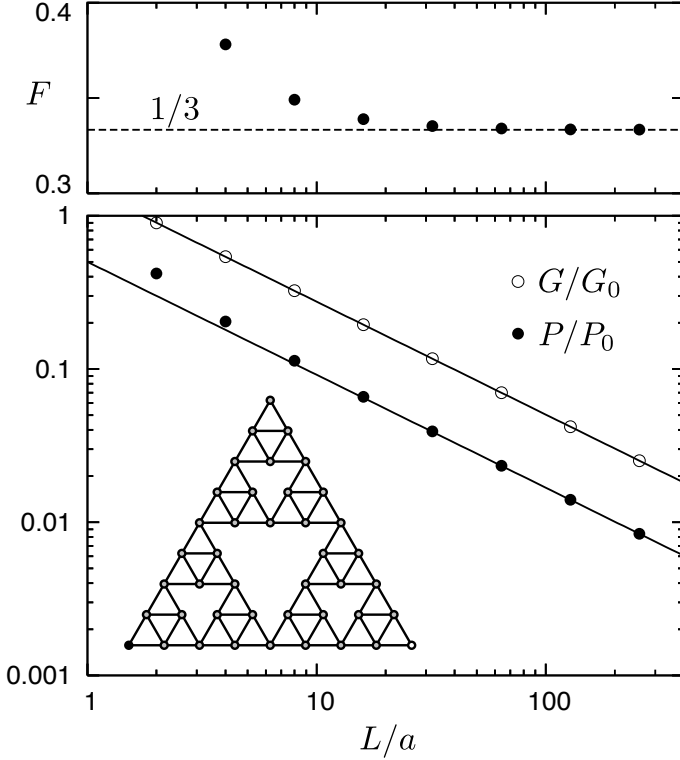
Figure 2.1: Lower panel: Electrical conduction through a Sierpiński lattice. This is a deterministic fractal, constructed by recursively removing a central triangular region from an equilateral triangle. The recursion level r quantifies the size $L = 2^r a$ of the fractal in units of the elementary bond length a (the inset shows the fourth recursion). The conductance $G = \bar{I}/V$ (open dots, normalized by the tunneling conductance G_0 of a single bond) and shot noise power P (filled dots, normalized by $P_0 = 2eVG_0$) are calculated for a voltage difference V between the lower-left and lower-right corners of the lattice. Both quantities scale as $L^{d_f - 2 - \alpha} = L^{\log_2(3/5)}$ (solid lines on the double-logarithmic plot). The Fano factor $F = P/2e\bar{I} = (P/P_0)(G_0/G)$ rapidly approaches 1/3, as shown in the upper panel.

35
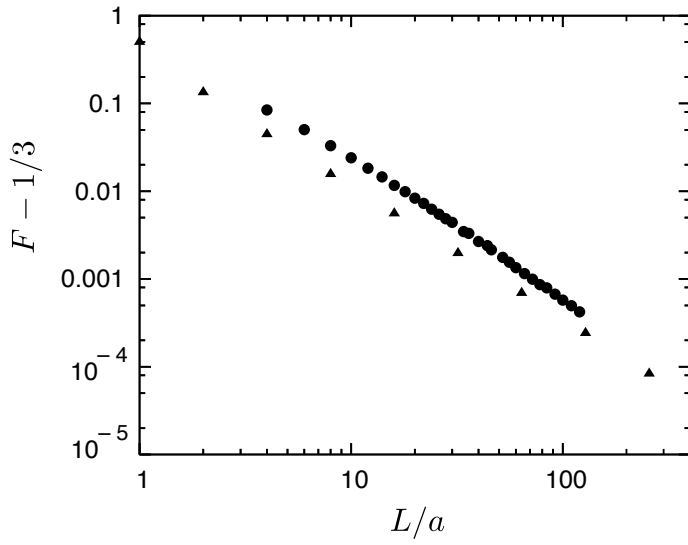
Figure 2.2: The deviation of the Fano factor from 1/3 scales to zero as a power law for the Sierpiński lattice (triangles) and for the random-resistor network (circles).
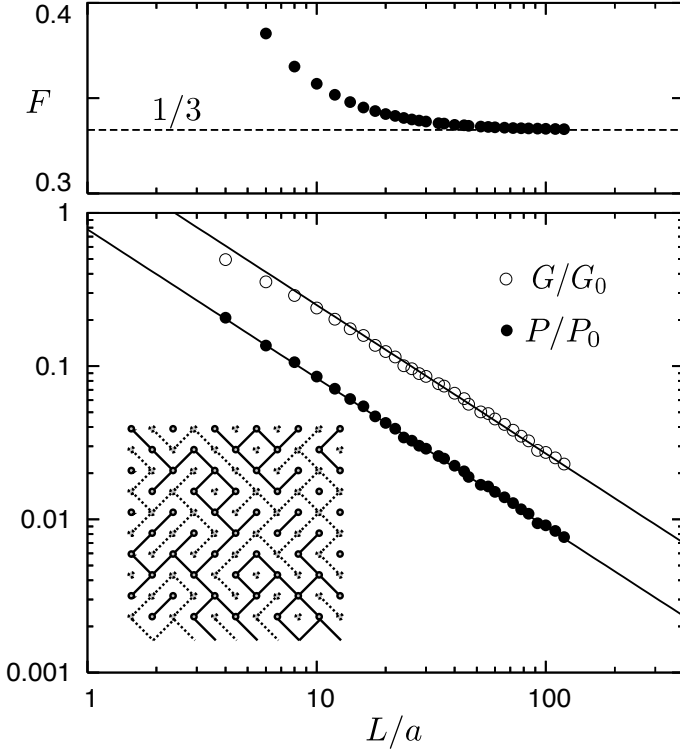
Figure 2.3: Same as Fig. 2.1, but now for the random-resistor network of disordered graphene introduced by Cheianov et al. [35]. The inset shows one realization of the network for $L/a = 10$ (the data points are averaged over $\simeq 10^3$ such realizations). The alternating solid and dashed lattice sites represent, respectively, the electron (n) and hole (p) puddles. Horizontal bonds (not drawn) are p-n junctions, with a negligibly small conductance $G_{pn} \approx 0$. Diagonal bonds (solid and dashed lines) each have the same tunnel conductance G_0. Current flows from the left edge of the square network to the right edge, while the upper and lower edges are connected by periodic boundary conditions. This plot is for undoped graphene, corresponding to an equal fraction of solid (n-n) and dashed (p-p) bonds.

3 Nonalgebraic length dependence of transmission through a chain of barriers with a Lévy spacing distribution

3.1 Introduction

Barthelemy, Bertolotti, and Wiersma have reported on the fabrication of an unusual random optical medium which they have called a *Lévy glass* [15]. It consists of a random packing of glass microspheres having a Lévy distribution of diameters. The space between the spheres is filled with strongly scattering nanoparticles. A photon trajectory therefore consists of ballistic segments of length s through spherical regions, connected by isotropic scattering events. A Lévy distribution is characterized by a slowly decaying tail, $p(s) \propto 1/s^{1+\alpha}$ for $s \to \infty$, with $0 < \alpha < 2$, such that the second moment (and for $\alpha < 1$ also the first moment) diverges. The transmission of light through the Lévy glass was analyzed [15] in terms of a Lévy walk [87, 129, 92] for photons.

Because the randomness in the Lévy glass is frozen in time ("quenched" disorder), correlations exist between subsequent scattering events. Backscattering after a large step is likely to result in another large step. This is different from a Lévy walk, where subsequent steps are independently drawn from the Lévy distribution ("annealed" disorder). Numerical [76] and analytical [120] theories indicate that the difference between quenched and annealed disorder can be captured (at least approximately) by a renormal-

ization of the Lévy walk exponent – from the annealed value α to the quenched value $\alpha' = \alpha + (2/d) \max(0, \alpha - d)$ in d dimensions. Qualitatively speaking, the correlations in a Lévy glass slow down the diffusion relative to what is expected for a Lévy walk, and the effect is the stronger the lower the dimension.

To analyze the effect of such correlations in a quantitative manner, we consider in this paper the one-dimensional analogue of a Lévy glass, which is a linear chain of barriers with independently Lévy distributed spacings s. Such a system might be produced artificially, along the lines of Ref. [15], or it might arise naturally in a porous medium [79] or in a nanowire [72]. Earlier studies of this system[1] [52, 36, 14, 25] have compared the dynamical properties with those of a Lévy walk. In particular, Barkai, Fleurov, and Klafter [14] found a superdiffusive mean-square displacement as a function of time [$\langle x^2(t) \rangle \propto t^\gamma$ with $\gamma > 1$] – reminiscent of a Lévy walk (where $\gamma = 3 - \alpha$). No precise correspondence to a Lévy walk is to be expected in one dimension, because subsequent step lengths are highly correlated: Backscattering after a step of length s to the right results in the same step length s to the left.

The simplicity of one-dimensional dynamics allows for an exact solution of the static transmission statistics, without having to assume a Lévy walk. We present such a calculation here, and find significant differences with the $L^{-\alpha/2}$ scaling of the average transmission expected [40, 78, 28] for a Lévy walk (annealed disorder) through a system of length L. If the length of the system is measured from the first barrier, we find for the case of quenched disorder an average transmission $\langle T \rangle \propto L^{-\alpha} \ln L$ for $0 < \alpha < 1$ and $\langle T \rangle \propto L^{-1}$ for $\alpha > 1$. Note that the nonalgebraic length de-

---

[1]The authors of Ref. [14] calculate a lower bound to the mean square displacement, with the result $\langle x^2 \rangle \geq t^{\min(2, 3 - \alpha)}$ if the initial position of the particle is randomly chosen along the chain (so superdiffusion for any $0 < \alpha < 2$). If the particle starts at a barrier (which corresponds to the situation we consider in the present work), the result is $\langle x^2 \rangle \geq t^{2-\alpha}$ (so superdiffusion for $0 < \alpha < 1$). Earlier papers [52, 36] gave different results for the mean square displacement, but a direct comparison is problematic because those papers did not notice the dependence on the starting position.
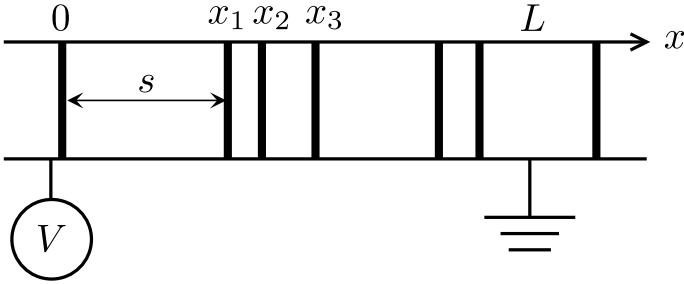
Figure 3.1: Linear chain of randomly spaced tunnel barriers. We study the statistics of conductance (or transmission) over a length L for a Lévy distribution of spacings $p(s)$.

pendence for $0 < \alpha < 1$ goes beyond what can be captured by a renormalization of α.

In the electronic context the average conductance $\langle G \rangle$ is proportional to $\langle T \rangle$, in view of the Landauer formula. In that context it is also of interest to study the shot noise power S, which quantifies the time dependent fluctuations of the current due to the granularity of the electron charge. We calculate the Fano factor $F \propto \langle S \rangle / \langle G \rangle$, and find that F approaches the value $1/3$ characteristic of normal diffusion [18, 96] with increasing L – but with relatively large corrections that decay only as $1/\ln L$ for $0 < \alpha < 1$.

3.2 Formulation of the problem

We consider a linear chain of tunnel barriers, see Fig. 3.1, with a distribution of spacings $p(s)$ that decays for large s as $1/s^{\alpha+1}$. A normalizable distribution requires $\alpha > 0$. For $0 < \alpha < 1$ the mean spacing is infinite. We take for each barrier the same mode-independent transmission probability $\Gamma \ll 1$ (no ballistic transmission). The corresponding tunnel resistance is $r = (h/e^2)(N\Gamma)^{-1}$, with N the number of transverse modes. In the electronic context we require $r \ll h/e^2$, so that the Coulomb blockade of single-electron tunneling can be ignored.

We work in the regime of incoherent sequential tunneling (no resonant tunneling). This regime can be reached for $N \gg 1$ as a result of intermode scattering, or it can be reached even for small N as a result of a short phase coherence length. For sequential tunneling the resistance R of n barriers in series is just the series resistance nr [corresponding to a transmission probability $T = (n\Gamma)^{-1}$]. We measure this resistance

$$R(L) = r \sum_n \theta(x_n)\theta(L - x_n) \tag{3.1}$$

between one contact at $x = 0$ and a second contact at $x = L > 0$. The numbers x_n indicate the coordinates of the tunnel barriers and $\theta(x)$ is the step function [$\theta(x) = 1$ if $x > 0$ and $\theta(x) = 0$ if $x < 0$].

Without further restrictions the statistics of the conductance would be dominated by ballistic realizations, that have not a single tunnel barrier in the interval $(0, L)$. The reason, discussed in Ref. [14], is that the average distance between a randomly chosen point along the chain and the nearest tunnel barrier diverges for any $0 < \alpha < 2$ (so even if the mean spacing between the barriers is finite). To eliminate ballistic transmission, we assume that one tunnel barrier is kept fixed at $x_0 = 0^+$. (This barrier thus contributes r to the resistance.) If we order the coordinates such that $x_n < x_{n+1}$, we have

$$R(L) = r + r \sum_{n=1}^{\infty} \theta(x_n)\theta(L - x_n). \tag{3.2}$$

We seek the scaling with L in the limit $L \to \infty$ of the negative moments $\langle R(L)^p \rangle$ ($p = -1, -2, -3, \ldots$) of the resistance. This information will give us the scaling of the positive moments of the conductance $G = R^{-1}$ and transmission $T = (h/Ne^2)R^{-1}$. It will also give us the average of the shot noise power S, which for an arbitrary number of identical tunnel barriers in series is determined by the formula [61]

$$S = \frac{2}{3}e|V|r^{-1}[(R/r)^{-1} + 2(R/r)^{-3}], \tag{3.3}$$

where V is the applied voltage. From $\langle S \rangle$ and $\langle G \rangle$ we obtain the Fano factor F, defined by

$$F = \frac{\langle S \rangle}{2e|V|\langle G \rangle}. \tag{3.4}$$

3.3 Arbitrary moments

The general expression for moments of the resistance is

$$\langle R(L)^p \rangle = r^p \left\langle \left(1 + \sum_{n=1}^{\infty} \theta(x_n)\theta(L - x_n) \right)^p \right\rangle, \tag{3.5}$$

where the brackets $\langle \cdots \rangle$ indicate the average over the spacings,

$$\langle \cdots \rangle = \prod_{n=1}^{\infty} \int_{-\infty}^{\infty} dx_n \, p(x_n - x_{n-1}) \cdots , \tag{3.6}$$

with the definitions $x_0 = 0$ and $p(s) = 0$ for $s < 0$. We work out the average,

$$\langle R(L)^p \rangle = r^p \sum_{n=1}^{\infty} n^p \left(\prod_{i=1}^{n} \int_{-\infty}^{\infty} ds_i \, p(s_i) \right)$$
$$\times \theta \left(\sum_{i=1}^{n} s_i - L \right) \theta \left(L - \sum_{i=1}^{n-1} s_i \right). \tag{3.7}$$

It is more convenient to evaluate the derivative with respect to L of Eq. (3.7), which takes the form of a multiple convolution of the spacing distribution[2],

$$\frac{d}{dL} \langle R^p \rangle = r^p (2^p - 1) p(L)$$
$$+ r^p \sum_{n=2}^{\infty} [(n+1)^p - n^p] \int_{-\infty}^{\infty} dx_{n-1} \cdots \int_{-\infty}^{\infty} dx_1$$
$$p(L - x_{n-1}) p(x_{n-1} - x_{n-2}) \cdots p(x_2 - x_1) p(x_1). \tag{3.8}$$

---

[2] We cannot directly take the derivative of Eq. (3.5), because that would lead (for $p \neq 1$) to an undefined product of $\theta(L - x)$ and $\delta(L - x)$. No such complication arises if we take the derivative of Eq. (3.7).

In terms of the Fourier (or Laplace) transform

$$f(\xi) = \int_0^\infty ds\, e^{i\xi s} p(s), \tag{3.9}$$

the series (3.8) can be summed up,

$$\frac{d}{dL}\langle R^p \rangle = \frac{r^p}{2\pi} \int_{-\infty+i0^+}^{\infty+i0^+} d\xi\, e^{-i\xi L} \sum_{n=1}^{\infty} [(n+1)^p - n^p] f(\xi)^n$$

$$= \frac{r^p}{2\pi} \int_{-\infty+i0^+}^{\infty+i0^+} d\xi\, e^{-i\xi L} \frac{1 - f(\xi)}{f(\xi)} \, \mathrm{Li}_{-p}[f(\xi)]. \tag{3.10}$$

The function $\mathrm{Li}(x)$ is the polylogarithm. The imaginary infinitesimal $i0^+$ added to ξ regularizes the singularity of the integrand at $\xi = 0$. For negative p this singularity is integrable, and the integral (3.10) may be rewritten as an integral over the positive real axis,

$$\frac{d}{dL}\langle R^p \rangle = \frac{r^p}{\pi} \mathrm{Re} \int_0^\infty d\xi\, e^{-i\xi L} \frac{1 - f(\xi)}{f(\xi)} \, \mathrm{Li}_{-p}[f(\xi)]. \tag{3.11}$$

3.4 Scaling with length

3.4.1 Asymptotic expansions

In the limit $L \to \infty$ the integral over ξ in Eq. (3.11) is governed by the $\xi \to 0$ limit of the Fourier transformed spacing distribution. Because $p(s)$ is normalized to unity one has $f(0) = 1$, while the large-s scaling $p(s) \propto 1/s^{\alpha+1}$ implies

$$\lim_{\xi \to 0} f(\xi) = \begin{cases} 1 + c_\alpha (s_0\xi)^\alpha, & 0 < \alpha < 1, \\ 1 + i\bar{s}\xi + c_\alpha (s_0\xi)^\alpha, & 1 < \alpha < 2. \end{cases} \tag{3.12}$$

The characteristic length $s_0 > 0$, the mean spacing $\bar{s}$, as well as the numerical coefficient c_α are determined by the specific form of the spacing distribution.

The limiting behavior of the polylogarithm is governed by

$$\mathrm{Li}_1(1+\epsilon) = -\ln(-\epsilon), \tag{3.13}$$

$$\lim_{\epsilon \to 0} \mathrm{Li}_2(1+\epsilon) = \zeta(2) - \epsilon \ln(-\epsilon), \tag{3.14}$$

$$\lim_{\epsilon \to 0} \mathrm{Li}_n(1+\epsilon) = \zeta(n) + \zeta(n-1)\epsilon, \quad n = 3, 4, \ldots \tag{3.15}$$

In combination with Eq. (3.12) we find, for $0 < \alpha < 1$, the following expansions of the integrand in Eq. (3.11):

$$\lim_{\zeta \to 0} \frac{1-f}{f} \mathrm{Li}_{-p}(f) = c_\alpha(s_0\zeta)^\alpha \ln[-c_\alpha(s_0\zeta)^\alpha],$$

$$\text{if } p = -1, \tag{3.16}$$

$$\lim_{\zeta \to 0} \frac{1-f}{f} \mathrm{Li}_{-p}(f) = -\zeta(-p)c_\alpha(s_0\zeta)^\alpha,$$

$$p = -2, -3\ldots \tag{3.17}$$

For $1 < \alpha < 2$ we should replace $c_\alpha(s_0\zeta)^\alpha$ by $i\bar{s}\zeta + c_\alpha(s_0\zeta)^\alpha$.

3.4.2 Results

We substitute the expansions (3.16) and (3.17) into Eq. (3.11), and obtain the large-L scaling of the moments of conductance with the help of the following Fourier integrals ($L > 0$, $\alpha > -1$):

$$\int_0^\infty d\zeta\, e^{-i\zeta L} \zeta^\alpha \ln\zeta = i\Gamma(1+\alpha)e^{-i\pi\alpha/2}L^{-1-\alpha}$$

$$\times (\ln L + i\pi/2 + \gamma_E - H_\alpha), \tag{3.18}$$

$$\int_0^\infty d\zeta\, e^{-i\zeta L} \zeta^\alpha = -i\Gamma(1+\alpha)e^{-i\pi\alpha/2}L^{-1-\alpha}, \tag{3.19}$$

$$\mathrm{Re} \int_0^\infty d\zeta\, e^{-i\zeta L} i\zeta = 0, \tag{3.20}$$

$$\mathrm{Re} \int_0^\infty d\zeta\, e^{-i\zeta L} i\zeta \ln\zeta = -\tfrac{1}{2}\pi L^{-2}. \tag{3.21}$$

Here γ_E is Euler's constant and H_α is the harmonic number. The resulting scaling laws are listed in Table 3.1.

Two physical consequences of these scaling laws are:

	$0 < \alpha < 1$	$1 < \alpha < 2$
$\langle R^{-1} \rangle \equiv \langle G \rangle$	$L^{-\alpha} \ln L$	L^{-1}
$\langle R^p \rangle \equiv \langle G^{-p} \rangle,\ p = -2, -3, \ldots$	$L^{-\alpha}$	$L^{-\alpha}$

Table 3.1: Scaling with L of moments of conductance (or, equivalently, transmission).

- The Fano factor (3.4) approaches $1/3$ in the limit $L \to \infty$, regardless of the value of α, but for $0 < \alpha < 1$ the approach is very slow: $F - 1/3 \propto 1/\ln L$. For $1 < \alpha < 2$ the approach is faster but still sublinear, $F - 1/3 \propto 1/L^{\alpha-1}$.

- The root-mean-square fluctuations rms $G = \sqrt{\langle G^2 \rangle - \langle G \rangle^2}$ of the conductance become much larger than the average conductance for large L, scaling as rms $G/\langle G \rangle \propto L^{\alpha/2}/\ln L$ for $0 < \alpha < 1$ and as rms $G/\langle G \rangle \propto L^{1-\alpha/2}$ for $1 < \alpha < 2$.

3.5 Numerical test

To test the scaling derived in the previous sections, in particular to see how rapidly the asymptotic L-dependence is reached with increasing L, we have numerically generated a large number of random chains of tunnel barriers and calculated moments of conductance and the Fano factor from Eqs. (3.2)–(3.4).

For the spacing distribution in this numerical calculation we took the Lévy stable distribution[3] for $\alpha = 1/2$,

$$p_{1/2}(s) = (s_0/2\pi)^{1/2} s^{-3/2} e^{-s_0/2s}. \tag{3.22}$$

Its Fourier transform is

$$f_{1/2}(\xi) = \exp(-\sqrt{-2is_0\xi}) \Rightarrow c_{1/2} = i - 1. \tag{3.23}$$

---

[3]For efficient algorithms to generate random variables with a Lévy stable distribution, see Refs. [33, 88].

Inserting the numerical coefficients, the large-L scaling of conductance moments for the distribution (3.22) is

$$\lim_{L\to\infty} \langle G \rangle = \frac{1}{r}(2\pi L/s_0)^{-1/2}[\ln(2L/s_0) + \gamma_E], \qquad (3.24)$$

$$\lim_{L\to\infty} \langle G^p \rangle = 2\zeta(p)\frac{1}{r^p}(2\pi L/s_0)^{-1/2}, \quad p \geq 2. \qquad (3.25)$$

The resulting scaling of the conductance fluctuations and Fano factor is

$$\left(\frac{\text{rms }G}{\langle G \rangle}\right)^2 \equiv \frac{\langle G^2 \rangle}{\langle G \rangle^2} - 1 \approx \frac{(\pi^2/3)(2\pi L/s_0)^{1/2}}{[\ln(2L/s_0) + \gamma_E]^2} - 1, \qquad (3.26)$$

$$F \approx \frac{1}{3} + \frac{(4/3)\zeta(3)}{\ln(2L/s_0) + \gamma_E}. \qquad (3.27)$$

In Fig. 3.2 we compare these analytical large-L formulas with the numerical data. The average conductance converges quite rapidly to the scaling (3.24), while the convergence for higher moments (which determine the conductance fluctuations and Fano factor) requires somewhat larger systems. We clearly see in Fig. 3.2 the relative growth of the conductance fluctuations with increasing system size and the slow decay of the Fano factor towards the diffusive $1/3$ limit.

3.6 Conclusion and outlook

In conclusion, we have analyzed the statistics of transmission through a sparse chain of tunnel barriers. The average spacing of the barriers diverges for a Lévy spacing distribution $p(s) \propto 1/s^{1+\alpha}$ with $0 < \alpha < 1$. This causes an unusual scaling with system length L (measured from the first tunnel barrier) of the moments of transmission or conductance, as summarized in Table 3.1. A logarithmic correction to the power law scaling appears for the first moment. Higher moments of conductance all scale with the same power law, differing only in the numerical prefactor. As a consequence,

sample-to-sample fluctuations of the transmission become larger than the average with increasing L.

This theoretical study of a one-dimensional "Lévy glass" was motivated by an optical experiment on its three-dimensional analogue [15]. The simplicity of a one-dimensional geometry has allowed us to account exactly for the correlations between subsequent step lengths, which distinguish the random walk through the sparse chain of barriers from a Lévy walk. We surmise that step length correlations will play a role in two and three dimensional sparse arrays as well, complicating a direct application of the theory of Lévy walks to the experiment. This is one line of investigation for the future.

A second line of investigation is the effect of wave interference on the transmission of electrons or photons through a sparse chain of tunnel barriers. Here we have considered the regime of incoherent sequential transmission, appropriate for a multi-mode chain with mode-mixing or for a single-mode chain with a short coherence length. The opposite, phase coherent regime was studied in Ref. [25]. In a single-mode and phase coherent chain interference can lead to localization, producing an exponential decay of transmission. An investigation of localization in this system is of particular interest because the sparse chain belongs to the class of disordered systems with long-range disorder, to which the usual scaling theory of Anderson localization does not apply [115].

A third line of investigation concerns the question "what is the shot noise of anomalous diffusion"? Anomalous diffusion [92] is characterized by a mean square displacement $\langle x^2 \rangle \propto t^\gamma$ with $0 < \gamma < 1$ (subdiffusion) or $\gamma > 1$ (superdiffusion). The shot noise for normal diffusion ($\gamma = 1$) has Fano factor $1/3$ [18, 96], and Ref. [48] concluded that subdiffusion on a fractal also produces $F = 1/3$. Here we found a convergence, albeit a logarithmically slow convergence, to the same $1/3$ Fano factor for a particular system with superdiffusive dynamics. We conjecture that $F = 1/3$ in the entire subballistic regime $0 < \gamma < 2$, with deviations appearing in the ballistic limit $\gamma \to 2$ – but we do not have a general theory to support this conjecture.
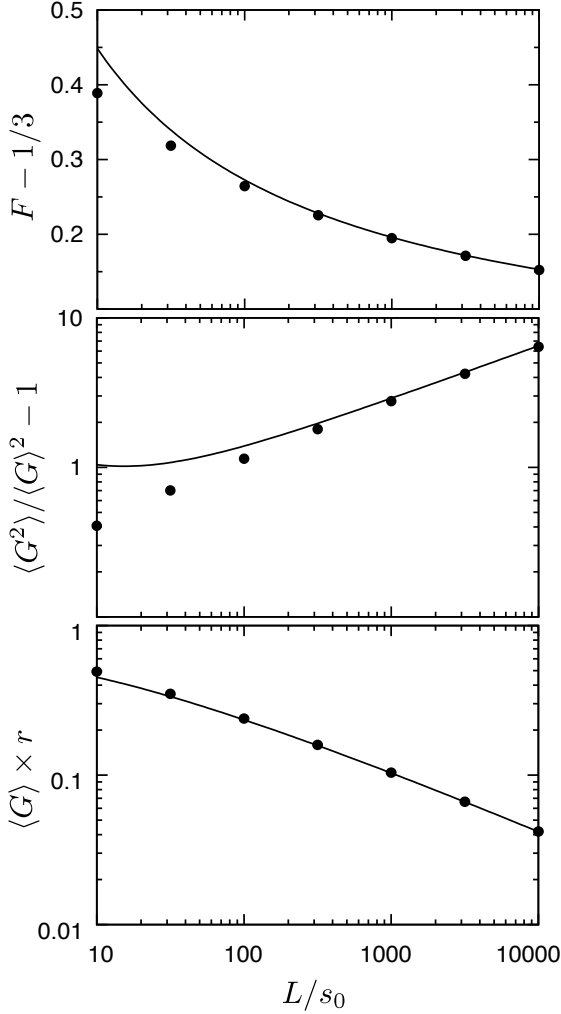
Figure 3.2: Scaling of the average conductance (bottom panel), the variance of the conductance (middle panel), and the Fano factor (top panel), for a chain of tunnel barriers with spacings distributed according to the $\alpha = 1/2$ Lévy stable distribution (3.22). The data points are calculated numerically, by averaging over a large number of random chains of tunnel barriers. The solid curves are the analytical results (3.24)–(3.27) of the asymptotic analysis in the $L \to \infty$ limit.

4 Finite difference method for transport properties of massless Dirac fermions

4.1 Introduction

The discovery of graphene [47] has created a need for efficient numerical methods to calculate transport properties of massless Dirac fermions. The two-dimensional massless Dirac equation (or Weyl equation) that governs the low-energy and long-wave length dynamics of conduction electrons in graphene has a time reversal symmetry called *symplectic* – which is special because it squares to -1. (The usual time reversal symmetry, which squares to $+1$, is called *orthogonal*.) The symplectic symmetry is at the origin of some of the unusual transport properties of graphene [86, 104, 117, 20, 42], including the absence of back scattering [10], weak antilocalization [137], enhanced conductance fluctuations [67, 66], and absence of a metal-insulator transition [13, 99].

Numerical methods of solution can be divided into two classes, depending on whether they break or preserve the symplectic symmetry.

The tight-binding model of graphene, with nearest neighbor hopping on a honeycomb lattice, breaks the symplectic symmetry by the two mechanisms of intervalley scattering [137] and trigonal warping [90]. Intervalley scattering couples the two flavors of Dirac fermions, corresponding to the two different valleys (at opposite corners of the Brillouin zone) in the graphene band structure, thereby changing the symmetry class from symplectic to orthog-

onal. Trigonal warping is a triangular distortion of the conical band structure that breaks the momentum inversion symmetry $(+\boldsymbol{p} \rightarrow -\boldsymbol{p})$, thereby effectively breaking time reversal symmetry in a single valley and changing the symmetry class from symplectic to unitary.

Breaking of the symplectic symmetry eliminates both weak antilocalization as well as the enhancement of the conductance fluctuations, and drives the system to an insulator with increasing size or disorder [6, 8]. As observed in computer simulations [116, 80, 148], the breaking of the symplectic symmetry can be pushed to larger system sizes and larger disorder strengths by reducing the lattice constant (at fixed correlation length and fixed amplitude of the disorder potential) – but this severely limits the computational efficiency.

The Chalker-Coddington network model [32, 54, 75], applied to graphene in Ref. [133], has a single flavor of Dirac fermions, so there is no intervalley scattering – but it still belongs to the same class of methods that break the symplectic symmetry of the massless Dirac equation. (The symplectic symmetry is broken on short length scales by the Aharonov-Bohm phases that appear in the mapping of the Dirac equation onto the network model.)

Both the network model and the tight-binding model are *real space* regularizations of the Dirac equation, with a smallest length scale (the lattice constant) to cut off the unbounded spectrum at large positive and large negative energies. There exists at present just one method to calculate transport properties numerically while preserving the symplectic symmetry, developed independently (and implemented differently) in Refs. [13] and [99]. That method (used also in Refs. [118, 100]) is based on a *momentum space* regularization, with a cutoff of the Fourier transformed Dirac equation at some large value of momentum.

It is the purpose of the present paper to develop and implement an alternative method of solution of the Dirac equation, that shares with the tight-binding and network models the convenience of a formulation in real space rather than momentum space, but without breaking the symplectic symmetry.

52

A celebrated no-go theorem [98] in lattice gauge theory forbids any regularization of the Dirac equation with *local* couplings from preserving symplectic symmetry. (The problematic role of inter-valley scattering appears in that context as the fermion doubling problem.) Several *nonlocal* finite difference methods have been proposed to work around the no-go theorem and we will adapt one of these (developed by Stacey [134] and by Bender, Milton, and Sharp [22]) to the study of transport properties.

The adaptation amounts to 1) the inclusion of a spatially dependent electrostatic potential (which breaks the chiral symmetry that played a central role in Refs. [134, 22]), and 2) a proper discretization of the current operator (such that the total current through any cross section is conserved). We implement the finite difference method to solve the scattering problem of Dirac fermions in a disordered potential landscape connected to ballistic leads, and compare our numerical results for the scaling and statistics of conductance and shot noise power with analytical theories [67, 66, 121].

Our numerical method is relevant for electrical conduction in graphene under the assumption that the impurity potential in the carbon monolayer is long-ranged (so that intervalley scattering is suppressed) and weak (so that trigonal warping can be neglected). Massless Dirac fermions are also expected to govern the electrical conduction along the surface of a three-dimensional topological insulator [45, 94, 114] (realized in BiSb [55]). In that case the symplectic symmetry is preserved even for short-range scatterers, and our numerical results should be applicable more generally.

4.2 Finite difference representation of the transfer matrix

4.2.1 Dirac equation

We consider the two-dimensional massless Dirac equation,

$$H\Psi = E\Psi, \quad H = -i\hbar v(\sigma_x \partial_x + \sigma_y \partial_y) + U(\boldsymbol{r}), \qquad (4.1)$$

where v and E are the velocity and energy of the Dirac fermions, $U(x,y)$ is the electrostatic potential landscape, and $\Psi(x,y)$ is the two-component (spinor) wave function. The two spinor components of Ψ refer to the two atoms in the unit cell in the application to graphene, or to the two spin degrees of freedom in the application to the surface of a topological insulator. We note the symplectic symmetry of the massless Dirac Hamiltonian,

$$H = \mathcal{S}H\mathcal{S}^{-1} = \sigma_y H^* \sigma_y. \tag{4.2}$$

The time reversal symmetry operator $\mathcal{S} = i\sigma_y \mathcal{C}$ (with $\mathcal{C}$ the operator of complex conjugation) squares to -1. The chiral symmetry $\sigma_z H \sigma_z = -H$ is broken by a nonzero U, so it will play no role in what follows. For later use we also note the current operator

$$(j_x, j_y) = v(\sigma_x, \sigma_y). \tag{4.3}$$

We consider a strip geometry of length L along the longitudinal x direction and width W along the transversal y direction. For the discretization we use a square lattice, $x_m = m\Delta$, $y_n = n\Delta$, with indices $m = 1, 2, \ldots M$ ($M = L/\Delta$), $n = 1, 2, \ldots N$ ($N = W/\Delta$). In the applications we will consider large aspect ratios $W/L \gg 1$, for which the precise choice of boundary conditions in the transverse direction does not matter. We choose periodic boundary conditions, $y_{N+1} \equiv y_1$, since they preserve the symplectic symmetry. The values $\Psi_{m,n} = \Psi(x_m, y_n)$ of the wave function at a lattice point are collected into a set of N-component vectors $\Psi_m = (\Psi_{m,1}, \Psi_{m,2}, \ldots \Psi_{m,N})^T$, one for each $m = 1, 2, \ldots M$.

The $N \times N$ transfer matrix $\mathcal{M}_m$ is defined by

$$\Psi_{m+1} = \mathcal{M}_m \Psi_m. \tag{4.4}$$

The symplectic symmetry (4.2) of the Hamiltonian requires that Ψ and $\sigma_y \Psi^*$ are both solutions at the same energy E, so they should both satisfy Eq. (4.4). The corresponding condition on the transfer matrix is

$$\mathcal{M}_m = \sigma_y \mathcal{M}_m^* \sigma_y. \tag{4.5}$$

The transfer matrix should conserve the total current through any cross section of the strip. In terms of the (still to be determined) discretized current operator J_x, this condition reads

$$\langle \Psi_{m+1} | J_x | \Psi_{m+1} \rangle = \langle \Psi_m | J_x | \Psi_m \rangle, \tag{4.6}$$

which then corresponds to the following condition on the transfer matrix:

$$\mathcal{M}_m^\dagger J_x \mathcal{M}_m = J_x. \tag{4.7}$$

Our problem is to discretize the differential operators in the Dirac equation (4.1), as well as the current operator (4.3), in such a way that the resulting transfer matrix describes a single flavor of Dirac fermions and without violating the two conditions (4.5), (4.7) of symplectic symmetry and current conservation.

4.2.2 Discretization

A local replacement of the differential operators ∂_x, ∂_y by finite differences either violates the Hermiticity of H (thus violating conservation of current) or breaks the symplectic symmetry (by the mechanism of fermion doubling). A nonlocal finite difference method that preserves the Hermiticity and symplectic symmetry of H was developed by Stacey [134] and by Bender, Milton, and Sharp [22]. These authors considered the case $U = 0$, when both symplectic and chiral symmetry are present. We extend their method to a spatially dependent U (thereby breaking the chiral symmetry), and obtain the discretized transfer matrix and current operator.

Since the transfer matrix relates $\Psi(x, y)$ at two different values of x, it is convenient to isolate the derivative with respect to x from the Dirac equation (4.1). Multiplication of both sides by $(i/\hbar v)\sigma_x$ gives

$$\partial_x \Psi = (-i\sigma_z \partial_y - i\sigma_x V)\Psi, \tag{4.8}$$

with the definition $V = (U - E)/\hbar v$. We can now make contact with the discretization in Refs. [134, 22] of the Dirac equation in
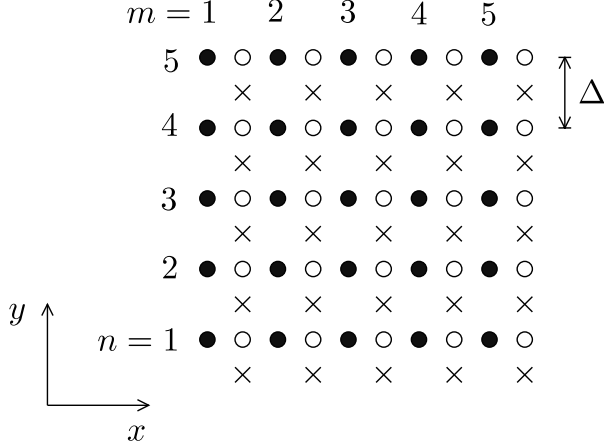
Figure 4.1: Square lattice (filled circles) on which the wave function Ψ is discretized as $\Psi_{m,n}$. The finite differences are evaluated at the displaced points indicated by crosses. The Dirac equation (4.8) is applied at the empty circles, by taking the mean of the contributions from the two adjacent crosses. The resulting finite difference equation defines a transfer matrix in the x direction that conserves current and preserves the symplectic symmetry.

one space and one time dimension, with x playing the role of (imaginary) time and y being the spatial dimension.

The key step by which Refs. [134, 22] avoid fermion doubling is the evaluation of the finite differences on a lattice that is displaced symmetrically from the original lattice. The displaced lattice points $(x_m + \Delta/2, y_n + \Delta/2)$ are indicated by crosses in Fig. 4.1. On the displaced lattice, the differential operators are discretized by

$$\partial_x \Psi \to \frac{1}{2\Delta}(\Psi_{m+1,n} + \Psi_{m+1,n+1} - \Psi_{m,n} - \Psi_{m,n+1}), \qquad (4.9)$$

$$\partial_y \Psi \to \frac{1}{2\Delta}(\Psi_{m,n+1} + \Psi_{m+1,n+1} - \Psi_{m,n} - \Psi_{m+1,n}), \qquad (4.10)$$

and the potential term is replaced by

$$V\Psi \to \tfrac{1}{4}V_{m,n}(\Psi_{m+1,n} + \Psi_{m+1,n+1} + \Psi_{m,n} + \Psi_{m,n+1}), \qquad (4.11)$$

with $V_{m,n} = V(x_m + \Delta/2, y_n + \Delta/2)$. The Dirac equation (4.8) is applied at the points $(x_m + \Delta/2, y_n)$ (empty circles in Fig. 4.1) by averaging the terms at the two adjacent points $(x_m + \Delta/2, y_n \pm \Delta/2)$.

The resulting finite difference equation can be written in a compact form with the help of the $N \times N$ tridiagonal matrices $\mathcal{J}$, $\mathcal{K}$, $\mathcal{V}^{(m)}$, defined by the following nonzero elements:

$$\mathcal{J}_{n,n} = 1, \quad \mathcal{J}_{n,n+1} = \mathcal{J}_{n,n-1} = \tfrac{1}{2}, \qquad (4.12)$$

$$\mathcal{K}_{n,n+1} = \tfrac{1}{2}, \quad \mathcal{K}_{n,n-1} = -\tfrac{1}{2}, \qquad (4.13)$$

$$\mathcal{V}^{(m)}_{n,n} = \tfrac{1}{2}(V_{m,n} + V_{m,n-1}), \quad \mathcal{V}^{(m)}_{n,n+1} = \tfrac{1}{2}V_{m,n},$$

$$\mathcal{V}^{(m)}_{n,n-1} = \tfrac{1}{2}V_{m,n-1}. \qquad (4.14)$$

In accordance with the periodic boundary conditions, the indices $n \pm 1$ should be evaluated modulo N. Notice that $\mathcal{J}$ and $\mathcal{V}^{(m)}$ are real symmetric matrices, while $\mathcal{K}$ is real antisymmetric. Furthermore $\mathcal{J}$ and $\mathcal{K}$ commute, but neither matrix commutes with $\mathcal{V}^{(m)}$.

For later use, we note that $\mathcal{J}$ has eigenvalues

$$j_l = 2\cos^2(\pi l/N), \quad l = 1, 2, \dots N, \qquad (4.15)$$

corresponding to the eigenvectors $\psi^{(l)}$ with elements

$$\psi^{(l)}_n = N^{-1/2}\exp(2\pi i l n/N). \qquad (4.16)$$

The eigenvalues of $\mathcal{K}$ are

$$\kappa_l = i\sin(2\pi l/N), \quad l = 1, 2, \dots N, \qquad (4.17)$$

for the same eigenvectors $\psi^{(l)}$. From Eq. (4.15) we see that for N even there is a zero eigenvalue of $\mathcal{J}$ (at $l = N/2$). To avoid the complications from a noninvertible $\mathcal{J}$, we restrict ourselves to N odd (when all eigenvalues of $\mathcal{J}$ are nonzero).

4.2.3 Transfer matrix

The discretized Dirac equation is expressed in terms of the matrices (4.12)–(4.14) by

$$\frac{1}{2\Delta} \mathcal{J} (\boldsymbol{\Psi}_{m+1} - \boldsymbol{\Psi}_m) = \left(-\frac{i}{2\Delta} \sigma_z \mathcal{K} - \frac{i}{4} \sigma_x \mathcal{V}^{(m)} \right)$$
$$(\boldsymbol{\Psi}_m + \boldsymbol{\Psi}_{m+1}). \tag{4.18}$$

Rearranging Eq. (4.18) we arrive at Eq. (4.4) with the transfer matrix

$$\mathcal{M}_m = \left(\mathcal{J} + i\sigma_z \mathcal{K} + \tfrac{1}{2} i\Delta \sigma_x \mathcal{V}^{(m)} \right)^{-1}$$
$$\left(\mathcal{J} - i\sigma_z \mathcal{K} - \tfrac{1}{2} i\Delta \sigma_x \mathcal{V}^{(m)} \right). \tag{4.19}$$

Since we take N odd, so that $\mathcal{J}$ is invertible, we may equivalently write Eq. (4.19) in the more compact form

$$\mathcal{M}_m = \frac{1 - iX_m}{1 + iX_m}, \quad X_m = \mathcal{J}^{-1} (\sigma_z \mathcal{K} + \tfrac{1}{2} \Delta \sigma_x \mathcal{V}^{(m)}). \tag{4.20}$$

As announced, the transfer matrix is nonlocal (in the sense that multiplication of $\boldsymbol{\Psi}_m$ by $\mathcal{M}_m$ couples all transverse coordinates).

One can readily check that the condition (4.5) of symplectic symmetry is fullfilled. In App. 4.A we demonstrate that the condition (4.7) of current conservation holds if we define the discretized current operator J_x in terms of the symmetric matrix $\mathcal{J}$,

$$J_x = \tfrac{1}{2} v \sigma_x \mathcal{J}. \tag{4.21}$$

The absence of fermion doubling is checked in Sec. 4.4.1.

The transfer matrix $\mathcal{M}$ through the entire strip (from $x = 0$ to $x = L$) is the product of the one-step transfer matrices $\mathcal{M}_m$,

$$\mathcal{M} = \prod_{m=1}^{M} \mathcal{M}_m, \tag{4.22}$$

ordered such that $\mathcal{M}_{m+1}$ is to the left of $\mathcal{M}_m$. The properties of symplectic symmetry and current conservation are preserved upon matrix multiplication.

4.2.4 Numerical stability

The repeated multiplication (4.22) of the one-step transfer matrix to arrive at the transfer matrix of the entire strip is unstable because it produces both exponentially growing and exponentially decaying eigenvalues, and the limited numerical accuracy prevents one from retaining both sets of eigenvalues. We resolve this obstacle, following Refs. [13, 133, 138], by converting the transfer matrix into a unitary matrix, which has only eigenvalues of unit absolute value. The formulas that accomplish this transformation are given in App. 4.B.

4.3 From transfer matrix to scattering matrix and conductance

4.3.1 General formulation

The scattering matrix is obtained from the transfer matrix by connecting the two ends of the strip at $x = 0$ and $x = L$ to semi-infinite ballistic leads. The N transverse modes in the leads (calculated in Sec. 4.4), consist of N_0 propagating modes $\phi_l^{\pm}$ (labeled $+$ for right-moving and $-$ for left-moving), and $N - N_0$ evanescent modes $\chi_l^{\pm}$ (decaying for $x \to \pm\infty$). The propagating modes are normalized such that each carries unit current.

Consider an incoming wave in mode l_0 from the left. At $x = 0$, the sum of incoming, reflected, and evanescent waves is given by

$$\Phi_{l_0}^{\text{left}} = \phi_{l_0}^+ + \sum_l r_{l,l_0}\phi_l^- + \sum_l \alpha_{l,l_0}\chi_l^-, \qquad (4.23)$$

while the sum of transmitted and evanescent waves at $x = L$ is given by

$$\Phi_{l_0}^{\text{right}} = \sum_l t_{l,l_0}\phi_l^+ + \sum_l \alpha'_{l,l_0}\chi_l^+. \qquad (4.24)$$

The $N_0 \times N_0$ reflection matrix r and transmission matrix t are

obtained by equating

$$\Phi_{l_0}^{\text{right}} = \mathcal{M}\Phi_{l_0}^{\text{left}}, \tag{4.25}$$

eliminating the coefficients α, α', and repeating for each of the N_0 propagating modes incident from the left. Starting from a mode incident from the right, we similarly obtain the reflection matrices r' and t', which together with r and t form a $2N_0 \times 2N_0$ unitary scattering matrix,

$$S = \begin{pmatrix} r & t' \\ t & r' \end{pmatrix}. \tag{4.26}$$

As a consequence of unitarity, the matrix products $tt^\dagger$ and $t't'^\dagger$ have the same set of eigenvalues $T_1, T_2, \ldots T_{N_0}$, called transmission eigenvalues.

The number N_0 of propagating modes in the leads is an odd integer, because of our choice of periodic boundary conditions. The symplectic symmetry condition (4.5) then implies that the transmission eigenvalues T_n consist of one unit eigenvalue and $(N_0 - 1)/2$ degenerate pairs (Kramers degeneracy[1]).

The conductance G follows from the transmission eigenvalues via the Landauer formula,

$$G = G_0 \sum_n T_n. \tag{4.27}$$

The conductance quantum $G_0 = 4e^2/h$ in the application to graphene (which has both spin and valley degeneracies), while $G_0 = e^2/h$ in the application to the surface of a topological insulator. The Kramers degeneracy, which is present in both applications, is accounted for in the sum over the transmission eigenvalues.

---

[1]Symplectic symmetry also implies that the basis of modes in the leads can be chosen such that S is antisymmetric ($S = -S^T$). We use a different basis, so our S will be not be antisymmetric. For a direct proof of the Kramers degeneracy of the transmission eigenvalues from the antisymmetry of the scattering matrix, see J. H. Bardarson, J. Phys. A **41**, 405203 (2008).

4.3.2 Infinite wave vector limit

Following Ref. [141], we model metal contacts by leads with an infinitely large Fermi wave vector. In the infinite wave vector limit all modes in the leads are propagating, so $N_0 = N$ and the scattering matrix has dimension $2N \times 2N$. The states $\phi_l^\pm$ ($l = 1, 2, \dots N$) in this limit are simply the $2N$ eigenstates of the current operator J_x, normalized such that each carries the same current. In terms of the eigenvalues and eigenvectors (4.15), (4.16) of $\mathcal{J}$ we have

$$\phi_l^\pm = j_l^{-1/2} \begin{pmatrix} 1 \\ \pm 1 \end{pmatrix} \psi^{(l)}. \tag{4.28}$$

Instead of the general Eqs. (4.23) and (4.24) we now have the simpler equations

$$\Phi_{l_0}^{\text{left}} = \phi_{l_0}^+ + \sum_l r_{l,l_0} \phi_l^-, \quad \Phi_{l_0}^{\text{right}} = \sum_l t_{l,l_0} \phi_l^+. \tag{4.29}$$

To obtain from Eq. (4.25) a closed-form expression for S in terms of $\mathcal{M}$, we first perform the similarity transformation

$$\tilde{\mathcal{M}} = \mathcal{R} \mathcal{M} \mathcal{R}^{-1}, \quad \mathcal{R} = \sigma_H \mathcal{J}^{1/2}, \tag{4.30}$$

where σ_H is the Hadamard matrix,

$$\sigma_H = 2^{-1/2} \begin{pmatrix} 1 & 1 \\ 1 & -1 \end{pmatrix} = \sigma_H^{-1}. \tag{4.31}$$

The notation $\sigma_H \mathcal{J}^{1/2}$ signifies a direct product, where σ_H acts on the spinor degrees of freedom $s = \pm$ and $\mathcal{J}^{1/2}$ acts on the lattice degrees of freedom $n = 1, 2, \dots N$. Notice that the matrix $\mathcal{R}$ is Hermitian [since $\mathcal{J}$ is Hermitian with exclusively positive eigenvalues, see Eq. (4.15)].

We separate the spinor degrees of freedom of $\mathcal{M}$ into four $N \times N$ blocks,

$$\mathcal{M} = \begin{pmatrix} \mathcal{M}^{++} & \mathcal{M}^{+-} \\ \mathcal{M}^{-+} & \mathcal{M}^{--} \end{pmatrix}, \tag{4.32}$$

such that $\mathcal{M}_{ns,ms'} = \mathcal{M}_{nm}^{ss'}$. The matrix $\tilde{\mathcal{M}}$ has a corresponding decomposition into submatrices $\tilde{\mathcal{M}}^{ss'}$. As one can verify by substitution into Eq. (4.29) and comparison with Eq. (4.25), the submatrices $\tilde{\mathcal{M}}^{ss'}$ are related to the transmission and reflection matrices by

$$r = -(\tilde{\mathcal{M}}^{--})^{-1}\tilde{\mathcal{M}}^{-+}, \tag{4.33a}$$

$$t = \tilde{\mathcal{M}}^{++} - \tilde{\mathcal{M}}^{+-}(\tilde{\mathcal{M}}^{--})^{-1}\tilde{\mathcal{M}}^{-+}, \tag{4.33b}$$

$$t' = (\tilde{\mathcal{M}}^{--})^{-1}, \tag{4.33c}$$

$$r' = \tilde{\mathcal{M}}^{+-}(\tilde{\mathcal{M}}^{--})^{-1}. \tag{4.33d}$$

Similar formulas were derived in Ref. [133], but there the transformation from $\mathcal{M}$ to S involved only a Hadamard matrix and no matrix $\mathcal{J}$, because of the different current operator in that model.

4.4 Ballistic transport

For a constant U we have ballistic transport through the strip of length L and width W. In this section we check that we recover the known results [63, 141] for ballistic transport of Dirac fermions from the discretized transfer matrix.

4.4.1 Dispersion relation

For $U = U_0 = $ constant the matrix (4.14) of discretized potentials is given by $\mathcal{V}^{(m)} = -(\varepsilon/\Delta)\mathcal{J}$, with $\varepsilon = (E - U_0)\Delta/\hbar v$ the dimensionless energy (measured relative to the Dirac point at energy U_0). Substitution into Eq. (4.20) gives the m-independent ballistic transfer matrix $\mathcal{M}_{\text{ball}}$,

$$\mathcal{M}_{\text{ball}} = \frac{1 + i(\varepsilon/2)\sigma_x - i\mathcal{J}^{-1}\mathcal{K}\sigma_z}{1 - i(\varepsilon/2)\sigma_x + i\mathcal{J}^{-1}\mathcal{K}\sigma_z}. \tag{4.34}$$

This is the one-step transfer matrix. The transfer matrix through the entire strip, in this ballistic case, is simply $\mathcal{M} = (\mathcal{M}_{\text{ball}})^M$.

In accordance with Eqs. (4.15)–(4.17), the matrix $\mathcal{J}^{-1}\mathcal{K}$ can be diagonalized (for N odd) by

$$\mathcal{J}^{-1}\mathcal{K} = \mathcal{F}\Lambda\mathcal{F}^\dagger, \quad \Lambda_{nn'} = i\tan(\pi n/N)\delta_{nn'}, \tag{4.35a}$$

$$\mathcal{F}_{nn'} = N^{-1/2}\exp(2\pi inn'/N). \tag{4.35b}$$

The Fourier transformed transfer matrix $\mathcal{F}\mathcal{M}_{\text{ball}}\mathcal{F}^\dagger$ is diagonal in the mode index $l = 1, 2, \ldots N$. A 2×2 matrix structure m_l in the spin index remains, given by

$$m_l = \frac{1 + i(\varepsilon/2)\sigma_x + \tan(\pi l/N)\sigma_z}{1 - i(\varepsilon/2)\sigma_x - \tan(\pi l/N)\sigma_z}. \tag{4.36}$$

The eigenvalues and eigenvectors of m_l are

$$m_l u_l^\pm = e^{\pm ik}u_l^\pm, \quad u_l^\pm = \begin{pmatrix} \varepsilon/2 \\ i\tan(\pi l/N) \pm \tan(k/2) \end{pmatrix}, \tag{4.37}$$

with the dimensionless momentum k given as a function of ε and l by the dispersion relation

$$\tan^2(k/2) + \tan^2(\pi l/N) = (\varepsilon/2)^2. \tag{4.38}$$

In Fig. 4.2 we have plotted the dispersion relation (4.38) for two different modes in the first Brillouin zone $-\pi < k < \pi$. For each mode index l, there is one wave that propagates to positive x (on the branch with $d\varepsilon/dk > 0$) and one wave that propagates to negative x (on the branch with $d\varepsilon/dk < 0$).

As anticipated [134, 22], the discretization of the Dirac equation on the displaced lattice (crosses in Fig. 4.1) has avoided the spurious doubling of the fermion degrees of freedom that would have happened if the finite differences would have been calculated on the original lattice (solid dots in Fig. 4.1). In the low-energy and long-wave-length limit $k, \varepsilon \to 0$, the conical dispersion relation $(vp_x)^2 + (vp_y)^2 = (E - U_0)^2$ of the Dirac equation (4.1) is recovered. The longitudinal momentum is $p_x = \hbar k/\Delta$, while the transverse momentum is $p_y = (2\pi\hbar/W)l$ if $l/N \to 0$ or $p_y = -(2\pi\hbar/W)(N - l)$ if $l/N \to 1$.
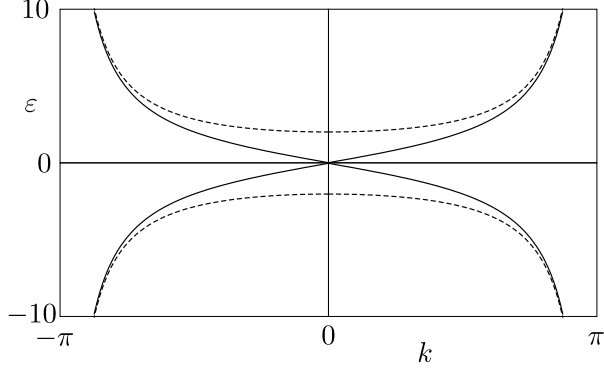
Figure 4.2: Dispersion relation (4.38) of the discretized Dirac equation, plotted in the first Brillouin zone for two transverse modes ($l = N$, solid curve; $l \approx N/4$, dotted curve). The dispersion relation approaches that of the Dirac equation near the point $(k, \varepsilon) = (0, 0)$, and avoids fermion doubling at other points in the Brillouin zone.

4.4.2 Evanescent modes

For $|\varepsilon| < 2 \tan(\pi/N)$, hence for $|E - U_0| \lesssim 2\pi\hbar v/W$, only the mode with index $l = N$ is propagating. The other $N - 1$ modes are evanescent, that is to say, their wave number k has a nonzero imaginary part κ. There are two classes of evanescent modes, one class with a purely imaginary wave number $k = i\kappa_+$, and another class with a complex wave number $k = \pi + i\kappa_-$. The relation between $\kappa_\pm$ and ε, following from Eq. (4.38), is

$$\tanh^2\left(\kappa_+/2\right) = \tan^2(\pi l/N) - (\varepsilon/2)^2, \qquad (4.39a)$$

$$\cotanh^2\left(\kappa_-/2\right) = \tan^2(\pi l/N) - (\varepsilon/2)^2. \qquad (4.39b)$$

In Fig. 4.3 we have plotted Eq. (4.39) for different mode indices, parameterized by $\xi = \tan(\pi l/N)$. The evanescent modes in the Dirac equation correspond to $k = i\kappa_+$ in the limit $\varepsilon \to 0$ (solid contours in Fig. 4.3). The second "spurious" class of evanescent modes, with $k = \pi + i\kappa_-$ (dashed contours), is an artefact of the
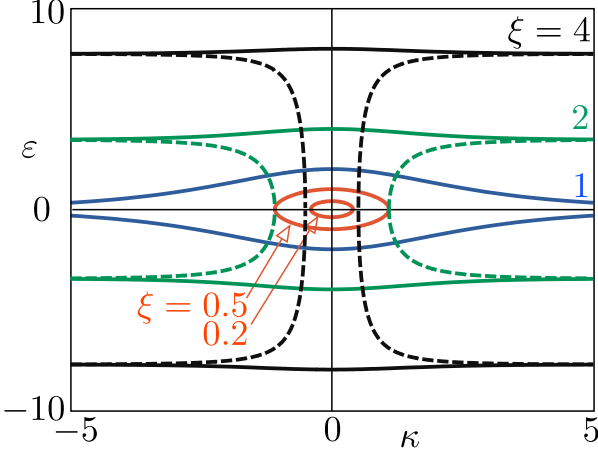
Figure 4.3: Relation between the energy ε and the imaginary part κ of the wave number of evanescent modes, calculated from Eq. (4.39) for five different values of the mode index [parameterized by $\xi = \tan(\pi l/N)$]. The real part of the wave number equals 0 on the solid contours (corresponding to κ_+), while it equals π on the dashed contours (corresponding to κ_-). Only the κ_+ evanescent modes have a correspondence to the Dirac equation in the limit $\varepsilon \to 0$. The κ_- evanescent modes that appear for $|\xi| > 1$ are artefacts of the discretization for large transverse momenta.

discretization that appears for large transverse momenta ($|\xi| > 1$, or $N/4 < l < 3N/4$).

To minimize the effect of the spurious evanescent modes we insert a pair of filters of length L_0 between the strip of length L and the leads with infinitely large Fermi wave vector. By choosing a large but finite Fermi wave vector in the filters, they remove the spurious evanescent modes of large transverse momenta which are excited by the infinite Fermi wave vector in the leads.

The geometry is sketched in Fig. 4.4. In the filters we choose $U = 0$, $E = 2\hbar v/\Delta$ (so $\varepsilon = 2$ in the filters). Since $|\kappa_-| \geq \pi/N$ for
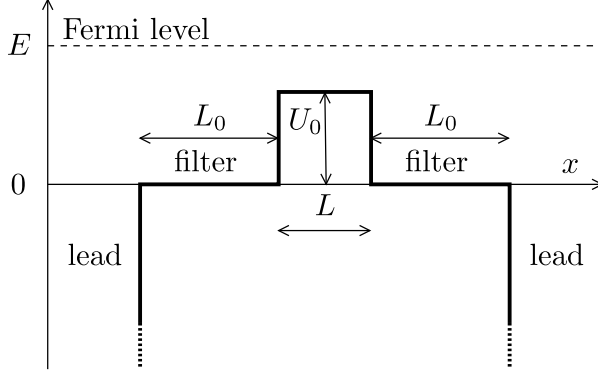
Figure 4.4: Potential profile of a strip (length L), connected to leads by a pair of filters (length L_0). The Fermi wave vector in the leads is taken infinitely large; the finite Fermi wave vector in the filters removes the spurious evanescent modes excited by the leads.

the spurious evanescent modes [described by Eq. (4.39b)], their longest decay length is of order $N\Delta = W$. By choosing $L_0 = 10\,W$ we ensure that these modes are filtered out.

4.4.3 Conductance

We have calculated the conductance at fixed Fermi energy $E = 2\hbar v/\Delta$ as a function of the potential step height U_0. Results are shown in Fig. 4.6 for aspect ratio $W/L = 3$ and lattice constant $\Delta = 10^{-2}\,L$ (solid curve) and compared with the solution of the Dirac equation (dashed curve). The agreement is excellent (for a twice smaller Δ the two curves would have been indistinguishable).

The horizontal dotted line in Fig. 4.6 indicates the value [63, 141]

$$\lim_{W/L \to \infty} \lim_{U_0 \to E} (L/W)G/G_0 = 1/\pi \qquad (4.40)$$

of the minimal conductivity at the Dirac point for a large aspect ratio of the strip. The oscillations which develop as one moves away
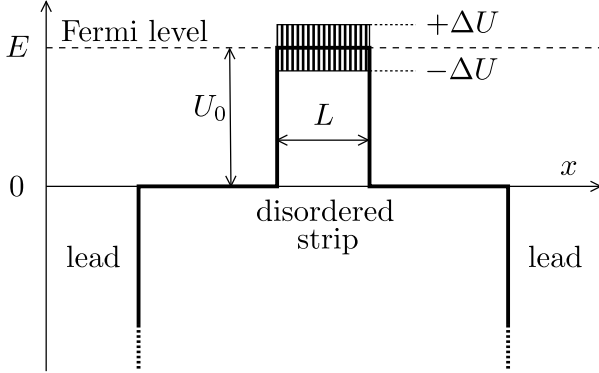
Figure 4.5: Same as Fig. 4.4, but now for the case that the potential in the strip fluctuates around the Dirac point: $U = U_0 + \delta U$, with $U_0 = E$ and δU uniformly distributed in the interval $(-\Delta U, \Delta U)$.

from the Dirac point are Fabry-Perot resonances from multiple reflections at $x = 0$ and $x = L$. The filters of length L_0 are not present in the continuum calculation (dashed curve), but the close agreement with the lattice calculation (solid curve) shows that the filters do not modify these resonances in any noticeable way. The filters do play an essential role in ensuring that the minimal conductivity reaches its proper value (4.40): Without the filters the lattice calculation would give a twice larger minimal conductivity, due to the contribution from the spurious evanescent modes of large transverse momentum.

4.5 Transport through disorder

We introduce disorder in the strip of length L by adding a random potential δU to each lattice point, distributed uniformly in the interval $(-\Delta U, \Delta U)$. Since our discretization scheme conserves the symplectic symmetry exactly, there is no need now to choose a finite correlation length for the potential fluctuations (as in earlier
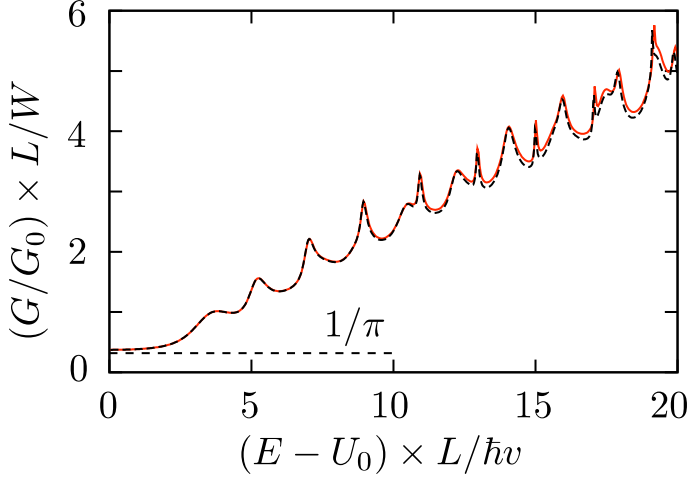
Figure 4.6: Solid curve: conductance in the geometry of Fig. 4.4. The Fermi wave vector $(E - U_0)/\hbar v$ in the strip of length L and width $W = 3L$ is varied by varying the potential step height U_0 at fixed Fermi energy $E = 2\hbar v/\Delta$. The lattice constant $\Delta = 10^{-2} L$. Dashed curve: the result from the Dirac equation (calculated from the formulas in Ref. [141]), corresponding to the limit $\Delta \to 0$. The horizontal dotted line is the mimimal conductivity at the Dirac point.

numerical studies [13, 99, 116, 80, 148, 133, 118, 100]). Instead we can let the potential of each lattice point fluctuate independently, as in the original Anderson model of localization [9].

4.5.1 Scaling of conductance at the Dirac point

When $U_0 = E$ the potential $U_0 + \delta U$ in the strip fluctuates around the Dirac point (see Fig. 4.5). Results for the scaling of the average conductivity $\sigma \equiv (L/W)\langle G \rangle$ with system size are shown for different disorder strengths in Fig. 4.7. We averaged over 3000 disorder realizations for $L/\Delta = 17, 41, 99$ and over 300 realizations
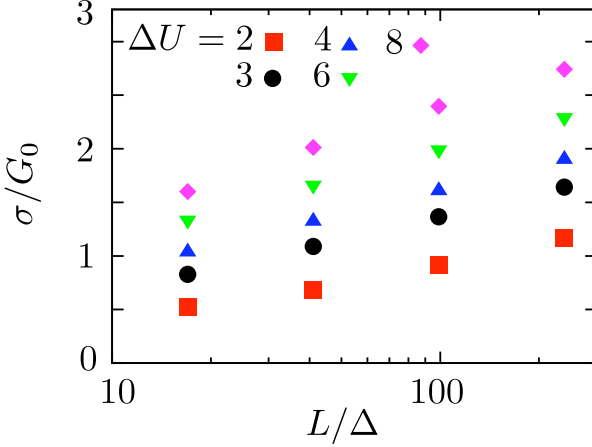
Figure 4.7: Scaling with system size of the average conductivity $\sigma \equiv (L/W)\langle G \rangle$ in a disordered strip at the Dirac point (geometry of Fig. 4.5). The length L of the strip is varied at fixed aspect ratio $W/L = 3$. The data are collected for different disorder strengths ΔU (listed in units of $\hbar v/\Delta$).

for $L/\Delta = 239$. The aspect ratio was fixed at $W/L = 3$.

For sufficiently strong disorder strengths $\Delta U \gtrsim 3\hbar v/\Delta$ the data follow the logarithmic scaling [13, 99]

$$\sigma/G_0 = c \ln[L/l^*(\Delta U)]. \qquad (4.41)$$

There is a consensus in the literature that $c = 1/\pi$ can be calculated perturbatively [121] as a weak antilocalization correction. The quantity l^* plays the role of a mean free path, dependent on the disorder strength. We fit this scaling to our data with a common fitting parameter c (disregarding the data sets with low ΔU as being too close to the ballistic limit). The fitting gives l^* for every data set with the same ΔU.

The resulting single-parameter scaling is presented in Fig. 4.8 (including also the low ΔU sets, for completeness). The data sets collapse onto a single logarithmically increasing conductivity with
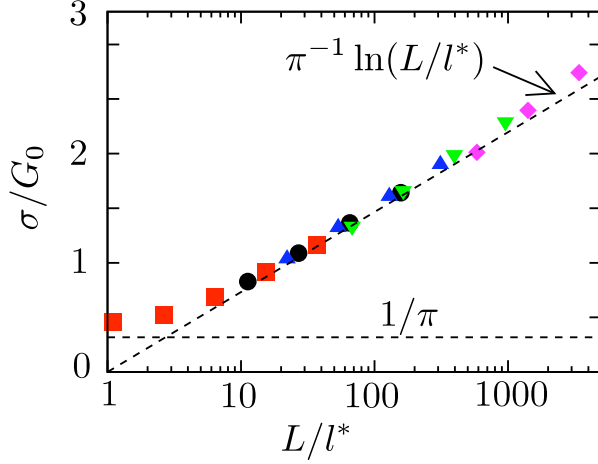
Figure 4.8: Dependence of the conductivity of Fig. 4.7 on the rescaled system length $L/l^*(\Delta U)$. The two dotted lines are the analytical weak and strong disorder limits.

$c \approx 0.33(1)$, close to the expected value $c = 1/\pi \approx 0.318$. To assess the importance of finite-size corrections [131] we include a non-universal lattice-constant dependent term to the logarithmic scaling: $\sigma/G_0 = c \ln[L/l^*(\Delta U)] + f(\Delta U)\Delta/L$. We then find $c \approx 0.316(5)$, again close to the expected value [121]. These results for the absence of localization of Dirac fermions are consistent with earlier numerical calculations [13, 99] using a momentum space regularization of the Dirac equation.

4.5.2 Conductance fluctuations at the Dirac point

The sample-to-sample conductance fluctuations at the Dirac point were calculated numerically in Ref. [116] using the tight-binding model on a honeycomb lattice. An enhancement of the variance above the value for point scatterers was observed, and explained in Ref. [67] in terms of the absence of intervalley scattering. A
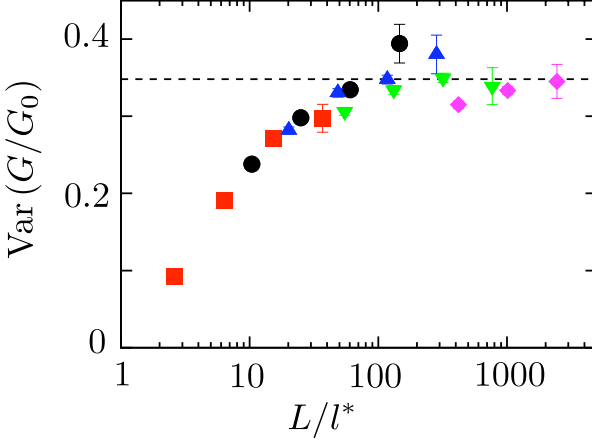
Figure 4.9: Same as Fig. 4.8, but now for the variance of the con-
ductance (instead of the ensemble average). The hor-
izontal dotted line is the analytical prediction (4.42),
$\text{Var}\,(G/G_0) = 0.116\,W/L$ with $W/L = 3$.

perturbative calculation [67, 66] of $\text{Var}\,G = \langle G^2 \rangle - \langle G \rangle^2$ gives

$$\text{Var}\,G = \frac{3\zeta(3)}{\pi^3}\,\frac{W}{L}\,G_0^2, \quad W/L \gg 1. \tag{4.42}$$

Intervalley scattering would reduce the variance by a factor of four,
while trigonal warping without intervalley scattering would reduce
the variance by a factor of two.

In Fig. 4.9 we plot our results for the dependence of the variance
of the conductance on the rescaled system size L/l^*, with the ΔU
dependence of l^* obtained from the scaling analysis of the average
conductance in Sec. 4.5.1. The convergence towards the expected
value (4.42) is apparent. The numerical data of Fig. 4.9 supports the
conclusion of Ref. [121], that the statistics of the conductance at the
Dirac point can be obtained from metallic diffusive perturbation
theory in the large-L limit.

The tight-binding model calculation of Ref. [116] only reached
about half the expected value (4.42), presumably because the po-
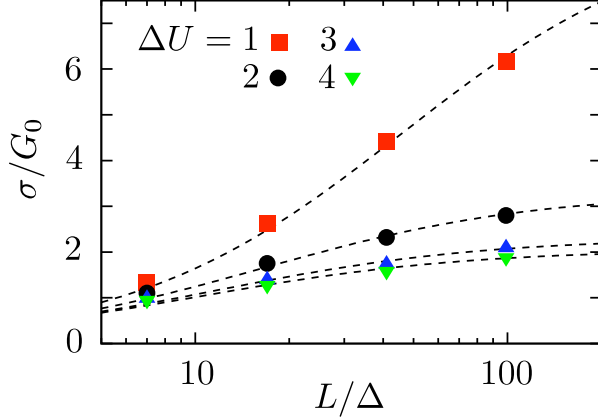
Figure 4.10: Crossover from ballistic to diffusive conduction away from the Dirac point. The conductivity is plotted versus system size, at fixed Fermi wave vector $(E - U_0)/\hbar v = 0.8\,\Delta^{-1}$ in the strip and fixed aspect ratio $W/L = 3$. The data is for different disorder strengths ΔU, listed in units of $\hbar v/\Delta$. The dotted curves are a fit to the semiclassical formula (4.43), with the transport mean free path l_0 as a fit parameter.

tential was not quite smooth enough to avoid intervalley scattering. This illustrates the power of the finite difference method used here: We retain single-valley physics even when the correlation length of the potential is equal to the lattice constant.

4.5.3 Transport away from the Dirac point

The results of Secs. 4.5.1 and 4.5.2 are for potential fluctuations around the Dirac point ($U_0 = E$). In this subsection we consider the average conductance and the conductance fluctuations away from the Dirac point. We take $(E - U_0) = 0.8\,\hbar v/\Delta$ and vary the sample length L at fixed aspect ratio $W/L = 3$. The resulting size dependence of the conductivity is presented in Fig. 4.10, for different disorder strengths ΔU.
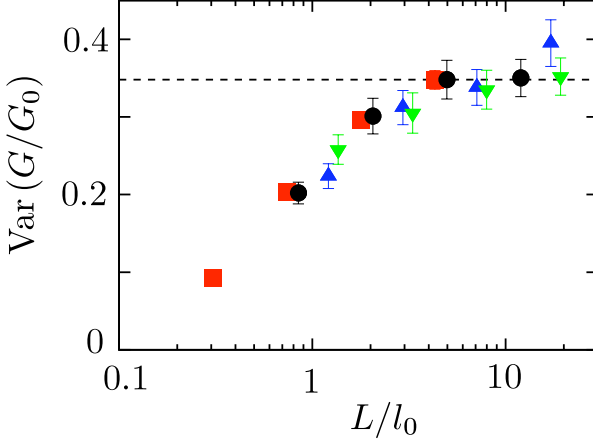
Figure 4.11: Same as Fig. 4.10, but now for the variance of the conductance. The data is plotted as a function of the rescaled sample size, using the values of the mean free path obtained from the fit of the conductance. The horizontal dotted line is the analytical prediction (4.42).

Since antilocalization is a relatively small quantum correction at these high Fermi energies, we are in the regime described by the semiclassical Boltzmann equation [3, 4]. In App. 4.C we apply a general theory [106] for the crossover from ballistic to diffusive conduction, to arrive at the formula

$$\langle G \rangle = \frac{\pi}{2} G_0 N_{\text{strip}} \frac{l_0}{L + 2l_0}, \tag{4.43}$$

for the average conductance in terms of the transport mean free path l_0 and the number $N_{\text{strip}} = |E - U_0|(W/\pi\hbar v)$ of propagating modes in the strip. From the fit of $\langle G \rangle$ versus L in Fig. 4.10 we extract the dependence on ΔU of l_0, and then we use that information to investigate the scaling of the variance of the conductance with system size. As seen in Fig. 4.11, the variance scales well towards the expected value (4.42).

4.6 Conclusion

In conclusion, we have presented in this paper what one might call the "Anderson model for Dirac fermions". Just as in the original Anderson tight-binding model of localization [9], our model is a tight-binding model on a lattice with uncorrelated on-site disorder. Unlike the tight-binding model of graphene (with nearest neighbor hopping on a honeycomb lattice), our model preserves the symplectic symmetry of the Dirac equation – at the expense of a nonlocal finite difference approximation of the transfer matrix.

Our finite difference method is based on a discretization scheme developed in the context of lattice gauge theory [134, 22], with the purpose of resolving the fermion doubling problem. We have adapted this scheme to include the chiral symmetry breaking by a disorder potential, and have cast it in a current-conserving transfer matrix form suitable for the calculation of transport properties.

To test the validity and efficiency of the model, we have calculated the average and the variance of the conductance and compared with earlier numerical and analytical results. We recover the logarithmic increase of the average conductance at the Dirac point, found in numerical calculations that use a momentum space rather than a real space discretization of the Dirac equation [13, 99]. The coefficient that multiplies the logarithm is close to $1/\pi$, in agreement with analytical expectations [121]. The variance of the conductance is enhanced by the absence of intervalley scattering, and we have been able to confirm the scaling with increasing system size towards the expected limit [67, 66] – something which had not been possible in earlier numerical calculations [116] because intervalley scattering sets in before the large-system limit is reached.

Our calculations support the expectation [121] that the statistics of the conductance at the Dirac point scales towards that of a diffusive metal in the large-system limit. This would imply that the shot noise should scale towards a Fano factor $F = 1/3$ [18]. Earlier numerical studies using the momentum space discretization

Figure 4.12: Scaling with system size of the Fano factor (average shot noise power divided by average current) in a disordered strip at the Dirac point (geometry of Fig. 4.5). The length L of the strip is varied at fixed aspect ratio $W/L = 3$. The data are collected for different disorder strengths ΔU (listed in units of $\hbar v/\Delta$). The dotted horizontal line is the value $F = 1/3$ for a diffusive metal. The dotted curve is a fit to $F = 1/3 + a[b + \ln(L/l^*)]^{-1}$, included in order to indicate a possible scaling towards the expected value.

[118] found a saturation at the smaller value of $F = 0.295$. Our own numerical results, shown in Fig. 4.12, instead suggest a slow, logarithmic, increase towards the expected $F = 1/3$. More research on this particular quantity is required for a conclusive answer.

We anticipate that the numerical method developed here will prove useful for the study of graphene with smooth disorder potentials (produced for example by remote charge fluctuations), since such potentials produce little intervalley scattering. Intervalley scattering is absent by construction in the metallic surface states of topological insulators (such as BiSb [55]). These surface states might be

studied by starting from a three-dimensional tight-binding model, but we would expect a two-dimensional formulation as presented here to be more efficient.

Appendix 4.A Current conserving discretization of the current operator

We seek a discretization of the current operator (4.3) that satisfies the condition (4.7) of current conservation. Substitution of the expression (4.20) into the condition (4.7) gives the requirement

$$J_x^{-1} \mathcal{M}_m^\dagger J_x = \mathcal{M}_m^{-1} \Leftrightarrow J_x^{-1} X_m^\dagger J_x = X_m. \tag{4.44}$$

The requirement that Eq. (4.44) holds for any choice of potential fixes the discretization (4.21) of the current operator [up to a multiplicative constant, which follows from the continuum limit (4.3)].

This is an appropriate point to note that current conservation could not have been achieved if the potential would have been discretized in a way that would have resulted in a nonsymmetric matrix $\mathcal{V}_m$. For example, if instead of Eq. (4.11) we would have chosen

$$
\begin{aligned}
V\Psi \to \tfrac{1}{4}\big(&\tilde{V}_{m+1,n}\Psi_{m+1,n} + \tilde{V}_{m+1,n+1}\Psi_{m+1,n+1} \\
&+ \tilde{V}_{m,n}\Psi_{m,n} + \tilde{V}_{m,n+1}\Psi_{m,n+1}\big),
\end{aligned}
\tag{4.45}
$$

with $\tilde{V}_{m,n} = V(x_m, y_n)$, then the corresponding matrix $\mathcal{V}_m$ would have been asymmetric and no choice of J_x could have satisfied Eq. (4.44).

Appendix 4.B Stable multiplication of transfer matrices

To perform the multiplication (4.22) of transfer matrices in a stable way (avoiding exponentially growing and decaying eigenvalues), we use the current conservation relation (4.7) to convert the product

into a composition of unitary matrices (involving only eigenvalues of unit absolute value). The same method was used in Refs. [13, 133, 138], but for a different current operator, so the required transformation formulas need to be adapted.

We separate the spinor degrees of freedom $s = \pm$ of the transfer matrix $\mathcal{M}_m$ into four $N \times N$ blocks,

$$\mathcal{M}_m = \begin{pmatrix} \mathcal{M}_m^{++} & \mathcal{M}_m^{+-} \\ \mathcal{M}_m^{-+} & \mathcal{M}_m^{--} \end{pmatrix}. \tag{4.46}$$

The current conservation relation (4.7) with current operator (4.21) can be written in the canonical form,

$$\tilde{\mathcal{M}}_m^{\dagger} \begin{pmatrix} 1 & 0 \\ 0 & -1 \end{pmatrix} \tilde{\mathcal{M}}_m = \begin{pmatrix} 1 & 0 \\ 0 & -1 \end{pmatrix}, \tag{4.47}$$

in terms of a matrix $\tilde{\mathcal{M}}_m$ related to $\mathcal{M}_m$ by a similarity transformation,

$$\tilde{\mathcal{M}}_m = \mathcal{R}\mathcal{M}_m\mathcal{R}^{-1}, \quad \mathcal{R} = 2^{-1/2} \begin{pmatrix} \mathcal{J}^{1/2} & \mathcal{J}^{1/2} \\ \mathcal{J}^{1/2} & -\mathcal{J}^{1/2} \end{pmatrix}. \tag{4.48}$$

Eq. (4.47) follows only from Eqs. (4.7) and (4.21) if the matrix $\mathcal{R}$ is Hermitian, which it is since $\mathcal{J}$ is Hermitian with only positive eigenvalues [see Eq. (4.15)].

It now follows directly from Eq. (4.7) that the matrix U_m constructed from $\tilde{\mathcal{M}}_m$ by

$$\tilde{\mathcal{M}}_m = \begin{pmatrix} a & b \\ c & d \end{pmatrix} \Leftrightarrow U_m = \begin{pmatrix} -d^{-1}c & d^{-1} \\ a - bd^{-1}c & bd^{-1} \end{pmatrix} \tag{4.49}$$

is a unitary matrix. Matrix multiplication of $\tilde{\mathcal{M}}_m$'s induces a nonlinear composition of U_m's,

$$\tilde{\mathcal{M}}_1 \tilde{\mathcal{M}}_2 \Leftrightarrow U_1 \otimes U_2, \tag{4.50}$$

defined by

$$\begin{pmatrix} A_1 & B_1 \\ C_1 & D_1 \end{pmatrix} \otimes \begin{pmatrix} A_2 & B_2 \\ C_2 & D_2 \end{pmatrix} = \begin{pmatrix} A_3 & B_3 \\ C_3 & D_3 \end{pmatrix}, \tag{4.51a}$$

$$A_3 = A_1 + B_1(1 - A_2 D_1)^{-1} A_2 C_1, \tag{4.51b}$$

$$B_3 = B_1(1 - A_2 D_1)^{-1} B_2, \tag{4.51c}$$

$$C_3 = C_2(1 - D_1 A_2)^{-1} C_1, \tag{4.51d}$$

$$D_3 = D_2 + C_2(1 - D_1 A_2)^{-1} D_1 B_2. \tag{4.51e}$$

To evaluate the product (4.22) of $\mathcal{M}_m$'s in a stable way, we first write it in terms of the matrices $\tilde{\mathcal{M}}_m$,

$$\mathcal{M} = \mathcal{R}^{-1} \left(\prod_{m=1}^{M} \tilde{\mathcal{M}}_m \right) \mathcal{R}. \tag{4.52}$$

We then transform each transfer matrix $\tilde{\mathcal{M}}_m$ into a unitary matrix U_m according to Eq. (4.49) and we compose the unitary matrices according to Eq. (4.51). Each step in this calculation is numerically stable.

At the end of the calculation, we may in principle transform back from the final unitary matrix U to the transfer matrix $\mathcal{M} = \mathcal{R}^{-1} \tilde{\mathcal{M}} \mathcal{R}$ by means of the inverse of relation (4.49),

$$U = \begin{pmatrix} A & B \\ C & D \end{pmatrix} \Leftrightarrow \tilde{\mathcal{M}} = \begin{pmatrix} C - DB^{-1}A & DB^{-1} \\ -B^{-1}A & B^{-1} \end{pmatrix}. \tag{4.53}$$

This inverse transformation is itself unstable, but we may avoid it because [as we can see by comparing Eqs. (4.49) and (4.53) with Eq. (4.33)] the final U is *identical* to the scattering matrix S between leads in the infinite wave vector limit. Hence the conductance can be directly obtained from U via the Landauer formula (4.27) [with the T_n's being the eigenvalues of $BB^\dagger$ and $CC^\dagger$].

Appendix 4.C Crossover from ballistic to diffusive conduction

Away from the Dirac point (for Fermi wave vectors $k_F = |E - U_0|/\hbar v$ in the strip large compared to $1/L$) conduction through the strip is via propagating rather than evanescent modes. If the number $N_{\text{strip}} = k_F W/\pi$ of propagating modes is $\gg 1$, the semiclassical Boltzmann equation can be used to calculate the conductance.

As the transport mean free path l_0 is reduced by adding disorder to the strip, the conduction crosses over from the ballistic to the diffusive regime. How to describe this crossover is a well-known problem in the context of radiative transfer [106]. An exact solution of the Boltzmann equation does not provide a closed-form expression for the crossover, but the following formula has been found to be accurate within a few percent:

$$\langle G \rangle = C_d G_0 N_{\text{strip}} \frac{l_0}{L + 2\zeta}. \tag{4.54}$$

The coefficient C_d depends on the dimensionality d: $C_3 = 4/3$, $C_2 = \pi/2$, $C_1 = 2$. The length ζ is the socalled extrapolation length of radiative transfer theory, equal to l_0 times a numerical coefficient that depends on the reflectivity of the interface at $x = 0$ and $x = L$. An infinite potential step in the Dirac equation has $\zeta = l_0$, see Ref. [124]. Substitution into Eq. (4.54) then gives the formula (4.43) used in the text.

5 Switching of electrical current by spin precession in the first Landau level of an inverted-gap semiconductor

5.1 Introduction

A central goal of spin-transport electronics (or spintronics) is the ability to switch current between spin-selective electrodes by means of spin precession [151]. In the original Datta-Das proposal for such a spin-based transistor [38], the current which is switched carries both spin and charge. It has proven difficult to separate the effects of spin precession from purely orbital effects (deflection of electron trajectories), so most succesful implementations use a nonlocal geometry [60] to modulate the spin current at zero charge current [58, 85, 139]. Even in the absence of an orbital effect, the fact that different electrons (moving along different trajectories) experience different amounts of spin precession prevents a complete switching of the current from one electrode to the other.

If the electron motion could somehow be confined to a single spatial dimension, it would be easier to isolate spin effects from orbital effects and to ensure that all electron spins precess by the same amount. Complete switching of the current would then be possible, limited only by spin relaxation processes. Edge state transport in the quantum Hall effect is one-dimensional and spin selective (in sufficiently strong perpendicular magnetic fields $B_\perp$), but spin precession plays no role in the traditional experiments
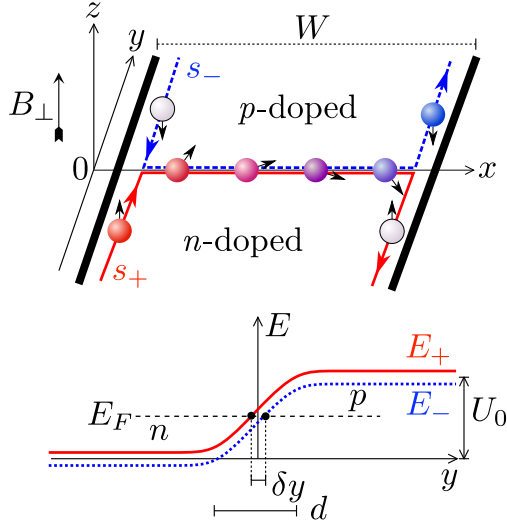
Figure 5.1: Top panel: Schematic illustration of the one-dimensional pathway along which the electron spin is injected, precessed, and detected (filled circles: occupied states; open circles: empty states). Bottom panel: Potential profile of the *p-n* junction, shown for $B_\perp > B_c$ (for $B_\perp < B_c$ the labels E_+ and E_- should be interchanged).

on a two-dimensional electron gas [17]. In this paper we show how the quantum Hall effect in an inverted-gap semiconductor offers the unique possibility to perform a one-dimensional spin precession experiment.

The key idea is to combine the spin-selectivity of edge states with free precession along a *p-n* interface. The geometry, shown in Fig. 5.1, has been studied in graphene [146, 2, 105, 142] – but there spin is only weakly coupled to the orbit and plays a minor role [62, 1]. The strong spin-orbit coupling in inverted-gap semiconductors splits the first Landau level into a pair of levels $E_\pm$ of opposite magnetic moment [74, 123]. One level E_+ (say, with spin up) has electron-like character and produces edge states in the

conduction band. The other level E_- (with spin down) has hole-like character and produces edge states in the valence band. The edge states from E_+ and E_- have opposite chirality, meaning that one circulates clockwise along the edge while the other circulates counter-clockwise. These spin-selective, chiral edge states provide the spin injection at $x = 0$ and detection at $x = W$.

For the spin precession we need to combine states from E_+ and E_-. This is achieved by means of a gate electrode, which creates a smooth potential step (height U_0, width d) centered at $y = 0$, such that the Fermi level lies in the conduction band for $y < 0$ (n-doped region) and in the valence band for $y > 0$ (p-doped region). At the p-n interface states from the first Landau levels E_+ and E_- overlap at the Fermi energy E_F, to form a spin-degenerate one-dimensional state. Spin precession can be realized externally by a parallel magnetic field $B_\parallel$ (in the $x - y$ plane) or internally by bulk or structure inversion asymmetry [74].

Good overlap at E_F of the states from E_+ and E_- is crucial for effective spin precession. The requirement is that the spatial separation $\delta y \simeq |E_+ - E_-| d / U_0$ of the states should be small compared to the magnetic length $l_m = (\hbar / e B_\perp)^{1/2}$ (which sets their spatial extent). This is where the inverted gap comes in, as we now explain.

Inversion of the gap means that the first Landau level in the conduction band goes down in energy with increasing magnetic field (because it has hole-like character), while the first Landau level in the valence band goes up in energy (because it has electron-like character). As a consequence, the gap $|E_+ - E_-|$ has a minimal value E_c much less than the cyclotron energy $\hbar \omega_c$ at a crossover magnetic field B_c. Indeed, $E_c = 0$ in the absence of inversion asymmetry [74]. Good overlap can therefore be reached in an inverted-gap semiconductor, simply by tuning the magnetic field. In a normal (non-inverted) semiconductor, such as GaAs, the cyclotron energy difference between E_+ and E_- effectively prevents the overlap of Landau levels from conduction and valence bands.

In the following two sections, we first present a general, model independent analysis and then specialize to the case of a HgTe

quantum well (where we test the analytical theory by computer simulation).

5.2 General theory

We introduce a one-dimensional coordinate $s_\pm$ along the $E_\pm$ edge states, increasing in the direction of the chirality (see Fig. 5.1). The wave amplitudes $\psi_\pm(s_\pm)$ of these two states can be combined into the spinor $\Psi = (\psi_+, \psi_-)$. Far from the *p-n* interface, ψ_+ and ψ_- evolve independently with Hamiltonian

$$H_0 = \begin{pmatrix} H_+ & 0 \\ 0 & H_- \end{pmatrix}, \quad H_\pm = v_\pm \left(-i\hbar \frac{\partial}{\partial s_\pm} - p_F^\pm \right). \qquad (5.1)$$

This is the generic linearized Hamiltonian of a chiral mode, with group velocity $v_\pm \equiv v(s_\pm)$ and Fermi momentum $p_F^\pm \equiv p_F(s_\pm)$. Near the *p-n* interface the spin-up and spin-down states are coupled by the generic precession Hamiltonian,

$$H_{\text{prec}} = \begin{pmatrix} 0 & \mathcal{M}^* \\ \mathcal{M} & 0 \end{pmatrix}, \qquad (5.2)$$

with a matrix element $\mathcal{M}$ to be specified later.

We seek the transfer matrix T, defined by

$$\Psi(s_+^f, s_-^f) = T\Psi(s_+^i, s_-^i). \qquad (5.3)$$

We take for Ψ a solution of the Schrödinger equation,

$$(H_0 + H_{\text{prec}})\Psi = 0, \qquad (5.4)$$

at zero excitation energy (appropriate for electrical conduction in linear response). The initial and final points $s_\pm^i$ and $s_\pm^f$ are taken away from the *p-n* interface. The unitary scattering matrix S (relating incident and outgoing current amplitudes) is related to T by a similarity transformation,

$$S = \begin{pmatrix} v_+^f & 0 \\ 0 & v_-^f \end{pmatrix}^{1/2} T \begin{pmatrix} v_+^i & 0 \\ 0 & v_-^i \end{pmatrix}^{-1/2}. \qquad (5.5)$$

The two-terminal linear-response conductance G of the p-n junction is given by the Landauer formula,

$$G = \frac{e^2}{h} |S_{21}|^2. \tag{5.6}$$

The transition matrix element $\mathcal{M}(s_+, s_-)$ between $\psi_+(s_+)$ and $\psi_-(s_-)$ vanishes if the separation $|s_+ - s_-|$ of the two states is large compared to the magnetic length l_m. We assume that $B_\perp$ is sufficiently close to B_c that $|s_+ - s_-| < l_m$ at the p-n interface $y = 0$, $0 < x < W$, where we may take $\mathcal{M} = $ constant (independent of x). At the two edges $x = 0$ and $x = W$ we set $\mathcal{M} = 0$, neglecting the crossover region within l_m of $(0,0)$ and $(W,0)$. (The precession angle there will be small compared to unity for $l_m \ll \hbar v_\pm / |\mathcal{M}|$.)

In this "abrupt approximation" we may identify the initial and final coordinates $s_\pm^i$ and $s_\pm^f$ with the points $(0,0)$ and $(W,0)$, at the two ends of the p-n interface. Integration of the Schrödinger equation (5.4) along the p-n interface gives the transfer matrix, and application of Eq. (5.5) then gives the scattering matrix

$$S = \exp\left[-i\frac{W}{\hbar} \begin{pmatrix} p_F^+ & \mathcal{M}^*/\sqrt{v_+ v_-} \\ \mathcal{M}/\sqrt{v_+ v_-} & p_F^- \end{pmatrix} \right]. \tag{5.7}$$

(We have assumed that $v_\pm$ and $p_F^\pm$, as well as $\mathcal{M}$, do not vary along the p-n interface, so we may omit the labels i, f.) One verifies that S is unitary, as it should be.

Evaluation of the matrix exponent in Eq. (5.7) and substitution into Eq. (5.6) gives the conductance,

$$G = \frac{e^2}{h} \sin^2\left(\frac{|\boldsymbol{p}_{\text{eff}}|W}{\hbar} \right) \sin^2 \alpha. \tag{5.8}$$

The effective precession momentum

$$\boldsymbol{p}_{\text{eff}} = \left(\frac{\text{Re}\,\mathcal{M}}{\bar{v}}, \frac{\text{Im}\,\mathcal{M}}{\bar{v}}, \frac{\delta p_F}{2} \right) \tag{5.9}$$

(with $\delta p_F = p_F^+ - p_F^-$ and $\bar{v} = \sqrt{v_+ v_-}$) makes an angle α with the z-axis. This is the final result of our general analysis.

5.3 Application to a HgTe quantum well

We now turn to a specific inverted-gap semiconductor, a quantum well consisting of a 7 nm layer of HgTe sandwiched symmetrically between $Hg_{0.3}Cd_{0.7}Te$ [73]. The properties of this socalled topological insulator have been reviewed in [74]. The low-energy excitations are described by a four-orbital tight-binding Hamiltonian [23, 44],

$$H = \sum_n c_n^\dagger \mathcal{E}_n c_n - \sum_{n,m \text{ (nearest neighb.)}} c_n^\dagger \mathcal{T}_{nm} c_m. \qquad (5.10)$$

Each site n on a square lattice (lattice constant $a = 4\,\text{nm}$) has four states $|s, \pm\rangle$, $|p_x \pm ip_y, \pm\rangle$ – two electron-like s-orbitals and two hole-like p-orbitals of opposite spin $\sigma = \pm$. Annihilation operators $c_{n,\tau\sigma}$ for these four states (with $\tau \in \{s, p\}$) are collected in a vector

$$c_n = (c_{n,s+}, c_{n,p+}, c_{n,s-}, c_{n,p-}).$$

States on the same site are coupled by the 4×4 potential matrix $\mathcal{E}_n$ and states on adjacent sites by the 4×4 hopping matrix $\mathcal{T}_{nm}$.

In zero magnetic field and without inversion asymmetry H decouples into a spin-up block H_+ and a spin-down block H_-, defined in terms of the 2×2 matrices

$$\mathcal{E}_n^+ = \mathcal{E}_n^- = \text{diag}\,(\varepsilon_s - U_n, \varepsilon_p - U_n), \qquad (5.11)$$

$$\mathcal{T}_{nm}^+ = \left(\mathcal{T}_{nm}^-\right)^* = \begin{pmatrix} t_{ss} & t_{sp}e^{i\theta_{nm}} \\ t_{sp}e^{-i\theta_{mn}} & -t_{pp} \end{pmatrix}. \qquad (5.12)$$

Here U_n is the electrostatic potential and θ_{nm} is the angle between the vector $r_n - r_m$ and the positive x-axis (so $\theta_{mn} = \pi - \theta_{nm}$). The orbital effect of a perpendicular magnetic field $B_\perp$ is introduced into the hopping matrix elements by means of the Peierls substitution

$$\mathcal{T}_{nm} \mapsto \mathcal{T}_{nm} \exp[i(eB_\perp/\hbar)(y_n - y_m)x_n].$$

This breaks the degeneracy of the spin-up and spin-down energy levels, but it does not couple them.

Spin-up and spin-down states are coupled by the Zeeman effect from a parallel magnetic field (with gyromagnetic factor $g_\parallel$) and by spin-orbit interaction without inversion symmetry (parameterized by a vector $\mathbf{\Delta}$). In first-order perturbation theory, the correction $\delta\mathcal{E}$ to the on-site potential has the form [74]

$$\delta\mathcal{E} = (\mathbf{\Delta}\cdot\boldsymbol{\sigma})\otimes\tau_y + \tfrac{1}{2}\mu_B g_\parallel(\mathbf{B}_\parallel\cdot\boldsymbol{\sigma})\otimes(\tau_0+\tau_z)$$
$$+ \mu_B B_\perp\sigma_z\otimes(\bar{g}_\perp\tau_0 + \delta g_\perp\tau_z). \tag{5.13}$$

The Pauli matrices $\boldsymbol{\sigma} = (\sigma_x,\sigma_y,\sigma_z)$ act on the spin-up and spin-down blocks, while the Pauli matrices τ_y, τ_z and the unit matrix τ_0 act on the orbital degree of freedom s, p within each block.

The parameters of the tight-binding model for a 7 nm thick HgTe/Hg$_{0.3}$Cd$_{0.7}$Te quantum well (grown in the (001) direction) are as follows [74]: $t_{ss} = 74.9$ meV, $t_{pp} = 10.9$ meV, $t_{sp} = 45.6$ meV, $\varepsilon_s = 289.5$ meV, $\varepsilon_p = -33.5$ meV, $\bar{g}_\perp = 10.75$, $\delta g_\perp = 11.96$, $g_\parallel = -20.5$, $\mathbf{\Delta} = (0, 1.6$ meV$, 0)$.

The quantum well is symmetric, so only bulk inversion asymmetry contributes to $\mathbf{\Delta}$. The *p-n* junction is defined by the potential profile

$$U(x,y) = \tfrac{1}{2}U_0[1 + \tanh(4y/d)], \quad 0 < x < W, \tag{5.14}$$

with $U_0 = 32$ meV, $d = 12$ nm, and $W = 0.8\,\mu$m. We fix the Fermi level at $E_F = 25$ meV, so that it lies in the conduction band for $y < 0$ and in the valence band for $y > 0$. (We have checked that none of the results are sensitive to the choice of potential profile or parameter values.) The scattering matrix of the *p-n* junction is calculated with the recursive Green function technique, using the "knitting" algorithm[1] of Ref. [65]. Results for G as a function of $\mathbf{B}_\parallel$ are shown in Figs. 5.2 and 5.3.

The dependence of the conductance on the parallel magnetic field $\mathbf{B}_\parallel$ shows a striking "bullseye" pattern, which can be understood

---

[1] The computer code for the knitting algorithm was kindly provided to us by Dr. Waintal.
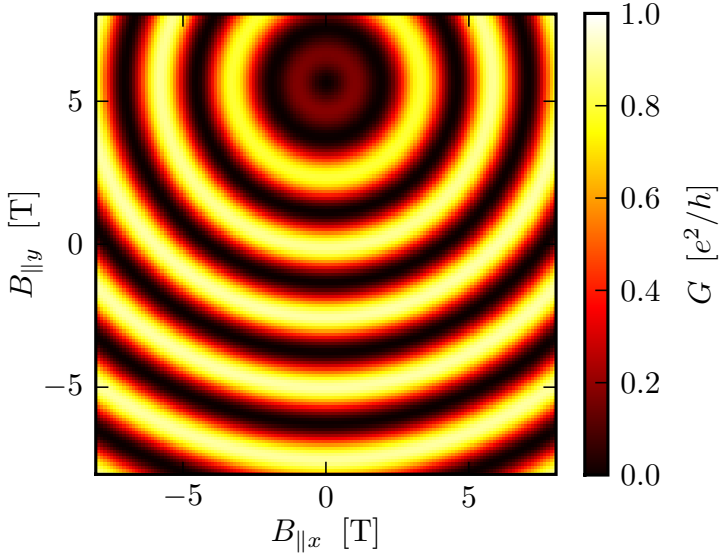
Figure 5.2: Dependence of the conductance of the HgTe quantum well on the parallel magnetic field $B_\parallel$, calculated from the tight-binding model for $B_\perp = B_c = 6.09\,\mathrm{T}$.

as follows. To first order in $B_\parallel$, the edge state parameters $v_\pm$ and $p_F^\pm$ are constant, while the precession matrix element

$$\mathcal{M} = \Delta_{\mathrm{eff}} + \mu_B g_{\mathrm{eff}}(B_{\parallel x} + iB_{\parallel y}) \qquad (5.15)$$

varies linearly. Substitution into Eqs. (5.8) and (5.9) gives a circularly symmetric dependence of G on $B_\parallel$,

$$G = \frac{e^2}{h}\left(1 + \frac{(\bar{v}\delta p_F)^2}{4|\mu_B g_{\mathrm{eff}}|^2|\boldsymbol{B}_\parallel - \boldsymbol{B}_0|^2}\right)^{-1}$$

$$\times \sin^2\left[\frac{W}{\hbar\bar{v}}\sqrt{|\mu_B g_{\mathrm{eff}}|^2|\boldsymbol{B}_\parallel - \boldsymbol{B}_0|^2 + \tfrac{1}{4}(\bar{v}\delta p_F)^2}\right], \qquad (5.16)$$

$$\boldsymbol{B}_0 = \mu_B^{-1}\big(\mathrm{Re}[\Delta_{\mathrm{eff}}/g_{\mathrm{eff}}], \mathrm{Im}[\Delta_{\mathrm{eff}}/g_{\mathrm{eff}}], 0\big). \qquad (5.17)$$

The parallel magnetic field B_0 corresponds to the center of the bullseye, at which the coupling between the $\pm$ edge states along
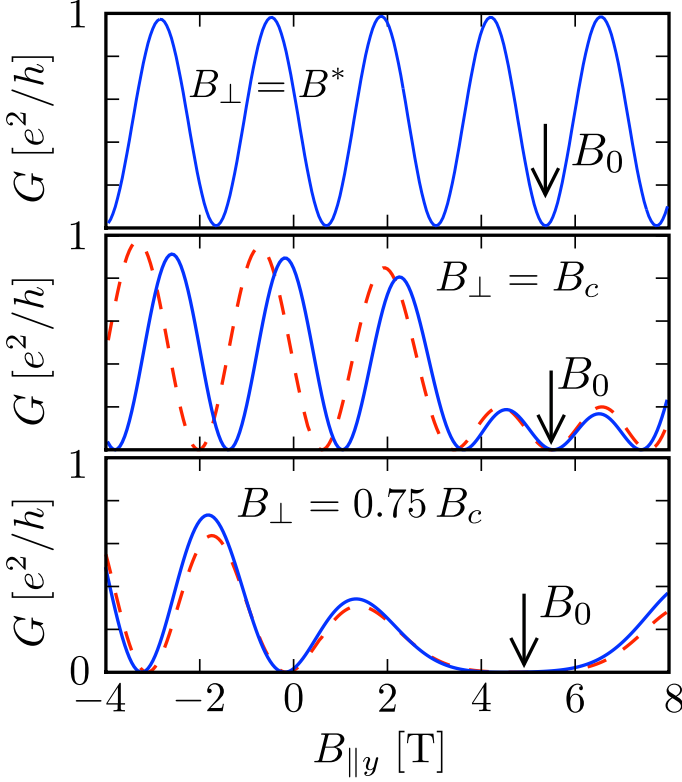
Figure 5.3: Dependence of the conductance on $B_{\|y}$ for $B_{\|x} = 0$, at three values of the perpendicular magnetic field. The solid curves are calculated numerically from the tight-binding model, the dashed curves are the analytical prediction (5.16). The arrow indicates the value of B_0 from Eq. (5.17). (Only the numerical curve is shown in the upper panel, because the analytical curve is nearly indistinguishable from it.)

the *p-n* interface by bulk inversion asymmetry is cancelled by the Zeeman effect.

The Fermi momentum mismatch δp_F vanishes at a perpendicular magnetic field B^* close to, but not equal to, B_c. Then the

magnetoconductance oscillations are purely sinusoidal,

$$G = \frac{e^2}{h} \sin^2[(W/\hbar\bar{v})\mu_B g_{\text{eff}}|\boldsymbol{B}_\parallel - \boldsymbol{B}_0|].\qquad(5.18)$$

For a quantitative comparison between numerics and analytics, we extract the parameters $v_\pm$ and $p_F^\pm$ from the dispersion relation of the edge states $\psi_\pm$ along an infinitely long p-n interface (calculated for uncoupled blocks $H_\pm$). The overlap of ψ_+ and ψ_- determines the coefficients

$$\Delta_{\text{eff}} = (\Delta_x + i\Delta_y)\langle\psi_-|\tau_y|\psi_+\rangle,\qquad(5.19)$$

$$g_{\text{eff}} = \tfrac{1}{2}g_\parallel\langle\psi_-|\tau_0 + \tau_z|\psi_+\rangle.\qquad(5.20)$$

For $B_\perp = B_c = 6.09\,\text{T}$ we find $\bar{v}\delta p_F = 0.86\,\text{meV}$, $\hbar\bar{v}/W = 0.23\,\text{meV}$, $\Delta_{\text{eff}} = -1.59\,\text{meV}$, $g_{\text{eff}} = -4.99$. The Fermi momentum mismatch δp_F vanishes for $B_\perp = B^* = 5.77\,\text{T}$. Substitution of the parameters into Eq. (5.16) gives the dashed curves in Fig. 5.3, in reasonable agreement with the numerical results from the tight-binding model (solid curves). In particular, the value of B_0 extracted from the numerics is within a few percent of the analytical prediction (5.17).

Because of the one-dimensionality of the motion along the p-n interface, electrostatic disorder and thermal averaging have a relatively small perturbing effect on the conductance oscillations. For disorder potentials ΔU and thermal energies $k_B T$ up to 10% of U_0 the perturbation is hardly noticeable (a few percent). As shown in Fig. 5.4, the conductance oscillations remain clearly visible even for ΔU and $k_B T$ comparable to U_0. In particular, we have found that the center of the bullseye pattern remains within 10% of B_0 even for ΔU as large as the p-n step height U_0.

5.4 Conclusion

In conclusion, we have proposed a one-dimensional spin precession experiment at a p-n junction in an inverted-gap semiconductor. The
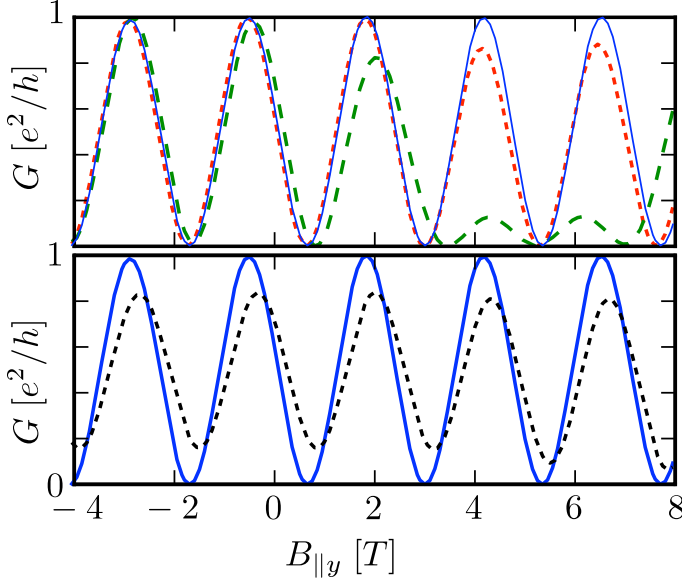
Figure 5.4: The solid blue curve in both panels is the same as in Fig. 5.3, top panel, calculated for $B_\perp = B^*$ from the tight-binding model at zero temperature without any disorder. The dotted black curve in the lower panel shows the effect of raising the temperature to $30\,\mathrm{K} \approx U_0/3k_B$. The dotted red curve and dashed green curve in the upper panel show the effect of disorder at zero temperature. The on-site disorder potential is drawn uniformly from the interval $(-\Delta U_0, \Delta U_0)$, with, respectively, $\Delta U = U_0/4$ and $\Delta U = U_0/2$.

conductance as a function of parallel magnetic field oscillates in a bullseye pattern, centered at a field B_0 proportional to the matrix element Δ_{eff} of the bulk inversion asymmetry. Our numerical and analytical calculations show conductance oscillations of amplitude not far below e^2/h, robust to disorder and thermal averaging. Realization of the proposed experiment in a HgTe quantum well [74] (or in other inverted-gap semiconductors [82]) would provide a

unique demonstration of full-current switching by spin precession.

As directions for future research, we envisage potential applications of this technique as a sensitive measurement of the degree of bulk inversion asymmetry, or as a probe of the effects of interactions on spin precession. It might also be possible to eliminate the external magnetic field and realize electrical switching of the current in our setup: The role of the perpendicular magnetic field in producing spin-selective edge states can be taken over by magnetic impurities or a ferromagnetic layer [83], while the role of the parallel magnetic field in providing controlled spin precession can be taken over by gate-controlled structural inversion asymmetry.

6 Theory of the topological Anderson insulator

6.1 Introduction

Topological insulators continue to surprise with unexpected physical phenomena [30]. A recent surprise was the discovery of the topological Anderson insulator (TAI) by Li, Chu, Jain, and Shen [81]. In computer simulations of a HgTe quantum well, these authors discovered in the phase diagram a transition from an ordinary insulating state (exponentially small conductance) to a state with a quantized conductance of $G_0 = 2e^2/h$. The name TAI refers to the latter state. The findings of Ref. [81] were confirmed by independent simulations [59].

The phenomenology of the TAI is similar to that of the quantum spin Hall (QSH) effect, which is well understood [62, 23] and observed experimentally in HgTe quantum wells [70, 74, 113]. The QSH effect is a band structure effect: It requires a quantum well with an inverted band gap, modeled by an effective Dirac Hamiltonian with a negative (socalled "topological") mass. The matching of this negative mass inside the system to the usual positive mass outside leaves edge states in the gap. The edge states are "helical", in the sense that the direction of propagation is tied to the electron spin. Opposite edges each contribute e^2/h to the conductance. The conductance remains quantized in the presence of (weak) disorder, because time reversal symmetry forbids scattering between counter-propagating edge states (of opposite helicity) [62, 23, 70, 74, 113].

The crucial difference between the TAI and QSH phases is that

the QSH phase extends down to zero disorder, while the TAI phase has a boundary at a minimal disorder strength. Put differently, the helical edge states in the QSH phase exist *in spite of* disorder, while in the TAI phase they exist *because of* disorder. Note that the familiar quantum Hall effect is like the QSH effect in this respect: The edge states in the quantum Hall effect exist already without disorder (although, unlike the QSH effect, they only form in a strong magnetic field).

The computer simulations of Refs. [81, 59] confront us, therefore, with a phenomenology without precedent: By what mechanism can disorder produce edge states with a quantized conductance? That is the question we answer in this paper.

6.2 Model

We start from the low-energy effective Hamiltonian of a HgTe quantum well, which has the form [23]

$$H = \alpha(p_x\sigma_x - p_y\sigma_y) + (m + \beta p^2)\sigma_z + [\gamma p^2 + U(r)]\sigma_0. \quad (6.1)$$

This is a two-dimensional Dirac Hamiltonian (with momentum operator $p = -i\hbar\nabla$, Pauli matrices σ_x, σ_y, σ_z, and a 2×2 unit matrix σ_0), acting on a pair of spin-orbit coupled degrees of freedom from conduction and valence bands. The complex conjugate H^* acts on the opposite spin. We assume time reversal symmetry (no magnetic field or magnetic impurities) and neglect any coupling between the two spin blocks H and H^*[1]. The scalar potential U accounts for the disorder. The parameters α, β, γ, m depend on the thickness and composition of the quantum well [74]. For the specific calculations that follow, we will use the same parameter

---

[1]We have repeated the calculations of the conductance including a coupling Hamiltonian between the spin blocks of the form $\pm i\kappa\sigma_y$, with $\kappa = 1.6\,\mathrm{meV}$, representative of bulk inversion asymmetry in a HgTe quantum well. The effect on the phase diagram was negliglibly small.

values as in Ref. [81], representative of a non-inverted HgTe/CdTe quantum well[2].

The terms quadratic in momentum in Eq. (6.1) are not present in the Dirac Hamiltonian familiar from relativistic quantum mechanics, but they play an important role here. In particular, it is the relative sign of β and m that determines whether the clean quantum well ($U \equiv 0$) is inverted ($\beta m < 0$) or not-inverted ($\beta m > 0$). We take $\beta > 0$, so the inverted quantum well has a negative topological mass $m < 0$. The inverted quantum well is a topological insulator (for Fermi energies E_F inside the gap), while the non-inverted quantum well is an ordinary band insulator. The phase transition between these two types of insulators therefore occurs at $m = 0$ in a clean quantum well.

6.3 TAI mechanism

We will now show that disorder can push the phase transition to positive values of m, which is the hallmark of a TAI. Qualitatively, the mechanism is as follows. Elastic scattering by a disorder potential causes states of definite momentum to decay exponentially as a function of space and time. The quadratic term $\beta p^2 = -\hbar^2 \beta \nabla^2$ in H, acting on the decaying state $\propto e^{-x/\lambda}$, adds a negative correction δm to the topological mass. The renormalized mass $\bar{m} = m + \delta m$ can therefore have the opposite sign as the bare mass m. Topological mass renormalization by disorder, and the resulting change in the phase diagram, has previously been studied without the terms quadratic in momentum [127]. The sign of $\bar{m}$ and m then remains the same and the TAI phase cannot appear.

We extract the renormalized topological mass $\bar{m}$, as well as the renormalized chemical potential $\bar{\mu}$, from the self-energy Σ of the disorder-averaged effective medium. To make contact with the

---

[2]The parameter values of H that we have used are: $\hbar\alpha = 364.5\,\text{meV nm}$, $\hbar^2\beta = 686\,\text{meV nm}^2$, $\hbar^2\gamma = 512\,\text{meV nm}^2$, $m = 1\,\text{meV}$. The lattice constant of the discretization was $a = 5\,\text{nm}$.

computer simulations [81, 59], we discretize H on a square lattice (lattice constant a) and take a random on-site disorder potential U, uniformly distributed in the interval $(-U_0/2, U_0/2)$. We denote by $H_0(\boldsymbol{k})$ the lattice Hamiltonian of the clean quantum well in momentum representation [23, 74].

The self-energy, defined by

$$(E_F - H_0 - \Sigma)^{-1} = \langle (E_F - H)^{-1} \rangle, \qquad (6.2)$$

with $\langle \cdots \rangle$ the disorder average, is a 2×2 matrix which we decompose into Pauli matrices: $\Sigma = \Sigma_0 \sigma_0 + \Sigma_x \sigma_x + \Sigma_y \sigma_y + \Sigma_z \sigma_z$. The renormalized topological mass and chemical potential are then given by

$$\bar{m} = m + \lim_{k \to 0} \operatorname{Re} \Sigma_z, \quad \bar{\mu} = E_F - \lim_{k \to 0} \operatorname{Re} \Sigma_0. \qquad (6.3)$$

The phase boundary of the topological insulator is at $\bar{m} = 0$, while the Fermi level enters the (negative) band gap when $|\bar{\mu}| = -\bar{m}$.

In the selfconsistent Born approximation, Σ is given by the integral equation [126]

$$\Sigma = \tfrac{1}{12} U_0^2 (a/2\pi)^2 \int_{\mathrm{BZ}} d\boldsymbol{k} \, [E_F + i0^+ - H_0(\boldsymbol{k}) - \Sigma]^{-1}. \qquad (6.4)$$

(The integral is over the first Brillouin zone.) The self-energy is independent of momentum and diagonal (so there is no renormalization of the parameters α, β, γ). By calculating $\bar{m}$ and $\bar{\mu}$ as a function of E_F and U_0 we obtain the two curves A and B in Fig. 6.1.

We have also derived an approximate solution in closed form[3],

$$\bar{m} = m - \frac{U_0^2 a^2}{48\pi\hbar^2} \frac{\beta}{\beta^2 - \gamma^2} \ln \left| \frac{\beta^2 - \gamma^2}{E_F^2 - m^2} \left(\frac{\pi\hbar}{a} \right)^4 \right|, \qquad (6.5a)$$

$$\bar{\mu} = E_F - \frac{U_0^2 a^2}{48\pi\hbar^2} \frac{\gamma}{\beta^2 - \gamma^2} \ln \left| \frac{\beta^2 - \gamma^2}{E_F^2 - m^2} \left(\frac{\pi\hbar}{a} \right)^4 \right|, \qquad (6.5b)$$

---

[3]The approximate solution (6.5) of Eq. (6.4) amounts to the Born approximation without selfconsistency (replacing Σ in the right-hand-side by zero) and keeping only the logarithmically divergent part of the integral.

showing that the correction $\delta m = \bar{m} - m$ to the topological mass by disorder is *negative* – provided $\beta > \gamma$. For $\beta < \gamma$ the clean HgTe quantum well would be a semimetal, lacking a gap in the entire Brillouin zone. Neither the TAI phase nor the QSH phase would then appear. In HgTe the parameter β is indeed larger than γ, but not by much[4]. Eq. (6.5) implies that the lower branch of curve B (defined by $\bar{\mu} = \bar{m} < 0$) is then fixed at $E_F \approx m > 0$ independent of U_0. This explains the puzzling absence of the TAI phase in the valence band ($E_F < 0$), observed in the computer simulations [81, 59].

To quantitatively test the phase diagram resulting from the effective medium theory, we performed computer simulations similar to those reported in Refs. [81, 59]. The conductance G is calculated from the lattice Hamiltonian [23, 74] in a strip geometry, using the method of recursive Green functions. The strip consists of a rectangular disordered region (width W, length L), connected to semi-infinite, heavily doped, clean leads[5]. Theory and simulation are compared in Figs. 6.1 and 6.2.

Fig. 6.1 shows the phase diagram. The weak-disorder boundary of the TAI phase observed in the simulations is described quite well by the selfconsistent Born approximation (curve B) – *without any adjustable parameter*. Curve B limits the region where (A) the renormalized topological mass $\bar{m}$ is negative *and* (B) the renormalized chemical potential $\bar{\mu}$ lies inside the band gap: $|\bar{\mu}| < -\bar{m}$. Condition (A) is needed for the existence of edge states with a quantized conductance. Condition (B) is not needed for an infinite system, because then Anderson localization suppresses conductance via bulk states as well as coupling of edge states at opposite edges. In the relatively small systems accessible by computer simulation, the localization length for weak disorder remains larger than the system size (see later). Condition (B) is then needed to eliminate

---

[4]See footnote on page 95.

[5]The reason we dope the leads in the computer simulations is to be able to access the region $|E_F| < m$ in the phase diagram, where the band gap in the clean leads would otherwise prevent conduction through the disordered region.
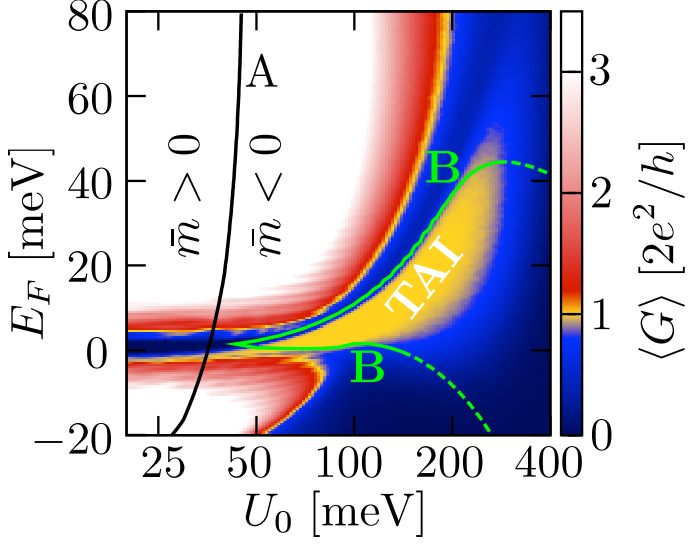
Figure 6.1: Computer simulation of a HgTe quantum well (for parameters see footnote on page 95), showing the average conductance $\langle G \rangle$ as a function of disorder strength U_0 (logarithmic scale) and Fermi energy E_F, in a disordered strip of width $W = 100\,a$ and length $L = 400\,a$. The TAI phase is indicated. Curves A and B are the phase boundaries resulting from the effective medium theory. Curve A separates regions with positive and negative renormalized topological mass $\bar{m}$, while curve B marks the crossing of the renormalized chemical potential $\bar{\mu}$ with the band edge ($|\bar{\mu}| = -\bar{m}$). Both curves have been calculated *without any adjustable parameter*. The phase boundary of the TAI at strong disorder is outside of the regime of validity of the effective medium theory.

the bulk conductance and to decouple the edge states.

Fig. 6.2 shows the average density of states ρ at the Fermi level. The agreement between the selfconsistent Born approximation (dashed black curve) and the computer simulation (solid black) is
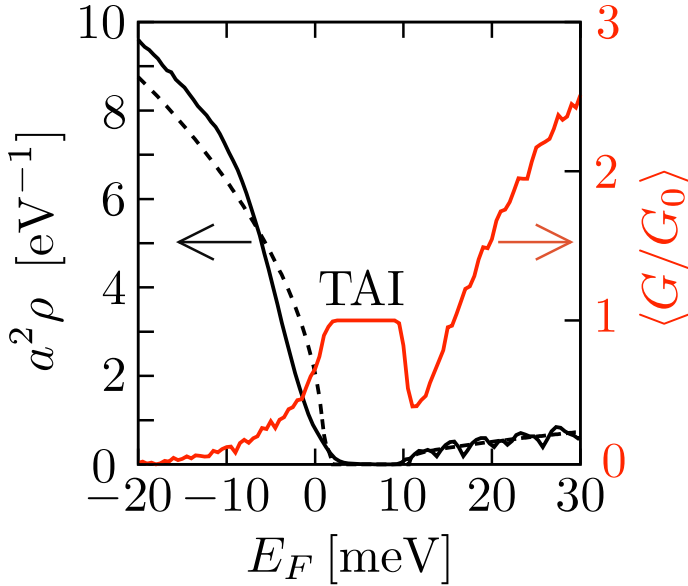
Figure 6.2: Black curves, left axis: Average density of states ρ as a function of E_F for $U_0 = 100\,\text{meV}$, calculated by computer simulation (solid curve, for a disordered $100\,a \times 100\,a$ square with periodic boundary conditions) or by effective medium theory (dashed curve). Red curve, right axis: Average conductance $\langle G \rangle$, calculated by computer simulation in a disordered strip ($U_0 = 100\,\text{meV}$, $W = 100\,a$, $L = 400\,a$). The TAI phase of quantized conductance lines up with the band gap.

quite good, in particular considering the fact that this plot is for a disorder strength which is an order of magnitude larger than the band gap. The range of Fermi energies over which the gap extends lines up nicely with the conductance plateau, shown in the same figure (red curve).

The strong-disorder phase boundary of the TAI cannot be described by effective medium theory, but it should be similar to the QSH phase boundary. In the QSH effect the strong-disorder transi-
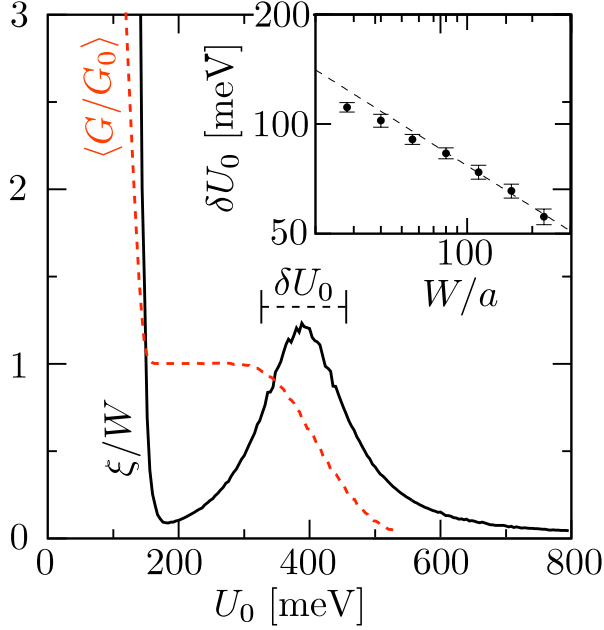
Figure 6.3: Red dashed curve: Average conductance $\langle G \rangle$ as a func-
tion of disorder strength ($E_F = 25\,\mathrm{meV}$, $W = L = 100\,a$).
Black solid curve: Localization length ξ, showing the
peak at the strong-disorder edge of the conductance
plateau – characteristic of a localization transition. The
scaling with system size W of the width δU_0 of the peak
is shown in the inset (double-logarithmic plot).

tion is in the universality class of the quantum Hall effect [102] –
in the absence of coupling between the spin blocks [103, 101]. To
ascertain the nature of the strong-disorder transition out of the TAI,
we have calculated the critical exponent ν governing the scaling of
the localization length ξ. For that purpose we roll up the strip into
a cylinder, thereby eliminating the edge states [59]. We determine
the localization length $\xi \equiv -2\lim_{L\to\infty} L \langle \ln G/G_0 \rangle^{-1}$ by increasing
the length L of the cylinder at fixed circumference W.

   In Fig. 6.3 we show ξ as a function of disorder strength U_0 at $E_F =$

$25\,meV$, $W = 100\,a$. As mentioned above, ζ becomes much larger than W upon crossing the weak-disorder boundary of the TAI, so there is no localization there[6]. At the strong-disorder boundary, however, the dependence of ζ on U_0 shows the characteristic peak of a localization transition [42]. In the inset we plot the scaling with W of the width δU_0 at half maximum of the peak. This yields the critical exponent via $\delta U_0 \propto W^{-1/\nu}$. We find $\nu = 2.66 \pm 0.15$, consistent with the value $\nu = 2.59$ expected for a phase transition in the quantum Hall effect universality class [132].

6.4 Conclusion

In conclusion, we have identified the mechanism for the appearance of a disorder-induced phase of quantized conductance in computer simulations of a HgTe quantum well [81, 59]. The combination of a random potential and quadratic momentum terms in the Dirac Hamiltonian can change the sign of the topological mass, thereby transforming a non-inverted quantum well (without edge states in the band gap) into an inverted quantum well (with edge states). The weak-disorder boundary in the phase diagram of the TAI has been calculated by effective medium theory, in good agreement with the simulations (curve B in Fig. 6.1).

Contrary to what the name "topological Anderson insulator" might suggest, we have found that the hallmark of the TAI in the simulations, the weak-disorder transition into a phase of quantized conductance, is not an Anderson transition at all. Instead, the weak-disorder boundary B marks the crossing of a band edge rather than a mobility edge. A mobility edge (similar to the QSH

---

[6]A pronounced conductance dip between the quantized plateau and the high-conductance regime exists for samples with a large aspect ratio L/W, becoming broader and broader with increasing L/W. The dip is clearly visible in Fig. 6.2 (for $L/W = 4$) and absent in Fig. 6.3 (for $L/W = 1$). Our numerical data suggests that the conductance dip extends over the parameter range where $W < \zeta < L$, so that conduction is suppressed both through the bulk and along the edges.

effect [102, 103, 101]) is crossed at strong disorder, as evidenced by the localization length scaling (Fig. 6.3).

Our findings can be summed up in one sentence: "A topological insulator *wants* to be topological". The mechanism for the conversion of an ordinary insulator into a topological insulator that we have discovered is generically applicable to narrow-band semiconductors with strong spin-orbit coupling (since these are described by a Dirac equation, which generically has quadratic momentum terms [150]). There is no restriction to dimensionality. We expect, therefore, a significant extension of the class of known topological insulators[7] to disordered materials without intrinsic band inversion.

---

[7]For introductions to topological insulators, see [149, 30, 95]

References

[1] D. A. Abanin, P. A. Lee, and L. S. Levitov, Phys. Rev. Lett. **96**, 176803 (2006).

[2] D. A. Abanin and L. S. Levitov, Science **317**, 641 (2007).

[3] S. Adam, E. H. Hwang, V. Galitski, and S. Das Sarma, Proc. Natl. Acad. Sci. USA **104**, 18392 (2007).

[4] S. Adam and S. Das Sarma, Phys. Rev. B **77**, 115436 (2008).

[5] A. R. Akhmerov and C. W. J. Beenakker, Phys. Rev. Lett. **98**, 157003 (2007).

[6] I. L. Aleiner and K. B. Efetov, Phys. Rev. Lett. **97**, 236801 (2006).

[7] S. Alexander and R. Orbach, J. Phys. Lett. (Paris) **43**, L625 (1982).

[8] A. Altland, Phys. Rev. Lett. **97**, 236802 (2006).

[9] P. W. Anderson, Phys. Rev. **109**, 1492 (1958).

[10] T. Ando, T. Nakanishi, and R. Saito, J. Phys. Soc. Japan **67**, 2857 (1998).

[11] Daniel ben-Avraham and Shlomo Havlin, *Diffusion and Reactions in Fractals and Disordered Systems* (Cambridge University Press, 2000).

[12] D. A. Bagrets and Yu. V. Nazarov, Phys. Rev. B **67**, 085316 (2003).

[13] J. H. Bardarson, J. Tworzydło, P. W. Brouwer, and C. W. J. Beenakker, Phys. Rev. Lett. **99**, 106801 (2007).

[14] E. Barkai, V. Fleurov, and J. Klafter, Phys. Rev. E **61** 1164 (2000).

[15] P. Barthelemy , J. Bertolotti, and D. S. Wiersma, Nature **453**, 495 (2008).

[16] F. Bartumeus, M. G. E. Da Luz, G. M. Viswanathan, and J. Catalan, Ecology **86**, 3078 (2005).

[17] C. W. J. Beenakker and H. van Houten, Solid State Phys. **44**, 1 (1991); arXiv:cond-mat/0412664.

[18] C. W. J. Beenakker and M. Büttiker, Phys. Rev. B **46**, 1889 (1992).

[19] C. W. J. Beenakker and C. Schönenberger, Physics Today, May 2003, p. 37.

[20] C. W. J. Beenakker, Rev. Mod. Phys. **80**, 1337 (2008).

[21] D. Ben-Avraham and S. Havlin, J. Phys. A **15**, L691 (1982).

[22] C. M. Bender, K. A. Milton, and D. H. Sharp, Phys. Rev. Lett. **51**, 1815 (1983).

[23] B. A. Bernevig, T. L. Hughes, and S.-C. Zhang, Science **314**, 1757 (2006).

[24] Ya. M. Blanter and M. Büttiker, Phys. Rep. **336**, 1 (2000).

[25] D. Boosé and J. M. Luck, J. Phys. A **40**, 14045 (2007).

[26] D. Brockmann, L. Hufnagel, and T. Geisel, Nature **439**, 462 (2006).

[27] R. Brown, London and Edinburgh philosophical magazine and journal of science **4**, 161 (1828).

[28] S. V. Buldyrev, S. Havlin, A. Ya. Kazakov, M. G. E. da Luz, E. P. Raposo, H. E. Stanley, and G. M. Viswanathan, Phys. Rev. E **64**, 041108 (2001); S. V. Buldyrev et al., Physica A **302**, 148 (2001).

[29] A. Bunde and S. Havlin, editors, *Fractals and Disordered Systems* (Springer, 1996).

[30] M. Büttiker, Science **325**, 278 (2009).

[31] F. E. Camino, V. V. Kuznetsov, E. E. Mendez, M. E. Gershenson, D. Reuter, P. Schafmeister, and A. D. Wieck, Phys. Rev. B **68**, 073313 (2003).

[32] J. T. Chalker and P. D. Coddingon, J. Phys. C **21**, 2665 (1988).

[33] J. M. Chambers, C. L. Mallows, and B. W. Stuck, J. Am. Stat. Ass. **71**, 340 (1976).

[34] V. V. Cheianov and V. I. Fal'ko, Phys. Rev. B **74**, 041403(R) (2006).

[35] V. V. Cheianov, V. I. Fal'ko, B. L. Altshuler, and I. L. Aleiner, Phys. Rev. Lett. **99**, 176801 (2007).

[36] K. W. Cheung, K. W. Yu, and P. M. Hui, Phys. Rev. B **45**, 456 (1992).

[37] R. Danneau, F. Wu, M. F. Craciun, S. Russo, M. Y. Tomi, J. Salmilehto, A. F. Morpurgo, and P. J. Hakonen, Phys. Rev. Lett. **100**, 196802 (2008).

[38] S. Datta and B. Das, Appl. Phys. Lett. **56**, 665 (1990).

[39] S. Datta, *Electronic transport in mesoscopic systems* (Cambridge University Press, 1995).

[40] A. Davis and A. Marshak, in *Fractal Frontiers*, edited by M. M. Novak and T. G. Dewey (World Scientific, 1997).

[41] L. DiCarlo, J. R. Williams, Y. Zhang, D. T. McClure, and C. M. Marcus, Phys. Rev. Lett. **100**, 156801 (2008).

[42] F. Evers and A. D. Mirlin, Rev. Mod. Phys. **80**, 1355 (2008).

[43] B. Fourcade and A.-M. S. Tremblay, Phys. Rev. B **34**, 7802 (1986).

[44] L. Fu and C. L. Kane, Phys. Rev. B **76**, 045302 (2007).

[45] L. Fu, C. L. Kane, and E. J. Mele, Phys. Rev. Lett. **98**, 106803 (2007).

[46] Y. Gefen, A. Aharony, and S. Alexander, Phys. Rev. Lett. **50**, 77 (1983).

[47] A. K. Geim and K. S. Novoselov, Nature Mat. **6**, 183 (2007).

[48] C. W. Groth, J. Tworzydło, and C. W. J. Beenakker, Phys. Rev. Lett. **100**, 176804 (2008).

[49] H.-M. Guo, G. Rosenberg, G. Refael, M. Franz, arXiv:1006.2777.

[50] M. Z. Hasan and C. L. Kane, arXiv:1002.3895.

[51] A. Hansen and M. Nelkin, Phys. Rev. B **33**, 649 (1986).

[52] S. Havlin, A. Bunde, and H. E. Stanley, Phys. Rev. B **34**, 445 (1986).

[53] S. Havlin and D. Ben-Avraham, Adv. Phys. **36**, 695 (1987).

[54] C.-M. Ho and J. T. Chalker, Phys. Rev. B **54**, 8708 (1996).

[55] D. Hsieh, D. Qian, L. Wray, Y. Xia, Y. S. Hor, R. J. Cava, and M. Z. Hasan, Nature **452**, 970 (2008).

[56] E. H. Hwang, S. Adam, and S. DasSarma, Phys. Rev. Lett. **98**, 186806 (2007).

[57] M. B. Isichenko, Rev. Mod. Phys. **64**, 961 (1992).

[58] F. J. Jedema, H. B. Heersche, A. T. Filip, J. J. A. Baselmans, and B. J. van Wees, Nature **416**, 713 (2001).

[59] H. Jiang, L. Wang, Q.-F. Sun, and X. C Xie, Phys. Rev. B **80**, 165316 (2009).

[60] M. Johnson and R. H. Silsbee, Phys. Rev. Lett. **55**, 1790 (1985).

[61] M. J. M. de Jong and C. W. J. Beenakker, Phys. Rev. B **51**, 16867 (1995).

[62] C. L. Kane and E. J. Mele, Phys. Rev. Lett. **95**, 226801 (2005).

[63] M. I. Katsnelson, Eur. Phys. J. B **51**, 157 (2006).

[64] M. I. Katsnelson, K. S. Novoselov and A. K. Geim, Nature Phys. **2**, 620 (2006).

[65] K. Kazymyrenko and X. Waintal, Phys. Rev. B **77**, 115119 (2008).

[66] K. Kechedzhi, O. Kashuba, and V. I. Fal'ko, Phys. Rev. B **77**, 193403 (2008).

[67] M. Yu. Kharitonov and K. B. Efetov, Phys. Rev. B **78**, 033404 (2008).

[68] Y. A. Kinkhabwala, V. A. Sverdlov, A. N. Korotkov, and K. K. Likharev, J. Phys. Condens. Matter **18**, 1999 (2006).

[69] K. v. Klitzing, G. Dorda, M. Pepper, Phys. Rev. Lett. **45**, 494 (1980).

[70] M. König, S. Wiedmann, C. Brüne, A. Roth, H. Buhmann, L. W. Molenkamp, X.-L. Qi, and S.-C. Zhang, Science **318**, 766 (2007).

[71] J. Kogut and L. Susskind, Phys. Rev. B **11**, 395 (1975).

[72] H. Kohno and H. Yoshida, Solid State Comm. **132**, 59 (2004).

[73] M. König, S. Wiedmann, C. Brüne, A. Roth, H. Buhmann, L. Molenkamp, X.-L. Qi, and S.-C. Zhang, Science **318**, 766 (2007).

[74] M. König, H. Buhmann, L. Molenkamp, T. Hughes, C.-X. Liu, X.-L. Qi, and S.-C. Zhang, J. Phys. Soc. Japan **77**, 031007 (2008).

[75] B. Kramer, T. Ohtsuki, and S. Kettemann, Phys. Rep. **417**, 211 (2005).

[76] R. Kutner and Ph. Maass, J. Phys. A **31**, 2603 (1998).

[77] V. V. Kuznetsov, E. E. Mendez, X. Zuo, G. L. Snider, and E. T. Croke, Phys. Rev. Lett. **85**, 397 (2000).

[78] H. Larralde, F. Leyvraz, G. Martinez-Mekler, R. Rechtman, and S. Ruffo, Phys. Rev. E **58**, 4254 (1998).

[79] P. Levitz, Europhys. Lett. **39**, 6593 (1997).

[80] C. H. Lewenkopf, E. R. Mucciolo, and A. H. Castro Neto, Phys. Rev. B **77**, 081410(R) (2008).

[81] J. Li, R.-L. Chu, J. K. Jain, and S.-Q. Shen, Phys. Rev. Lett. **102**, 136806 (2009); commentary by S. Mitra in Physics, April 6, 2009.

[82] C.-X. Liu, T. Hughes, X.-L. Qi, K. Wang, and S.-C. Zhang, Phys. Rev. Lett. **100**, 236601 (2008).

[83] C.-X. Liu, X.-L. Qi, X. Dai, Z. Fang, and S.-C. Zhang, Phys. Rev. Lett. **101**, 146802 (2008).

[84] R. C. Liu, P. Eastman, and Y. Yamamoto, Solid State Comm. **102**, 785 (1997).

[85] X. Lou, C. Adelmann, S. A. Crooker, E. S. Garlid, J. Zhang, K. S. Madhukar Reddy, S. D. Flexner, C. J. Palmstrom, and P. A. Crowell, Nature Phys. **3**, 197 (2007).

[86] A. W. W. Ludwig, M. P. A. Fisher, R. Shankar, and G. Grinstein, Phys. Rev. B **50**, 7526 (1994).

[87] B. B. Mandelbrot, *The Fractal Geometry of Nature* (Freeman, New York, 1983).

[88] R. N. Mantegna, Phys. Rev. E **49**, 4677 (1994).

[89] J. Martin, N. Akerman, G. Ulbricht, T. Lohmann, J. H. Smet, K. von Klitzing, and A. Yacoby, Nature Phys. **4**, 144 (2008).

[90] E. McCann, K. Kechedzhi, V. I. Fal'ko, H. Suzuura, T. Ando, and B. L. Altshuler, Phys. Rev. Lett. **97**, 146805 (2006).

[91] J. W. McClure, Phys. Rev. **104**, 666 (1956).

[92] R. Metzler and J. Klafter, Phys. Rep. **339**, 1 (2000).

[93] J. C. Meyer, A. K. Geim, M. I. Katsnelson, K. S. Novoselov, T. J. Booth, and S. Roth, Nature **446**, 60 (2007).

[94] J. E. Moore and L. Balents, Phys. Rev. B **75**, 121306(R) (2007).

[95] J. Moore, Nature Phys. **5**, 378 (2009).

[96] K. E. Nagaev, Phys. Lett. A **169**, 103 (1992).

[97] Yu. V. Nazarov, Phys. Rev. Lett. **73**, 134 (1994).

[98] H. B. Nielsen and M. Ninomiya, Nucl. Phys. B **185**, 20 (1981).

[99] K. Nomura, M. Koshino, and S. Ryu, Phys. Rev. Lett. **99**, 146806 (2007).

[100] K. Nomura, S. Ryu, M. Koshino, C. Mudry, and A. Furusaki, Phys. Rev. Lett. **100**, 246806 (2008).

[101] H. Obuse, A. Furusaki, S. Ryu, and C. Mudry, Phys. Rev. B **76**, 075301 (2007).

[102] M. Onoda and N. Nagaosa, Phys. Rev. Lett. **90**, 206601 (2003).

[103] M. Onoda, Y. Avishai, and N. Nagaosa, Phys. Rev. Lett. **98**, 076802 (2007).

[104] P. M. Ostrovsky, I.V. Gornyi, and A. D. Mirlin, Phys. Rev. Lett. **98**, 256801 (2007).

[105] B. Özyilmaz, P. Jarillo-Herrero, D. Efetov, D. A. Abanin, L. S. Levitov, and P. Kim, Phys. Rev. Lett. **99**, 166804 (2007).

[106] J. C. J. Paasschens, M. J. M. de Jong, and C. W. J. Beenakker, arXiv:0807.1623.

[107] K. Pearson, *A mathematical theory of random migration* (Dulau and co., London, 1906).

[108] X.-L. Qi, S.-C. Zhang, arXiv:1008.2026.

[109] R. Rammal and G. Toulouse, J. Phys. Lett. (Paris) **44**, L13 (1983).

[110] R. Rammal, J. Phys. Lett. (Paris) **45**, L1007 (1984).

[111] S. Redner, arXiv:0710.1105.

[112] P.-E. Roche, B. Derrida, and B. Douçot, Eur. Phys. J. B **43**, 1434 (2005).

[113] A. Roth, C. Bruene, H. Buhmann, L. W. Molenkamp, J. Maciejko, X.-L. Qi, and S.-C. Zhang, Science **325**, 294 (2009).

[114] R. Roy, Phys. Rev. B **79**, 195321 (2009).

[115] S. Russ, J. W. Kantelhardt, A. Bunde, and S. Havlin, Phys. Rev. B **64**, 134209 (2001).

[116] A. Rycerz, J. Tworzydło, and C. W. J. Beenakker, Europhys. Lett. **79**, 57003 (2007).

[117] S. Ryu, C. Mudry, H. Obuse, and A. Furusaki, Phys. Rev. Lett. **99**, 116601 (2007).

[118] P. San-Jose, E. Prada, and D. S. Golubev, Phys. Rev. B **76**, 195445 (2007).

[119] G. M. Schütz, in *Phase Transitions and Critical Phenomena*, edited by C. Domb and J. L. Lebowitz (Academic, 2001).

[120] M. Schulz, Phys. Lett. A **298**, 105 (2002); M. Schulz and P. Reineker, Chem. Phys. **284**, 331 (2002).

[121] A. Schuessler, P. M. Ostrovsky, I. V. Gornyi, and A. D. Mirlin, Phys. Rev. B **79**, 075405 (2009).

[122] A. Schuessler, P. M. Ostrovsky, I. V. Gornyi, and A. D. Mirlin, Phys. Rev. B **82**, 085419 (2010)

[123] M. J. Schmidt, E. G. Novik, M. Kindermann, and B. Trauzettel, Phys. Rev. B **79**, 241306(R) (2009).

[124] R. A. Sepkhanov, A. Ossipov, and C. W. J. Beenakker, Europhys. Lett. **85**, 14005 (2009).

[125] H. Scher and E. Montroll, Phys. Rev. B **12**, 2455, (1975).

[126] P. Sheng, *Introduction to Wave Scattering, Localization, and Mesoscopic Phenomena* (Springer, Berlin, 2006).

[127] R. Shindou and S. Murakami, Phys. Rev. B, **79**, 045321 (2009).

[128] B. I. Shklovskii and A. L. Efros, *Electronic Properties of Doped Semiconductors* (Springer, 1984).

[129] M. Shlesinger, G. Zaslavsky, and U. Frisch, editors, *Lévy Flights and Related Topics in Physics* (Springer, Berlin, 1995).

[130] W. Sierpiński, C. R. Acad. Sci. Paris **160**, 302 (1915).

[131] Y. Asada, K. Slevin, and T. Ohtsuki, Phys. Rev. B **70**, 035115 (2004).

[132] K. Slevin and T. Ohtsuki, Phys. Rev. B **80**, 041304(R) (2009).

[133] I. Snyman, J. Tworzydło, and C. W. J. Beenakker, Phys. Rev. B **78**, 045118 (2008).

[134] R. Stacey, Phys. Rev. D **26**, 468 (1982).

[135] D. Stauffer and A. Aharony, *Introduction to Percolation Theory* (Taylor and Francis, 1994).

[136] E. V. Sukhorukov and D. Loss, Phys. Rev. Lett. **80**, 4959 (1998).

[137] H. Suzuura and T. Ando, Phys. Rev. Lett. **89**, 266603 (2002).

[138] H. Tamura and T. Ando, Phys. Rev. B **44**, 1792 (1991).

[139] N. Tombros, C. Jozsa, M. Popinciuc, H. T. Jonkman, and B. J. Van Wees, Nature **448**, 571 (2007).

[140] S. A. Trugman, Phys. Rev. B **27**, 7539 (1983).

[141] J. Tworzydło, B. Trauzettel, M. Titov, A. Rycerz, and C. W. J. Beenakker, Phys. Rev. Lett. **96**, 246802 (2006).

[142] J. Tworzydło, I. Snyman, A. R. Akhmerov, and C. W. J. Beenakker, Phys. Rev. B **76**, 035411 (2007).

[143] P. R. Wallace, Phys. Rev. **71**, 622 (1947).

[144] I. Webman, Phys. Rev. Lett. **47**, 1496 (1981).

[145] E. R. Weeks, J. S. Urbach, and H. L. Swinney, Physica D **97**, 291 (1996).

[146] J. R. Williams, L. DiCarlo, and C. M. Marcus, Science **317**, 638 (2007).

[147] K. Wilson, in *New Phenomena in Subnuclear Physics*, edited by A. Zichichi (Plenum, New York, 1977).

[148] Y.-Y. Zhang, J. Hu, B. A. Bernevig, X. R. Wang, X. C Xie, and W. M Liu, Phys. Rev. Lett **102**, 106401 (2009).

[149] S.-C. Zhang, Physics **1**, 6 (2008).

[150] H. Zhang, C.-X. Liu, X.-L. Qi, X. Dai, Z. Fang, and S.-C. Zhang, Nature Phys. **5**, 438 (2009).

[151] I. Žutić, J. Fabian, and S. Das Sarma, Rev. Mod. Phys. **76**, 323 (2004).

Summary

Imagine an indecisive hiker standing somewhere along a path, constantly tossing a coin. Whenever the result is "heads", he walks one step further. Whenever the result is "tails", he takes a step back. How does this situation relate to someone heating (for a short while) a metal bar with a lighter? Both the "density of the hiker" (i.e. the probability to find him per piece of path), and the density of heat in the rod (determined by the temperature) spread with time according to the diffusion equation. This equation essentially states that the extent of the density profile grows as the square root of time. In the case of the hiker this means that if he has (averaged over many repetitions of this tiresome procedure) moved from his starting point by 20 meters after 15 minutes, we can expect him to have moved by 40 meters on average after one hour. Similar processes are abundant in nature and include the spreading of impurities in crystals as well as the sprawling of infected mosquitos.

The square-root-law of diffusion is remarkably universal, yet there exist cases in nature where the random spreading does not follow this law. Such diffusion is called *anomalous* – the width of the density profile spreads as a power of time which lies somewhere between 0 and 1, different from the power 1/2 of normal diffusion. For example, it has been found that contaminations in ground water spread slower than if they would be governed by normal diffusion. This is due to the pollutants getting trapped underground for long times too often to sustain normal diffusion. Slower-than-normal diffusion is called subdiffusion. Superdiffusion, faster than normal, is also possible, and has been observed for example in the transmission of skylight through cloudy atmospheres.

Anomalous diffusion can also occur in electrical conduction through disordered metals and semiconductors. At low temperatures quantum mechanics enters as another mechanism by which the diffusion of electrons can become anomalous. It may slow down to a complete halt due to destructive interference, while if the interference is constructive, the opposite effect can happen.

This thesis addresses a variety of systems in which the diffusion is anomalous, mainly motivated by recent experimental developments.

In Chapter 2 we look at the consequences that slower-than-normal diffusion on fractals has for shot noise, the time-dependent fluctuations of the electric current. Fractals are self-similar geometric objects characterized by a non-integer dimension. (Cloud patterns are a familiar example of fractals.) Our study is motivated by the fractals which form from "puddles" of electrons and holes in graphene, a one-atom thick sheet of carbon.

Faster-than-normal diffusion requires long steps to happen sufficiently more often than in the case of normal diffusion. Recently, superdiffusion of photons was reported in a medium consisting of glass spheres with a large range of diameters. Because the arrangement of the spheres is fixed in time, the steps which the photon makes in the medium are correlated: a long step in one direction is likely to be followed by another long step in the opposite direction. To assess the importance of the correlations we examine in Chapter 3 the effects correlations have on superdiffusion in one dimension. Working in one dimension enhances the correlations (thus providing a worst-case estimate) and allows an exact solution in closed form.

Electrons in graphene have the unusual property that they are massless, and their wave equation is the relativistic Dirac equation, rather than the nonrelativistic Schrödinger equation. (These massless electrons are the Dirac fermions from the title.) Quantum interference in graphene is constructive rather than destructive on average. As a consequence, while increasing the disorder strength in normal materials makes it more difficult for electrons to travel, in

the case of graphene the opposite effect can occur. In Chapter 4 we develop and demonstrate the usefulness of a method to simulate the anomalous diffusion of Dirac fermions in a computer.

The last two chapters of this thesis address other properties of Dirac fermions, not directly related to anomalous diffusion. These appear in socalled topological insulators, a novel class of materials which are insulating in the bulk but can conduct via metallic edge states. These edge states are unique because spin-up and spin-down electrons move in opposite directions, regardless of any obstacles they might find along their way. Chapter 5 proposes and analyzes a spin precession experiment in topological insulators. In Chapter 6 we present the mechanism for the conversion of an ordinary insulator into a topological insulator by disorder. This conversion was reported in the literature, on the basis of computer simulations, but had remained unexplained.

Samenvatting

Stel je voor, een twijfelende wandelaar ergens op een pad, die steeds maar weer een munt opgooit. Als het resultaat "kruis" is, doet hij een stap naar voren. Als het resultaat "munt" is, doet hij een stap naar achteren. Wat is het verband met het (gedurende korte tijd) opwarmen van een metalen staaf met een aansteker? Zowel de "dichtheid van de wandelaar" (namelijk, de kans om hem in een bepaald stuk van het pad aan te treffen), alsook de dichtheid van warmte in de staaf (bepaald door de temperatuur) breiden zich met de tijd uit volgens een diffusievergelijking. Deze vergelijking zegt in essentie dat de uitgebreidheid van het dichtheidsprofiel groeit met de wortel uit de tijd. In het geval van de wandelaar betekent dit dat, als hij zich (gemiddeld over vele herhalingen van deze vermoeiende operatie) 20 meter van zijn startpositie heeft verplaatst na 15 minuten, we kunnen verwachten dat hij zich gemiddeld 40 meter heeft verplaatst na een uur. Soortgelijke processen komen veel voor in de natuur, van de verspreiding van verontreinigingen in een kristal tot de verspreiding van geïnfecteerde muskieten.

De wortel-uit-de-tijd wet van diffusie is opvallend universeel, en toch zijn er gevallen in de natuur waar het toevallig verspreiden van deze wetmatigheid afwijkt. Zulke diffusie heet *anomaal* – de breedte van het dichtheidsprofiel breidt zich in de tijd uit met een macht die ergens tussen 0 en 1 ligt, verschillend van de macht 1/2 van normale diffusie. Bijvoorbeeld, het is bekend dat verontreinigingen in water zich langzamer verspreiden dan het gevolg zou zijn van normale diffusie. De reden is dat verontreinigingen lange tijd onder de grond vast kunnen komen te zitten. Diffusie die langzamer is dan normaal heet subdiffusie. Superdiffusie, sneller dan normaal, is ook mogelijk, en is bijvoorbeeld waargenomen in

de voortplanting van hemellicht door een bewolkte atmosfeer.

Anomale diffusie kan ook voorkomen in elektrische geleiding door wanordelijke metalen en halfgeleiders. Bij lage temperaturen doet de kwantummechanica haar intrede als een ander mechanisme waardoor diffusie van elektronen anomaal kan worden. Het kan vertragen tot een komplete stop ten gevolge van destructieve interferentie, terwijl constructieve interferentie het tegenovergestelde kan bewerkstelligen.

Dit proefschrift behandelt een verscheidenheid van systemen waarin de diffusie anomaal is, vooral gemotiveerd door recente experimentele ontwikkelingen.

In hoofdstuk 2 onderzoeken we de gevolgen die langzamer-dan-normale diffusie op fraktalen heeft voor hagelruis, de tijds-afhankelijke fluctuaties van de elektrische stroom. Fraktalen zijn geometrische objecten die gekarakteriseerd worden door een niet-heeltallige dimensie. (Wolkpatronen zijn een vertrouwd voorbeeld van fraktalen.) Onze studie is gemotiveerd door de fraktalen die gevormd worden door de gebiedjes van elektronen en gaten in grafeen, een enkele laag koolstofatomen.

Sneller-dan-normale diffusie vereist lange stappen, met een hogere frequentie dan bij normale diffusie. Recent is superdiffusie van fotonen gerapporteerd in een medium bestaande uit glazen bollen met een grote verscheidenheid aan diameters. Omdat de ordening van de bollen vast ligt in de tijd, zijn de stappen die een foton maakt door het medium gecorreleerd: een lange stap in de ene richting wordt waarschijnlijk gevolgd door een lange stap in de omgekeerde richting. Om het belang van de correlaties te onderzoeken bestuderen we in hoofdstuk 3 het effect van correlaties op superdiffusie in één dimensie. In één dimensie is het effect van correlaties het sterkst (het is dus een "worst-case" geval), en deze dimensie heeft het voordeel dat een exacte oplossing kan worden opgeschreven.

Elektronen in grafeen hebben de ongebruikelijke eigenschap dat ze massaloos zijn. Hun golfvergelijking is de relativistische Dirac-vergelijking, in plaats van de niet-relativistische Schrödinger-

vergelijking. (Deze masssaloze elektronen zijn de Dirac-fermionen uit de titel.) Kwantum-interferentie in grafeen is constructief in plaats van destructief, gemiddeld gesproken. Terwijl toename van de wanorde in gewone materialen het moeilijker maakt voor elektronen om zich voort te bewegen, gebeurt in grafeen het tegenovergestelde. In hoofdstuk 4 ontwikkelen en demonstreren we een methode om de anomale diffusie van Dirac-fermionen op een computer te simuleren.

De laatste twee hoofdstukken van dit proefschrift behandelen andere eigenschappen van Dirac-fermionen, niet direct gerelateerd aan anomale diffusie. Deze treden op in zogenaamde topologische isolatoren, een nieuwe klasse van materialen die isoleren in het binnenste maar geleiden via metallische randtoestanden. Deze randtoestanden zijn uniek omdat spin-op en spin-neer elektronen in tegenovergestelde richtingen bewegen, ongeacht een obstakel dat ze op hun weg zouden kunnen vinden. Hoofdstuk 5 stelt een spin-precessie experiment voor in topologische isolatoren, en analyseert het. In hoofdstuk 6 presenteren we een mechanisme om een gewone isolator te converteren in een topologische isolator door middel van wanorde. Deze conversie was gerapporteerd in de literatuur, op basis van computersimulaties, maar zonder verklaring.

List of Publications

- *Counting statistics of coherent population trapping in quantum dots*, C. W. Groth, B. Michaelis, C. W. J. Beenakker, Phys. Rev. B **74**, 125315 (2006).

- *Electronic shot noise in fractal conductors*, C. W. Groth, J. Tworzydło, C. W. J. Beenakker, Phys. Rev. Lett. **100**, 176804 (2008) [Chapter 2].

- *Finite difference method for transport properties of massless Dirac fermions*, J. Tworzydło, C. W. Groth, C. W. J. Beenakker, Phys. Rev. B **78**, 235438 (2008) [Chapter 4].

- *Nonalgebraic length dependence of transmission through a chain of barriers with a Lévy spacing distribution*, C. W. J. Beenakker, C. W. Groth, A. R. Akhmerov, Phys. Rev. B **79**, 024204 (2009) [Chapter 3].

- *Switching of electrical current by spin precession in the first Landau level of an inverted-gap semiconductor*, A. R. Akhmerov, C. W. Groth, J. Tworzydło, C. W. J. Beenakker, Phys. Rev. B **80**, 195320 (2009) [Chapter 5].

- *Theory of the topological Anderson insulator*, C. W. Groth, M. Wimmer, A. R. Akhmerov, J. Tworzydło, C. W. J. Beenakker, Phys. Rev. Lett. **103**, 196805 (2009) [Chapter 6].

Curriculum Vitæ

I was born in Gdynia on the Polish Baltic coast on the 15th of December 1980. In 1990 my family moved to Kulmbach in Germany, where I received the remaining primary and secondary education. During school years I attended the science competition *Jugend forscht* six times, winning five times on regional level. In 2001 my project *Fluid simulation for computer graphics* won the second prize on national level. After finishing school in the same year, I worked for ten months in a boarding school for mentally disabled children as my compulsory community service.

In 2002 I enrolled at the University of Bayreuth for a German *Diplom* degree in physics. Having passed the intermediate exams after four semesters, I was granted a scholarship of *Cusanuswerk*. In 2005 I moved to the Netherlands to continue my studies at Leiden University, and obtained there in 2007 a master's degree in theoretical physics with a thesis entitled *Counting statistics of coherent population trapping in quantum dots* supervised by prof. C. W. J. Beenakker. After graduation I stayed in the group of prof. Beenakker employed by *Stichting FOM* to pursue the research which is documented in this thesis.

During my studies in Germany I taught exercise classes in Quantum Mechanics I. In Leiden I taught the exercise classes in Computational Physics and Electromagnetism II. I have attended two summer schools and represented my work at a number of conferences.

Stellingen

behorende bij het proefschrift

Anomalous diffusion of Dirac fermions

1. Our finding that diffusion and subdiffusion have the same Fano factor can explain the carrier-density independent measurements of DiCarlo et al.

   L. DiCarlo, J. R. Williams, Y. Zhang,
   D. T. McClure, and C. M. Marcus,
   Phys. Rev. Lett. **100**, 156801 (2008);
   This thesis, Chapter 2.

2. The strong effects of correlations found in a one-dimensional Lévy glass persist in higher dimensions.

   This thesis, Chapter 3.

3. A Lévy walk with characteristic exponent α has a transmission probability over a length L which decays as $L^{1-\alpha}$ for $1 < \alpha < 2$ and is length-independent for $0 < \alpha < 1$.

4. Inverted-gap semiconductors are ideally suited to realize the Datta-Das transistor.

   This thesis, Chapter 5.

5. The name "topological Anderson insulator" is a misnomer.

   This thesis, Chapter 6.

6. In chiral p-wave superconductors, the tricritical point at the intersection of the metal-insulator and insulator-insulator phase boundaries is repulsive.

   M. V. Medvedyeva, J. Tworzydło, and C. W. J. Beenakker,
   Phys. Rev. B **81**, 214203 (2010).

7. Inclusion of a vector potential in the discretized single-valley Dirac equation breaks gauge invariance.

8. The fact that modern travel is superdiffusive hinders the confinement of epidemics.

D. Brockmann, L. Hufnagel, and T. Geisel,
Nature **439**, 462 (2006).

9. The freedom to modify (and therefore to study, fix, and improve) the things one owns is increasingly endangered.

Christoph Groth,
November 2010